BUOYANCY-DRIVEN PARTICLE-LADEN EXCHANGE FLOWS IN INCLINED CONDUITS

A Thesis

Presented to

the Faculty of the Department of Engineering Technology

University of Houston

In Partial Fulfillment

of the Requirements for the Degree

Master of Science

in Engineering Technology

by

Nima Mirzaeian

May 2018

BUOYANCY-DRIVEN PARTICLE-LADEN EXCHANGE FLOWS IN INCLINED CONDUITS

Nima Mirzaeian

Approved:

Chair of the Committee
Kamran Alba, Assistant Professor,
Engineering Technology

Committee Members:

Medhat El Nahas, Assistant Professor,
Engineering Technology

Navdeep Singh, Assistant Professor,
Engineering Technology

Jacinta C. Conrad, Associate Professor,
Chemical and Biomolecular Engineering

George Zouridakis, Associate Dean of Research,
College of Technology

Wajiha Shireen, Chair,
Engineering Technology

Acknowledgements

Firstly, I would like to offer my deep appreciation to my supervisor, Professor Kamran Alba, for giving me an exceptional opportunity of participating in his research projects during my Master's program. It was a profound professional experience and an enjoyable journey in my life. Not alone I could learn the high quality research from Kamran, but also he influenced me in a very personal level. He taught me that through perseverance, concentration, and hard work, impossible can become possible. He showed me an exalted path to pursue and higher ambitions to aim for. His discipline and support helped me to grow beyond my expectations within the short term of our collaboration. Thank you for being a humble mentor and a caring friend.

I also want to thank my dear colleagues, Aqib Hasnain, Gaarthick Ravichandran, Bahareh Eslami, Shadi Shariatnia, Olamide Oladosu, Pouya Jalalmanesh and many others for sharing their helpful experiences and inputs. We all could build a common identity behind the name of the Complex Fluid Group and celebrated our joyful moments of success together. They always gave me positive energy and motivation by their determination, discipline, and useful conversations.

During realizing the experimental apparatus, I had the honor of working with a skillful co-op, Hector Garza, without his contribution, I could not accomplish the research objectives. I would like to thank him for his valuable assistance and I wish him the best in his professional endeavor.

This projects could not be completed without the help of many technical and administrative staff in the University of Houston. I would like to thank Mike Mahanay, mechanical technician of the SR1 building, for his crucial technical supports, Gordon Taylor and Caesar Nunez, laboratory and machine shop managers in the College of

Technology for their tremendous help during building the set-up. Also, I would like to extend my appreciation to Nam Nguyen and Eduardo Cortes for their administrative supports.

In the end, I would like to thank the members of my thesis committee, Dr. Medhat El Nahas, Dr. Navdeep Singh, Dr. Jacinta C. Conrad, and Dr. Kamran Alba for participating in the defense meeting and providing insightful comments. This thesis is dedicated to my mother, Nezhat, and my father, Ghodratollah, for their endless kindness and continual trust. They are the main motive, and the true foundation behind this work.

BUOYANCY-DRIVEN PARTICLE-LADEN EXCHANGE FLOWS IN INCLINED CONDUITS

An Abstract

of a

Thesis

Presented to

the Faculty of the Department of Engineering Technology

University of Houston

In Partial Fulfillment

of the Requirements for the Degree

Master of Science

in Engineering Technology

by

Nima Mirzaeian

May 2018

Abstract

As an extension to the previously investigated buoyancy-driven exchange flow of pure fluids in inclined ducts, we propose an experimental and theoretical approach to practically study the effect of solid particles within the flow. The flow problem starts in a density-unstable lock-exchange configuration with heavy suspension being on top of a light pure fluid in a long narrow pipe or channel. Suspension is a mixture of negatively-buoyant solid particles in a Newtonian pure fluid. The density difference between the heavy and light phases is small enough to neglect the inertia (Boussinesq approximation).

Flow is firstly studied through an experimental framework. Various sedimentary, transitionary, and mixing regimes are observed based on the pipe inclination angle, β, and initial volume fraction of particles, ϕ_0. The results are mapped on dimensionless diagrams suitable for industrial design and environmental planning. Effects of particle size and fluid's viscosity are further discussed. The sedimentary behavior is diminished by reducing particle size, whereas remains unchanged with fluid's viscosity. The advancement frontal speed of the heavy suspension layer into the light pure fluid, $\hat{V}_f$, is measured over full range of experiments. It is found that $\hat{V}_f$ becomes larger as the pipe is titled away from the horizontal direction. An intermediate range of particle volume fraction, ϕ_0, is interestingly discovered to lead to maximal $\hat{V}_f$. A non-dimensional scale for frontal velocity is successfully proposed constituting various flow and geometrical parameters.

For strictly vertical duct, a lubrication model is developed to theoretically investigate the flow in this simplified configuration. Novel particle-rich zones inside the suspension are further discovered in the vicinity of the advancing heavy and light fronts. It was further revealed that the geometry confinement plays a signif-

icant role in exchange flow dynamics through formation of interfacial patterns and particle-enrichment behavior. The fundamental findings of this thesis help understand the dynamics of important flows observed in nature within oceanographic and geophysical contexts as well as in industry through discharge, transport and dispersion of slurries, mine tailings, pastes, pharmaceuticals, paper pulp, drill cuttings, sludge, effluents and sewage, manufacture of cement clinker in inclined kilns, mineral processing in hydrocyclones, and inclined fluidized beds.

Table of Contents

Acknowledgements **v**

Abstract **viii**

Table of Contents **x**

List of Figures **xii**

List of Tables **xv**

Nomenclature **xvi**

1 Introduction **1**

1.1 Problem of study 1

1.2 Outline of the thesis 6

2 Experiments **7**

2.1 Experimental approach 7

2.1.1 Methodology 7

2.1.2 Range of parameters 9

2.2 Results 12

2.2.1 Buoyancy-driven exchange flow of pure fluids in inclined pipes . 12

2.2.2 Particle-laden exchange flows in near-horizontal angles: halt time and distance 14

2.2.3 Particle-laden exchange flows in inclined pipes 18

3 Modeling **32**

3.1 Dimensional and dimensionless governing parameters 34

3.2 Lubrication model derivation 36
3.3 Numerical scheme 42
3.3.1 Procedure 42
3.3.2 Benchmarking notes 44
3.4 Results 44
3.4.1 Pure fluids ($\phi_0 = 0$) 44
3.4.2 Particle-laden flows ($\phi_0 > 0$) 50
3.5 Comparison between theory and experiment 59

4 Conclusions **62**
4.1 Contributions 62
4.2 Future works 66

A Benchmarking against pure (particle-free) exchange flow study of Seon *et al.* (2005) [16] **79**

B Shear-induced migration effects **81**

C Axisymmetric flow in pipe **83**

D Coefficients in velocity expressions (3.15) and (3.16) for 2D channel case **87**

E Flux function, q, in (3.17) for 2D channel case **88**

F Derivation of lubrication model Eqs. (3.18) and (3.19) for 2D channel **89**

G Derivation of lubrication model for axisymmetric flow in pipe (Appendix C) **93**

List of Figures

1.1 Schematic of the problem. 2

1.2 Applications of the buoyant particle-laden exchange flows 3

2.1 Schematic of the experimental apparatus. 8

2.2 Sequence of experimental images for pure fluid and array of images over the full range of inclination angle, β. 13

2.3 Sequence of images at different times, spatio-temporal diagram, leading front's location $\hat{X}_f^2(\hat{t})$, and frontal velocity, $\hat{V}_f(\hat{t})$ for a near-horizontal experiment from set A. 15

2.4 Variation of the stoppage distance $\hat{X}_s$, and time $\hat{t}_s$, with initial volume fraction of particles, ϕ_0 at near-horizontal angle. 17

2.5 Experimental images and spatio-temporal diagrams for three flow regimes: sedimentary, transitionary, and mixing. 19

2.6 Suspension front position, $\hat{X}_f^2(\hat{t})$, over time, $\hat{t}$, for various angles of inclination and ϕ_0 corresponding to the experiments in set A. 20

2.7 Array of experimental images at various angles corresponding to the experiments of set A 22

2.8 Concentration profiles, $\bar{C}$, on the right-hand side of the pipe over time, $\hat{t}$, showing the formation of a ridge close to the front region. 24

2.9 Phase diagram and variation of the mean frontal velocity $\hat{V}_{f,av}$, versus angle of inclination β, for experiments in set A 25

2.10 Array of experimental images at various angles corresponding to the experiments of set B 27

2.11 Phase diagram and variation of the mean frontal velocity $\hat{V}_{f,av}$, versus angle of inclination β, for experiments in set B 27
2.12 Array of experimental images at various angles corresponding to the experiments of set C 30
2.13 Phase diagram and variation of the mean frontal velocity $\hat{V}_{f,av}$, versus angle of inclination β, for experiments in set C 30

3.1 Schematic of the symmetric particle-laden exchange flow in a vertical 2D duct used in the lubrication model analysis. 33
3.2 Variation of the flux function, q, in (3.17) with interface height, h, for pure fluids 40
3.3 Evolution of the interface height, h, with time, t, in exchange flow of two iso-viscous fluids 45
3.4 Comparison of the interface height, h, at different values of Re, and κ. 47
3.5 Variation of heavy front height, h_{Hf}, and light front height, h_{Lf} versus κ for all values of $Re > 0$. 49
3.6 Evolution of the interface height, h, and particle volume fraction, ϕ, profiles with time, t. 51
3.7 Change in interface height, h, and particle volume fraction, ϕ, with x at various values of the precursor film thickness, b. 52
3.8 Change in interface height, h, and particle volume fraction, ϕ, with x at various values of the Reynolds number, Re. 53
3.9 Change in interface height, h, and particle volume fraction, ϕ, with x at various values of the initial particle volume fraction, ϕ_0. 54
3.10 Change in interface height, h, and particle volume fraction, ϕ, with x at various values of the light-to-carrying-fluid viscosity ratio, κ. 55
3.11 Change in interface height, h, and particle volume fraction, ϕ, with x at various values of the particle-radius-to-half-the-duct-width ratio, r_p. 56

3.12 Change in interface height, h, and particle volume fraction, ϕ, with x at various values of the particle-to-carrying-fluid density ratio, ξ. 57
3.13 Change in interface height, h, and particle volume fraction, ϕ, with x at various values of the light-to-carrying-fluid density ratio, η. 58
3.14 Comparison between theoretical and experimental results of buoyant exchange flow of pure fluid. 60
3.15 Comparison between theoretical and experimental results of buoyant particle-laden exchange flow. 60

A.1 Benchmarking result of experiments for pure fluid 80

C.1 Schematic of axisymmetric particle-laden exchange flow in a vertical pipe. 84
C.2 Comparison of interface height profile, h, for pure fluid and particle-laden cases between pipe and 2D channel 85

List of Tables

2.1 List of *dimensional* independent parameters in the experiments. 10
2.2 List of *dimensionless* independent parameters in the experiments. . . . 11
2.3 List of experimental sets along with their corresponding parameter ranges. 12

3.1 List of *dimensional* independent input parameters of the lubrication model problem. 35
3.2 List of *dimensionless* independent input parameters of the lubrication model problem. 36

Nomenclature

Dimensional

$\hat{g}$	Gravitational acceleration
$\hat{D}$	Pipe diameter, Half of the duct width
$\hat{L}$	Pipe length, Duct length
$\hat{d}$	Particle diameter
$\hat{a}$	Particle radius
$\hat{\rho}_p$	Particle density
$\hat{\rho}_L$	Light fluid density
$\hat{\rho}_H$	Heavy fluid (suspension) viscosity
$\hat{\rho}_f,\ \hat{\rho}_{f,H}$	Carrying (pure) fluid density
$\hat{\mu}_L$	Light fluid viscosity
$\hat{\mu}_H$	Heavy fluid (suspension) viscosity
$\hat{\mu}_f,\ \hat{\mu}_{f,H}$	Carrying (pure) fluid viscosity
$\hat{V}_p$	Initial volume of particles
$\hat{V}_j$	Jamming volume of particles
$\hat{V}_H$	Volume of heavy fluid (suspension)
$\hat{\nu}_f$	Kinematic viscosity of carrying (pure) fluid
$\hat{\nu}_{av}$	Average kinematic viscosity of heavy and light fluids
$\hat{V}_t$	Characteristic velocity of inertial regime
$\hat{V}_v$	Characteristic velocity of viscous regime
$\hat{u}_0$	Stokes settling velocity of particles
$\hat{u}_s$	Hindered settling velocity of particles
$\hat{t}$	Time
$\hat{t}_s$	Halt time
$\hat{x}$	Length
$\hat{y}$	Width
$\hat{z}$	Depth
$\hat{X}_f$	Leading front's location
$\hat{X}_s$	Halt distance
$\hat{V}_f$	Leading front's velocity
$\hat{V}_{f,av}$	Leading front's average velocity
$\hat{U}_f$	Velocity scale of the leading front
$\hat{J}_{Migration}$	Shear-induced migration flux of particles
$\hat{J}_{Settling}$	Settling flux of particles

Dimensionless

δ	Aspect ratio
β	Pipe inclination angle
r_p	Particle-to-pipe-diameter ratio
ξ	Particle-to-fluid density ratio
η	Light-to-carrying-fluid density ratio
κ	Light-to-carrying-fluid viscosity ratio
ϕ_0	Initial volume fraction of particles
ϕ_j	Jamming volume fraction of particles
Re_t, Re	Reynolds number
ψ	Density ratio of light fluid to heavy fluid
m	Viscosity ratio of light fluid to heavy fluid
At	Atwood number
C	Concentration
$\bar{C}$	Average concentration
K_ν	Constant in shear-induced particle flux
Λ	Ratio of the sedimentation Grashof number to Reynolds number
C_F	Velocity scaling constant
ϕ	Volume fraction of particles
h	Height of the interface between heavy and light fluids
h_{Hf}	Height of the heavy fluid (suspension) front
h_{Lf}	Height of the light fluid front
V_{Hf}	Velocity of the heavy fluid (suspension) front
V_{Lf}	Velocity of the light fluid front
x	Length
y	Width
t	Time
u	Velocity
u_p	Relative velocity of particles to fluid
p	Pressure
τ	Shear stress
q	Flux function
ω	Wall function
λ	Similarity parameter in Lubrication model
b	Precursor film thickness

Chapter 1: Introduction

1.1 Problem of study

This thesis investigates buoyancy-driven interpenetration of a heavy particle-laden fluid into a light pure one in an inclined narrow conduit (pipe or duct). Flow starts by a gate release in the middle of a long lock-exchange geometry where heavy suspension occupies its upper half and a light pure fluid the lower one. Suspension in our study consists of negatively-buoyant solid particles. Both the carrying fluid and the light pure one are considered to follow Newtonian rheology. The suspension is collectively heavier than pure fluid due to the presence of heavy particles. Buoyancy is a significant driving force for the flow in this problem; however, pertaining to various configuration and fluid types, sedimentation may also be a crucial in the development of the flow. We study the effects of initial volume fraction of particles, ϕ_0, density ratio of light and heavy phases, ψ, inclination angle, β, size ratio of particle to pipe, r_p, density ratio of particle to the fluid, ξ, and density and viscosity ratios of light fluid to the carrying fluid, η, and κ, respectively. The diameter or width of the duct, denoted by $\hat{D}$, is comparably small with respect to its length, $\hat{L}$, suitable for capturing the behavior of fully developed flows. The inclination angle, β, changes from horizontal ($\beta = 90°$) to vertical directions ($\beta = 0°$), leading to different sedimentary or mixing mechanisms in the flow. Figure 1.1 shows a schematic of the problem. There are numerous buoyancy-driven flows in nature widely found in oceanography, meteorology, and geophysics [1–3]. There are also multiple applications of these flows in industry such as chemical, mining, and petroleum processes [4, 5]. Such flows, in practice, often carry solid particles along the way resulting in more complex behavior. Buoyant particle-laden flows have applications in discharge, transport and dis-

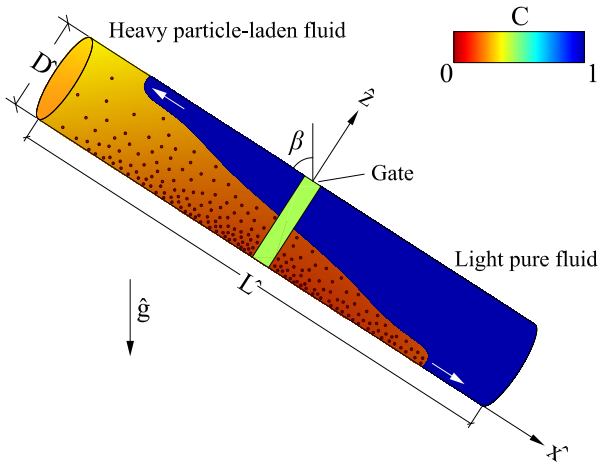

Figure 1.1: Schematic of the problem. Tilt angle β, measured from vertical. The interface shape and particle distribution are illustrative only.

persion of slurries, mine tailings, pastes, pharmaceuticals, paper pulp, drill cuttings, sludge, effluents and sewage [6–8], manufacture of cement clinker in inclined kilns [9], mineral processing in hydrocyclones [10], and inclined fluidized beds [11]. Our main motivation comes from complex buoyancy-driven flows that exist in the oil and gas industry vastly concerned with well construction e.g. drilling, well/plug cementing, and hydraulic fracturing; see figure 1.2a. The well cementing process requires a metal casing with circular cross section to be placed into the well. The remained drilling mud inside the pipe has to be removed by cement slurry being pumped or buoyantly released in the case of plug cementing. The mud then leaves the system from the very bottom of the pipe through the gap between the casing and the rocky wall. This problem has previously been investigated considering a pair of pure fluids [12–14]. In this study, we aim to understand the underlying mechanism of such buoyant flows in the presence of particles in order to design efficient industrial processes involving such flows. From a practical standpoint, the optimum condition of particle-laden exchange flow is to remove as much as drilling mud without considerable sedimentation along the channel (mixed suspension). Similar studies can also help preventing environmental hazards as seen for example, during the release of

particulate effluents into the fresh water canals (figure 1.2b). The buoyancy-driven suspension exchange flow perfectly imitates such scenario. Therefore, understanding the halting (mixing) behavior as well as interpenetration extent of flow can facilitate the design and planning of robust water way systems.

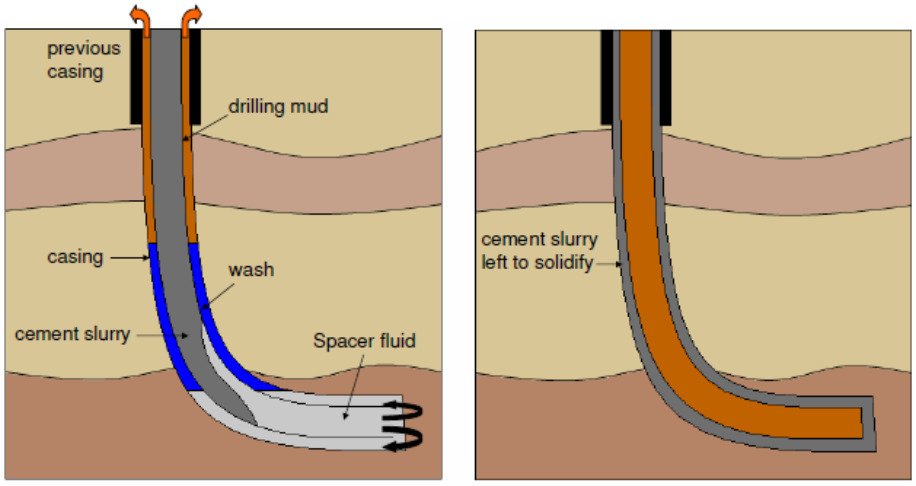

(a) © Kamran Alba

(b) © Greenpeace

Figure 1.2: Applications of the buoyant particle-laden exchange flows, (a) well cementing: cement (suspension) replaces the drilling mud (pure fluid) inside the well casing. (b) Release of effluents into the water canals.

Buoyancy-driven flows have been vastly studied experimentally [13, 15–17], analytically [18–21], and computationally [22–24] for pure fluids. Meanwhile, particulate flows have been studied in the literature primarily in the contexts of enhanced

sedimentation in inclined pipes (Boycott flow) [25–27], turbidity currents [28, 29], and particulate thin film flows over a substrate [30, 31]. The interpenetrating exchange flow of a suspension into a pure fluid within a practical duct geometry still remains to be meticulously studied. The complexity of such case arises from the effect that sedimentation imposes on the evolution of flow. Basically, settling tends to reduce the concentration of particles within the heavy mixture, and ultimately its buoyant advantage over the pure ambient. One of the very few studies available in literature on this topic is the recent work of Saha *et al.* (2013) [32], carried experimentally for horizontal configuration. They found that the particle-laden layer undergoes a sedimentary phase and finally halts at a finite distance. A comprehensive study of the particle-laden flows in pipes tilted at various angles still lacks severely in the literature. Current thesis studies this problem to address the following objectives:

- **Objective I: Identifying various sedimentary and/or mixed regimes**. Interpenetrating particle-laden flows may exhibit various *sedimentary* and/or *mixed* patterns as shown in the rather recent study of [30] for free-surface geometry. The mixed flows can be *uniform* or may contain *particle-rich* / *depleted* zones. Naturally, the question is what type of novel regimes are likely to emerge in the case of flow in duct? Understanding the sedimentation or mixing behavior of the particles is of great importance in many industries concerning slurry flows, for instance in characterizing the properties of gruels, sauces, salad dressings, chemicals, paints and cosmetics [33]. Through experimentation, we aim to fundamentally study the effect of various parameters of the problem such as duct inclination angle and particle/fluid properties on sedimentation and mixing.
- **Objective II: Characterizing the runout length and/or spreading speed**

of the interpenetrating layers. Sedimentation over time can lead to *halting* or *runout* [32]. On the other hand, if solid particles are remained mixed due to the dynamics of the flow they will continue spreading [30]. Two critical questions arise here: 1) What is the runout length and time in the case of sedimentary flows? 2) What is the spreading speed of interpenetrating layers in the case of mixed flows? There can be incredibly interesting counter-intuitive effects associated with the runout length and/or spreading speeds. For instance, in the case of sedimentary flows in horizontal configuration it has recently been observed that the maximum runout length/time is achieved within an *intermediate* range of particle volume fraction [32]. Moreover, in the case of continuous flows, the highest spreading rate of the interpenetrating and convective current is repeatedly reported to happen at an *intermediate* inclination angle. Through integrated experimental and mathematical methodologies, we aim to build a predictive framework responding to these unaddressed questions for the case of inclined channels.

- **Objective III: Classification of flow regimes in dimensionless maps**. Predictive flow regime maps concerning interpenetrating flows are of extreme importance in the process designs such as in mining [10] and energy industries [8]. Once flow regime maps in the *dimensionless* format are furnished, the engineers can conveniently locate pre-designed flows on these maps to ensure they meet the criteria. As third objective and after extensive analyses of the experimental and mathematical data obtained in the previous phases, we aim to provide the followings: 1) The underlying flow regimes related of interpenetrating particle-laden flows in ducts with respect to the dimensionless parameters of the problem. 2) Dimensionless formulas predicting the spreading speed of the layers in the applicable ranges to be achieved through curve-fitting of the experimental data.

The approaches taken to understand the suspension gravity current in this thesis are experimental and theoretical. The major part of the results are obtained by experiments explained in detail in chapter 2. The flow in the case of vertical channel is further described analytically through a system of conservative partial differential equations (PDEs), called as *lubrication model*; see chapter 3. The governing equations are then solved numerically to investigate the effects of wide range of parameters on the advancement and particle-enrichment in the flow. The final aim through these integrated studies is to fundamentally understand the underlying mechanisms of buoyant particle-laden exchange flows and to provide quantitative measures of flow parameters for optimized industrial design and environmental planning.

1.2 Outline of the thesis

The next chapter looks into the adopted experimental approach including methodology, the apparatus, and the range of parameters. We present the experimental results in this chapter for a range of ϕ_0 away from the packed limit, and over full range of tilt angles, β. The verification of the apparatus through benchmarking the experiments of [16] will be presented separately in appendix A. Chapter 3 lays out a mathematical analysis of the flow in vertical 2D channel. Complementary information will further be provided in the appendices. Appendix F will present the details of the lubrication model derivation. The discussion involving the shear-induced migration effects will be evaluated in appendix B. The adjusted model for the flow in axisymmetric pipe geometry will be given in appendix C. Additional coefficients and flux functions in the derived model are also available in appendices D and E. The thesis is closed in chapter 4 by highlighting the novel findings of the study, concluding remarks, industrial recommendations and future perspectives.

Chapter 2: Experiments

In this chapter we present the experimental results of particle-laden exchange flows over full range of tilt angles, β, and over a range of initial particle concentration, ϕ_0. The carrying fluid in the suspension is considered the same as light pure fluid, yet, the overall density of suspension is always maintained higher than the pure phase due to the presence of particles. Flows within our range of parameters adopt low Reynolds numbers (negligible inertia) and are in the limit of Boussinesq approximation, i.e., small density difference between heavy and light phases, thus, negligible inertia. Through measuring the extent of the interpenetration domain in the post-processed camera recordings of the pipe, various sedimentary and mixing regimes are identified, then, are plotted on the dimensionless maps of ϕ_0 and β. The same approach allows us to quantify the advancement rate of the flow in each of those experiments which are presented in the appropriate velocity figures.

2.1 Experimental approach

2.1.1 Methodology

We utilize an experimental apparatus consisting of an acrylic pipe with a pneumatic gate valve placed in the middle as shown in figure 2.1. The inner diameter and total length of the pipe are $\hat{D}$ = 9.53 mm and $\hat{L}$ = 2000 mm, respectively. These dimensions result in a small aspect ratio ($\delta = \hat{D}/\hat{L} \approx 0.0048$) suitable for capturing the long time and fully developed effects of the flow [32, 34, 35]. The entire pipe and valve structure is mounted on an aluminum frame which allows tilting of the pipe in clockwise way at an angle of inclination β, measured from the vertical direction. Heavy suspension occupies the left-hand side of the pipe and light pure fluid the right-hand side. The apparatus is equipped with solenoid valves and

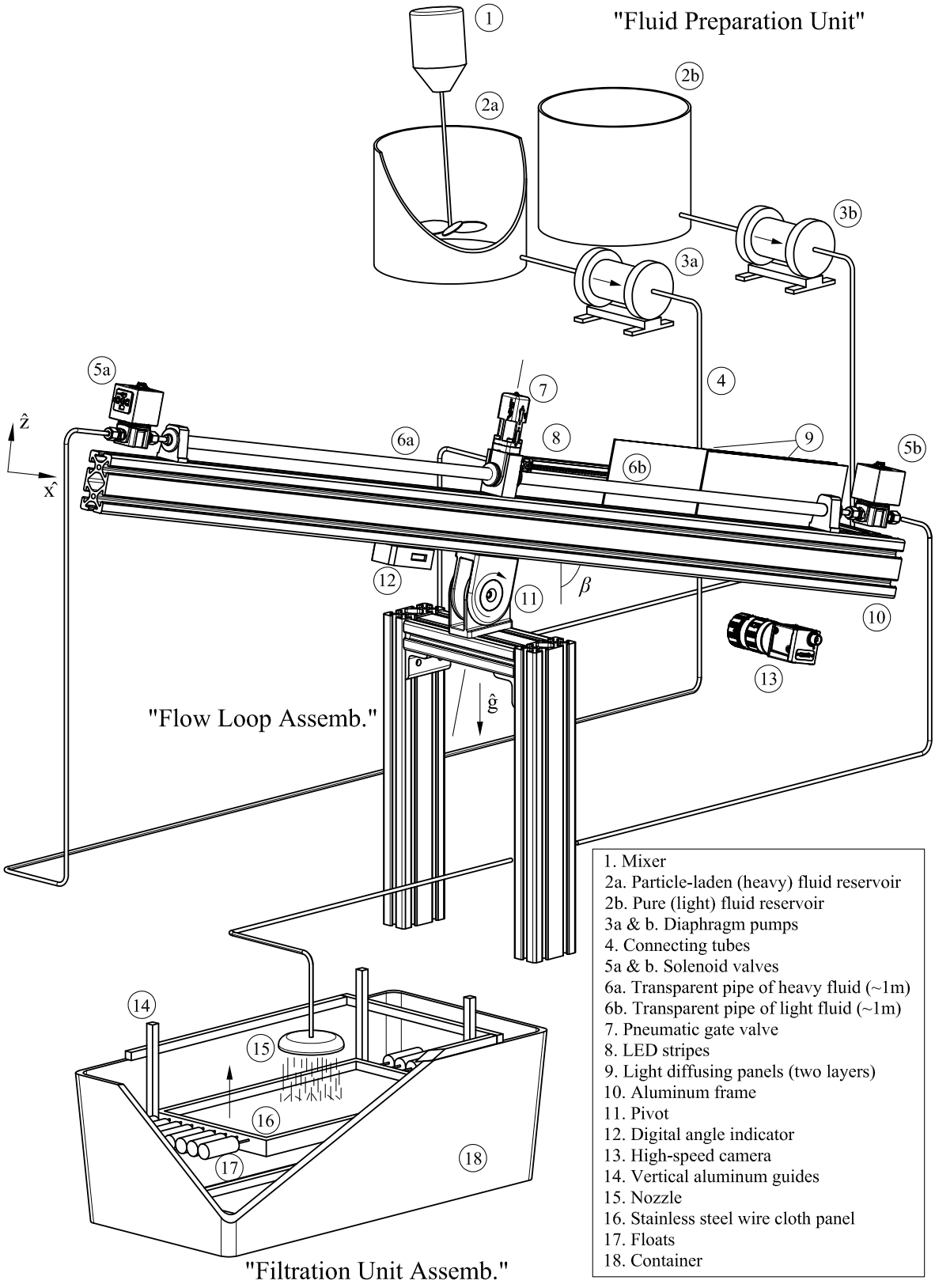

Figure 2.1: Schematic of the experimental apparatus. The entire pipe system can be tilted at an angle β, measured from vertical.

diaphragm pumps in order to facilitate experimental procedure, while minimizing the chance of non-homogeneity and Boycott flow development within the suspension layer prior to the gate release. In order to maintain a *lock-exchange* configuration, shut-off valves at two ends of the system are closed immediately after heavy and light fluids are in place. At the start of each experiment ($\hat{t} = 0$), the gate valve is opened allowing heavy particle-laden mixture to penetrate into the pure liquid ambient. Experiment continues until the heavy front reaches the opposite end of the pipe or halts at a run-out distance; whichever occurs first. Pipe is illuminated by placing Light-Emitting Diode (LED) stripes behind two light-diffusing panels to obtain a homogeneous lightening. Images are taken every 0.5 s using a high-speed camera (Basler Ace acA2040-90um CMOS, 2048^2 pixels) positioned at an adequately far location from the pipe. In post-processing of images, light intensity of each pixel is scaled onto a concentration value, $C(\hat{x}, \hat{z}, \hat{t})$ between 0 and 1, by applying the Beer-Lambert law [36]. Note that $C = 0$ and 1 values are assigned to the suspension and pure fluid respectively. The concentration values, C, less than 0, due to sedimentation of particles, are appointed the value 0 in order to consistently locate the frontal position and speeds across all experiments; see section 2.2.2 for details. A schematic post-processed image of the pipe with scaled light intensity is presented in the inset of figure. 2.1.

2.1.2 Range of parameters

Consistent with our recent theoretical work on the same topic [34], our experiments involve 9 independent *dimensional* parameters which we henceforth denote with a circumflex (^). The gravitational acceleration is denoted by $\hat{g}$, pipe diameter $\hat{D}$, and pipe length $\hat{L}$. Solid particles have density $\hat{\rho}_p$. The particles diameter, $\hat{d}$, is adequately large for suspension to be *non-Brownian* [37], whereas, it is relatively small compared to the pipe diameter i.e., 1 μm $\ll \hat{d} \ll \hat{D}$. Density and viscosity of carrying fluid (the same as light pure fluid) are $\hat{\rho}_f$, and $\hat{\mu}_f$, accordingly. Initial and

Table 2.1: List of *dimensional* independent parameters in the experiments.

Definition	**Parameter**	**Range**
Gravitational acceleration	$\hat{g}$	9.81 m s^{-2}
Pipe diameter	$\hat{D}$	9.53 mm
Pipe length	$\hat{L}$	2 m
Particle diameter	$\hat{d}$	40, 70 μm.
Particle density	$\hat{\rho}_p$	2500 kg m^{-3}
Pure fluid density	$\hat{\rho}_f$	1243.0, 1253.4 kg m^{-3}
Pure fluid viscosity	$\hat{\mu}_f$	0.367, 0.765 Pa s
Initial volume of particles	$\hat{V}_p$	3.56-35.59 cm^3
Jamming volume of particles	$\hat{V}_j$	47.69 cm^3

jamming volume of particles are $\hat{V}_p$ and $\hat{V}_j$ respectively. The latter depends on the shape and packing arrangement of particles [32]. A total of 7 independent *dimensionless* controlling parameters are evaluated [34], namely pipe aspect ratio, $\delta = \hat{D}/\hat{L} \ll 1$, angle of inclination β, particle-to-pipe-diameter ratio $r_p = \hat{d}/\hat{D} \ll 1$, particle-to-fluid-density ratio $\xi = \hat{\rho}_p/\hat{\rho}_f$, initial volume fraction of particles $\phi_0 = \hat{V}_p/\hat{V}_H$, jamming volume fraction $\phi_j = \hat{V}_j/\hat{V}_H$, and Reynolds number $Re_t = \hat{\rho}_H(\phi_0)\hat{V}_t\hat{D}/\hat{\mu}_H(\phi_0)$. Assuming that the suspension solution initially fills half of the pipe, the volume of the heavy solution, $\hat{V}_H$, is approximated as $\hat{V}_H = \pi\hat{D}^2\hat{L}/8$. The density of the suspension is expressible as $\hat{\rho}_H(\phi_0) = \hat{\rho}_p\phi_0 + \hat{\rho}_f(1-\phi_0)$ for ϕ_0 away from the packed limit ($\phi_0 \to \phi_j$) [38, 39]. The viscosity of the suspension may be captured via a Newtonian rheology in the form of $\hat{\mu}_H(\phi_0) = \hat{\mu}_f\left(1-\phi_0/\phi_j\right)^{-2}$ [40], in which, jamming volume fraction for spherical particles is proposed as $\phi_j \approx 0.61$ [32, 41]. The characteristic velocity, $\hat{V}_t$, in the Reynolds number expression is given by Eq. (2.1) [36]. The dimensional and dimensionless parameters governing the flow along with their range and values are listed in Tables 2.1 and 2.2, respectively. These parameters are also conveniently provided in figure. captions throughout this paper.

Our choices of particles are two different sizes of soda-lime glass microspheres (Cospheric LLC) with density $\hat{\rho}_p = 2500 \pm 50$ kg m^{-3}. First type involves smooth spheres with mean diameter 70 μm and standard deviation ≈ 5 μm , and the second type 40 μm with similar distribution. Particles are suspended within two dif-

Table 2.2: List of *dimensionless* independent parameters in the experiments.

Definition	**Parameter**	**Range**
Aspect ratio	$\delta = \frac{\hat{D}}{\hat{L}}$	4.8×10^{-3}
Pipe inclination angle	β	$0° - 88°$
Particle-to-pipe-diameter ratio	$r_p = \frac{\hat{d}}{\hat{D}}$	0.004, 0.007
Particle-to-fluid density ratio	$\xi = \frac{\hat{\rho}_p}{\hat{\rho}_f}$	1.99, 2.01
Initial volume fraction of particles	$\phi_0 = \frac{\hat{V}_p}{\hat{V}_H}$	0.05-0.50
Jamming volume fraction of particles	$\phi_j = \frac{\hat{V}_j}{\hat{V}_H}$	≈ 0.61
Reynolds number	$Re_t = \frac{\hat{\rho}_H(\phi_0)\hat{V}_t\hat{D}}{\hat{\mu}_H(\phi_0)}$	0.10-1.72

ferent aqueous glycerin solutions: First one with 93% glycerin-water concentration by weight with density $\hat{\rho}_f = 1243.0 \pm 0.1$ kg m^{-3} and viscosity $\hat{\mu}_f = 0.367 \pm 0.001$ Pa s. Second one is a 97% glycerin-water solution with density $\hat{\rho}_f = 1253.4 \pm 0.1$ kg m^{-3} and viscosity $\hat{\mu}_f = 0.765 \pm 0.001$ Pa s. We consider the same values for viscosity as reported in [42]. Suspension was prepared by weighting particles and fluid separately, pouring fluid first in a reservoir agitated by a heavy-duty mixer (IKA® Eurostar 200), and at the end adding the particles continuously but slowly. This procedure ensures maintaining a uniform and bubble-free mixture. In order to examine the accuracy of initial particle concentration after adding particles, we measured the densities of at least three samples of the mixture using a density meter (Attension® Sigma 701 module) with 0.1 kg m^{-3} resolution, and successfully verified the results with theory, $\hat{\rho}_H(\phi) = \phi_0\hat{\rho}_p + (1-\phi_0)\hat{\rho}_f$ (5 kg m^{-3} negligible error) [32]. Highly exothermic mixing was experienced due to the extreme shear forces inflicted by the mixer propeller on bulk of the viscous mixture. Therefore, for avoiding uncontrolled temperature variations, we immersed mixing chamber in a cold-water bath. Under this controlled condition, temperature always remained in the limit of $291 \sim 294$ K (measured by OMEGAETTE® HH308 thermometer with res. ± 0.1 K). Moreover, β is measured by an angle indicator with $\pm 0.1°$ resolution.

Three separate sets of experiments were designed covering angles $\beta \in [0° - 88°]$.

Table 2.3: List of experimental sets along with their corresponding parameter ranges.

	$\hat{d}$ (μm)	$\hat{\mu}_f$ (Pa s)	$\hat{\rho}_f$ (kg m^{-3})	$\hat{u}_0$ (mm s^{-1})	r_p	ξ
Set A	70	0.367	1243.0	0.009	0.007	2.01
Set B	40	0.367	1243.0	0.003	0.004	2.01
Set C	70	0.765	1253.4	0.004	0.007	1.99

First set includes 47 experiments involving particle size $\hat{d} = 70$ μm, and initial volume fractions $\phi_0 = \{0.05, 0.15, 0.30, 0.40, 0.50\}$. Particles are suspended in the less viscous 93 wt% aqueous glycerin solution. For investigating the effect of particle size, we consider the fluid in set B being the same as set A, while using smaller particles $\hat{d} = 40$ μm, with initial volume fractions $\phi_0 = \{0.05, 0.30, 0.50\}$ (21 experiments). For set C, we consider the more viscous 97 wt% solution. This set also consists of 21 experiments, designed to study the effect of interstitial fluid on the flow. Table 2.3 lists three sets of experiments and their assigned variables.

2.2 Results

2.2.1 Buoyancy-driven exchange flow of pure fluids in inclined pipes

Before proceeding to particle-laden limit, we first performed 33 experiments with pure fluids in order to: 1) Explore the effect of buoyant mixing in the absence of particles providing a basis for comparison with further suspension experiments. 2) Validate our experimental apparatus through benchmarking against the well-established results of Seon *et al.* (2005) and (2007), obtained for various density contrasts and tilt angles [16, 18]. Two major effects are observed as seen in figure 2.2a (The parameters are $\hat{\rho}_H = 1018.4\,\mathrm{kg\,m^{-3}}$, $\hat{\rho}_L = 998.1\,\mathrm{kg\,m^{-3}}$,$\hat{\mu}_H = \hat{\mu}_L = 1 \times 10^{-3}$ Pa s, $At = (1-\psi)/(1+\psi) = 0.01$, $\phi_0 = 0$, $Re_t = 291$, $\xi = 0$, and $r_p = 0$. The field of view is 2000×9.53 mm^2 in all the images). First, interpenetration in the form of quasi-parallel layers of heavy fluid, named *leading*, into the light pure one, termed as *trailing* over time is evident. Second, at angles away from horizontal, transverse mixing, in the form of Kevin-Helmholtz instabilities, homogenizes local density contrast at

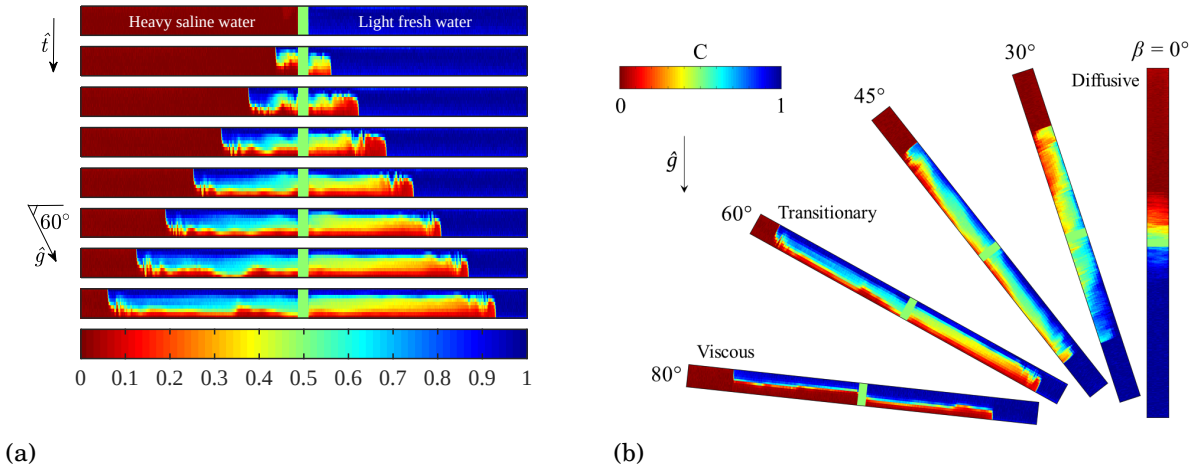

(a) (b)

Figure 2.2: (a) Sequence of experimental images for pure exchange flow obtained for $\beta = 60°$ at times $\hat{t} = [0, 5, 11, \ldots 32, 37]$ s. (b) Array of images over the full range of inclination angle, β, at $\hat{t} \approx 35$ s.

the interface [16]. Location of the interface between heavy ($C = 0$) and light ($C = 1$) fluids is obtained from the averaged concentration profile across the depth, $\bar{C}(\hat{x}, \hat{t})$ [35].

Similar to Seon *et al.* (2005) [16], we observed three different flow regimes by increasing β, i.e., decreasing inclination (figure 2.2b). I) *diffusive* : for pipes close to vertical, flow is turbulent and thoroughly diffusive meaning that the averaged concentration profile $\bar{C}(\hat{x}, \hat{t})$ follows a macroscopic diffusion law which is shown in our appendix; see also Ref. [18]. II) *Transitionary*: by further increasing β, mixing across the width of the pipe becomes weaker, and $\bar{C}(\hat{x}, \hat{t})$ no longer follows the diffusive law [16, 18]. Inertia is the dominant limiting process during the first and second flow regimes. III) *Viscous*: finally, heavy and light fronts steadily evolve over time in the form of separate counter-current fingers with minimal transverse mixing. Flow in this regime is controlled by viscous-buoyant stress balance. Seon *et al.* (2007) have shown in viscous regime except the particular case of horizontal pipe, the front always reaches a constant velocity [18]. Thus, in the following section, the special case of $\beta = 90°$ is excluded from our experiments for generality. See the appendix for quantitative classification of different flow regimes and benchmarking results.

2.2.2 Particle-laden exchange flows in near-horizontal angles: halt time and distance

Unlike interpenetrating flow of pure fluids in which buoyancy forces arise from the density difference between heavy fluid and light ambient (using salt), such forces in suspension gravity currents originate from denser particles in the mixture [32]. In near-horizontal pipes, upon releasing the gate, similar exchanging *leading* and *trailing* fronts are formed; see figure 2.3a. (The parameters are $\phi_0 = 0.30$, $\beta = 88°$, $\hat{d} = 70$ μm, $\hat{\mu}_f = 0.367$ Pa s, $\hat{u}_0 = 0.009$ mm s^{-1}, $\psi = 0.767$, $Re_t = 1.21$, $\xi = 2.01$, and $r_p = 0.007$. The field of view is 2000×9.53 mm^2). Flow develops through three stages after releasing the gate. During stages I and II, buoyant stress in order of $(\hat{\rho}_H - \hat{\rho}_L)\hat{g}\hat{D}$, is initially balanced by inertial stress as $(\hat{\rho}_H + \hat{\rho}_L)\hat{V}^2$, and later is controlled by viscous stress, $(\hat{\rho}_H + \hat{\rho}_L)\hat{\nu}_{av}\hat{V}/\hat{D}^2$. Here, $\hat{\nu}_{av}$ is the average kinematic viscosity of heavy and light fluids [16, 17]. Therefore, we have defined the respective characteristic velocities for *inertial* and *viscous* phases as

$$\hat{V}_t = \sqrt{\frac{1-\psi}{1+\psi}\hat{g}\hat{D}}, \tag{2.1}$$

$$\hat{V}_\nu = \frac{1-\psi}{1+\psi}\frac{\hat{g}\hat{D}^2}{\hat{\nu}_{av}}, \tag{2.2}$$

where, $\psi = \hat{\rho}_L/\hat{\rho}_H(\phi_0)$ is density ratio of the light fluid to heavy suspension. Saha *et al.* (2013) [32] showed an additional stage for flow in horizontal tilt angle, during which, particle settling gradually diminishes the driving buoyancy force through reducing the effective density difference (stage III).

Consequently, flow reaches an abrupt *halt* over a finite distance [32]. The behavior reported by Saha *et al.* (2013) [32] for horizontal duct ($\beta = 90°$), is found to persist in the slightly inclined pipe in our experiments ($\beta = 88°$). Henceforth, we use the word *sedimentary* as indication to this stage. Halt is evident in figure 2.3a where leading front remains almost immobile with time. There is also found a straight line

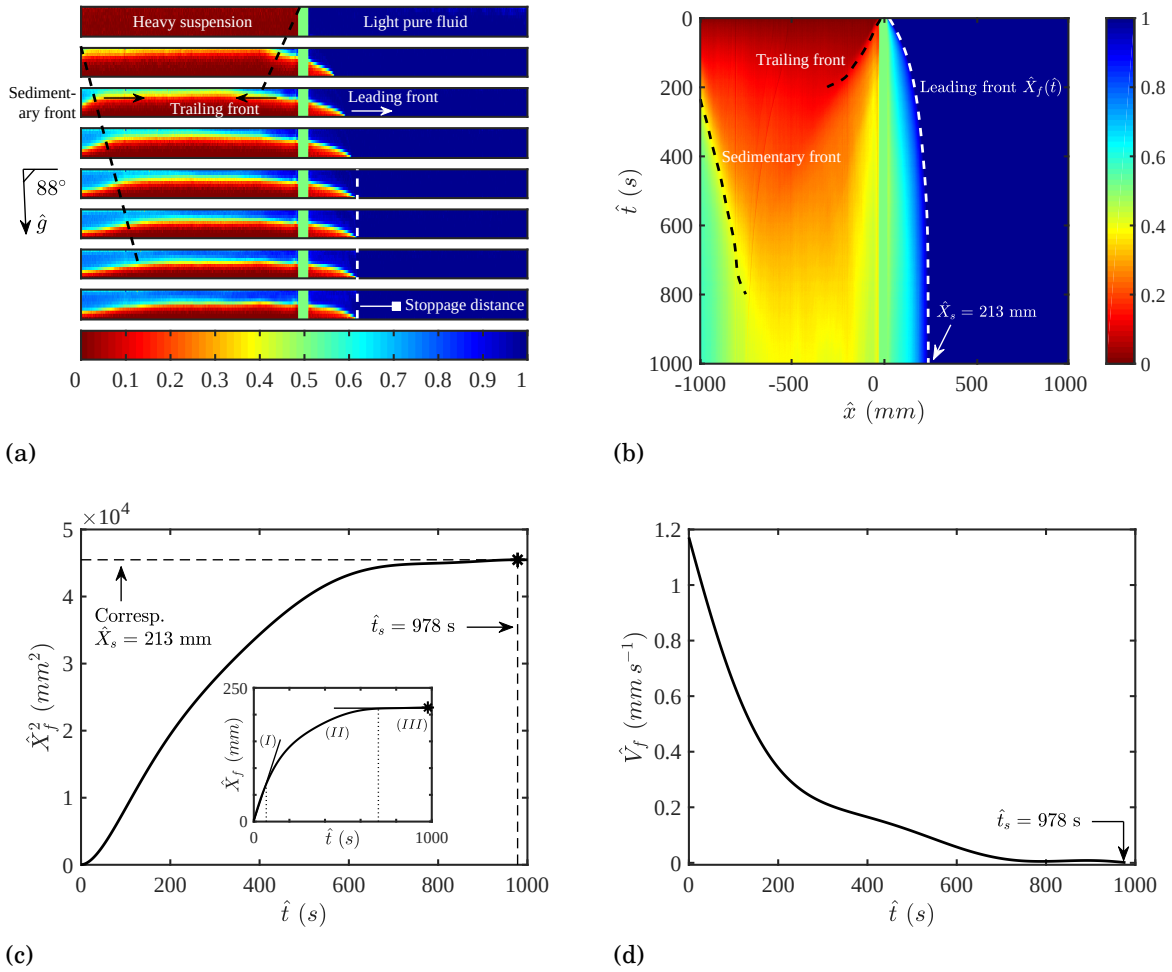

Figure 2.3: (a) Sequence of images at times $\hat{t} = [0, 136, 272, \ldots 816, 952]$ s , (b) spatio-temporal diagram of the depth-averaged concentration, (c) leading front's location , and (d) frontal velocity dependency on time for a suspension flow at near horizontal angle (set A).

corresponding to the halt distance which is evident from spatio-temporal diagram of the depth-averaged concentration in figure 2.3b. Settling rate is often expressed as the product of Stokes slip velocity of a single particle $\hat{u}_0 = (\hat{\rho}_p - \hat{\rho}_f)\hat{g}\hat{d}^2/(18\hat{\mu}_f)$ by Richardson-Zaki hindrance function, $(1-\phi_0)^5$ [43–45]. Thus, the characteristic slip velocity of the sedimentary phase, $\hat{u}_s$, is defined as

$$\hat{u}_s = \frac{r_p^2(\xi-1)(1-\phi_0)^5}{18}\frac{\hat{g}\hat{D}^2}{\hat{\nu}_f}, \tag{2.3}$$

with $\hat{\nu}_f$ being the kinematic viscosity of interstitial fluid. Note that ψ and ξ are convertible as $\psi = 1/(1+(\xi-1)\phi_0)$ [34].

Figure 2.3a further depicts the settling of particles from top part of the pipe towards the bottom. Due to the depthwise settling, trailing front created by light pure fluid disappears after a while (see third to fifth snapshots in figure 2.3a). The disappearance of the trailing front is accompanied by the formation of a *sedimentary* front on the very left hand side of the tube marked in figure 2.3a. As the flow halts, all the leading, trailing, and sedimentary fronts stop advancing (figures 2.3a & 2.3b). Location of the leading, trailing, and sedimentary fronts at any time are obtainable from the mean scaled concentration profiles $\bar{C}(\hat{x},\hat{t})$ [1]. The obtained values are then precisely fitted by ninth-degree polynomials. Results are displayed in spatio-temporal diagram (figure 2.3b) using white dashed line for leading and black for trailing and sedimentary fronts.

Leading front's location, $\hat{X}_f$, shown in figure 2.3c (inset), initially grows linearly with time, later deflects, and ultimately turns to a plateau as develops through inertial, viscous, and sedimentary phases respectively. Inertial-viscous transition ($\hat{t} \simeq 70$ s) as well as viscous-sedimentary changeover ($\hat{t} \simeq 700$ s) are also clearly evident in this figure. Notice that the front location in figure 2.3c is primarily expressed in the form $\hat{X}_f^2$ to be consistent with study of Saha *et al.* (2013) [32]. $\hat{X}_f$ is further

[1] The criteria for locating fronts are verified by those in previous works of the authors [13, 35, 36].

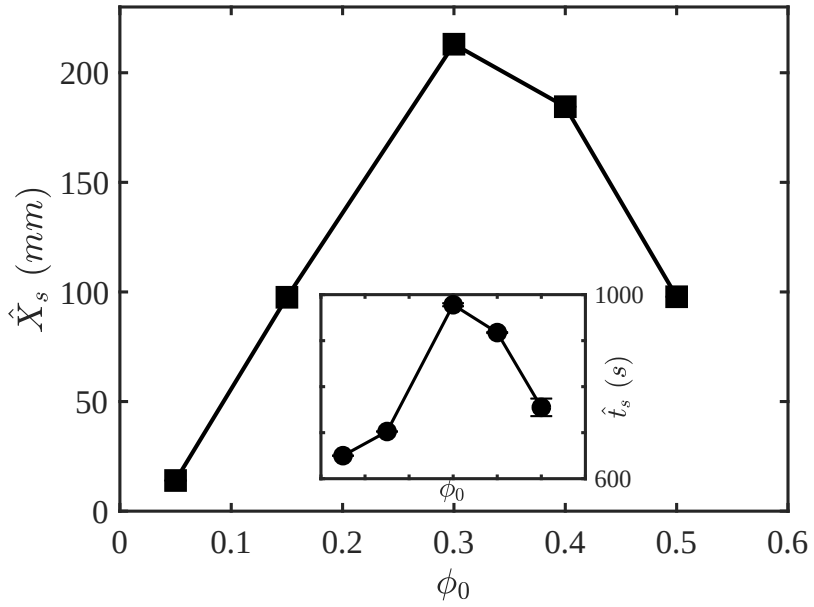

Figure 2.4: Variation of the stoppage distance $\hat{X}_s$, and time $\hat{t}_s$ (inset), with initial volume fraction of particles: $\phi_0 = \{0.05, 0.15, 0.30, 0.40, 0.50\}$, $\beta = 88°$, using set A.

used to calculate the instantaneous frontal velocity as $\hat{V}_f = d\hat{X}_f/d\hat{t}$. As seen in figure 2.3d, $\hat{V}_f$ gradually decreases to zero as flow comes to a halt at stoppage time, $\hat{t}_s$, corresponding to the distance, $\hat{X}_s$. We present halting time $\hat{t}_s$, and distance $\hat{X}_s$, in figure 2.4 for various initial volume fraction of particles, ϕ_0, for a slightly angled pipe, $\beta = 88°$. (Other parameters are $\hat{d} = 70$ μm, $\hat{\mu}_f = 0.367$ Pa s, $\hat{u}_0 = 0.009$ mm s^{-1}, $\psi = \{0.952, 0.868, 0.767, 0.712, 0.664\}$, $Re_t = \{1.37, 1.72, 1.21, 0.67, 0.22\}$, $\xi = 2.01$, and $r_p = 0.007$). Both curves in figure 2.4 interestingly depict a maximum over an intermediate particle concentration ($\phi_0 = 0.30$) which is consistent with findings of Ref. [32] obtained for a strictly horizontal channel. Error bars were small, thus not shown in this figure for clarity. This unique phenomenon can be described by looking into the competing effect of the viscosity and density of suspension. Basically, by increasing the initial volume fraction of particles ϕ_0, suspension's viscosity $\hat{\mu}_H(\phi_0) \propto (1 - \phi_0/\phi_j)^{-2}$ increases exponentially, neighboring infinity in the vicinity of packed limit ($\phi_0 \to \phi_j$). Meanwhile, density of suspension $\hat{\rho}_h(\phi_0) \propto \phi_0$ also increases

linearly with ϕ_0. As a result, in the dilute limit where viscosity is low, density difference is also small leading to a premature halt of the flow. Close to the packing limit, density difference is significant, yet the viscosity is extensively high so the flow remains almost immobile. This can explain the maximal halting time and distance corresponding to the intermediate ϕ_0.

2.2.3 Particle-laden exchange flows in inclined pipes

2.2.3.1 Principal characteristics

Pipe inclination transforms the behavior of flow by affecting settling and spreading processes [30]. Three distinct regimes are observed in our low-Reynlods-number experiments ($Re_t \in [0.10 - 1.72]$). i) At low particle concentrations, ϕ_0, and inclinations ($\beta \to 88°$), flow is primarily controlled by sedimentation and may halt at a finite location as explained in section 2.2.2. Halting occurs less frequently as the pipe is further inclined, in fact, none is observed for $\beta < 75°$ over the range of particle concentrations $\phi_0 = \{0.05, 0.15, 0.30, 0.40, 0.50\}$. The advancing suspension front position, $\hat{X}_f$, for such flows is curved and turns to a plateau; see figure 2.5a. (Parameters are $\phi_0 = 0.30$, $\hat{d} = 70$ μm, $\hat{\mu}_f = 0.367$ Pa s, $\hat{u}_0 = 0.009$ mm s^{-1}, $\beta = 30°, 75°$ & $88°$, $\psi = 0.767$, $Re_t = 1.21$, $\xi = 2.01$, and $r_p = 0.007$.) ii) At higher ϕ_0 and inclinations ($\beta \to 0°$), particles remain mixed in suspension, yet almost no significant mixing is present between two fluids. Leading and trailing fronts spread ceaselessly and linearly with time $\hat{t}$. Therefore, $\hat{X}_f$ follows a straight line (figure 2.5c), as one may face during viscous regime in pure-pure gravity exchange flows [16, 17]. iii) A *transitionary* domain exists between these two regimes, in which, flow manifests both *sedimentary* and *mixing* characteristics, i.e., the heavy front neither advances linearly nor comes to a halt. As a result, frontal displacement profile, $\hat{X}_f$, is curved but continues unceasingly; see figure 2.5b. It can also be shown that transition to mixing flows predominately occurs over angles closer to horizon and away from vertical direction.

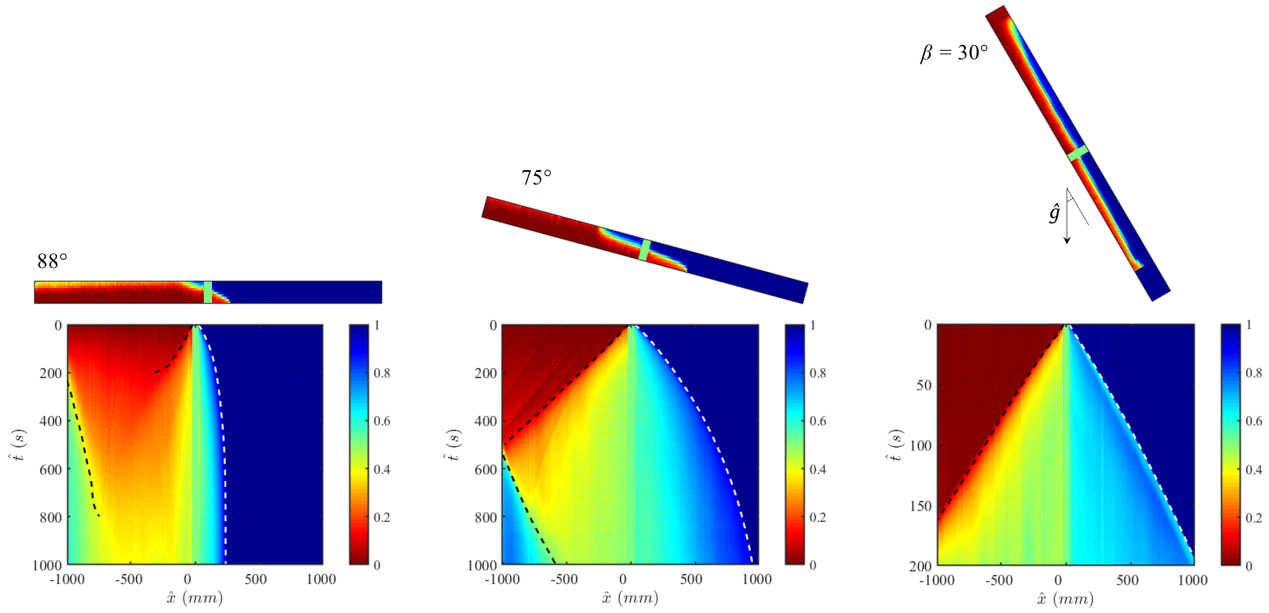

(a) Sedimentary (b) Transitionary (c) Mixing

Figure 2.5: Experimental images at $\hat{t} \approx 150\,\mathrm{s}$ (top) and corresponding spatio-temporal diagrams of the depth-averaged concentration (bottom) for three flow regimes (a) sedimentary, (b) transitionary, and (c) mixing.

In order to distinct the flow regimes from one another more effectively, $\hat{X}_f^2$ quantity versus time, $\hat{t}$, can be used as shown in figure 2.6. (Parameters are $\hat{d} = 70\ \mu\mathrm{m}$, $\hat{\mu}_f = 0.367\ \mathrm{Pa\,s}$, $\hat{u}_0 = 0.009\ \mathrm{mm\,s^{-1}}$, $\phi_0 = \{0.05, 0.15, 0.30, 0.40, 0.50\}$, $\psi = \{0.952, 0.868, 0.767, 0.712, 0.664\}$, $Re_t = \{1.37, 1.72, 1.21, 0.67, 0.22\}$, $\xi = 2.01$, and $r_p = 0.007$.) Upward-facing curves growing unboundedly with time, are related to the mixing regime. Oppositely, downward-facing curves progressing slowly to a halt are categorized under the sedimentary regime. Other types of profiles which follow neither trends, including irregular curves (figures 2.6a-2.6c) and straight lines (figures 2.6d and 2.6e), belong to the transitionary regime. It is evident from figure 2.6 that the transitionary flows occur over a very narrow range of inclination angles. To capture these flows we had to precisely design additional experiments.

It is appropriate at this stage to look into the timescales over which the sedimentary, mixing, and transitionary processes take place and examine their variation with inclination angle. Timescale pertaining to streamwise spreading is given as

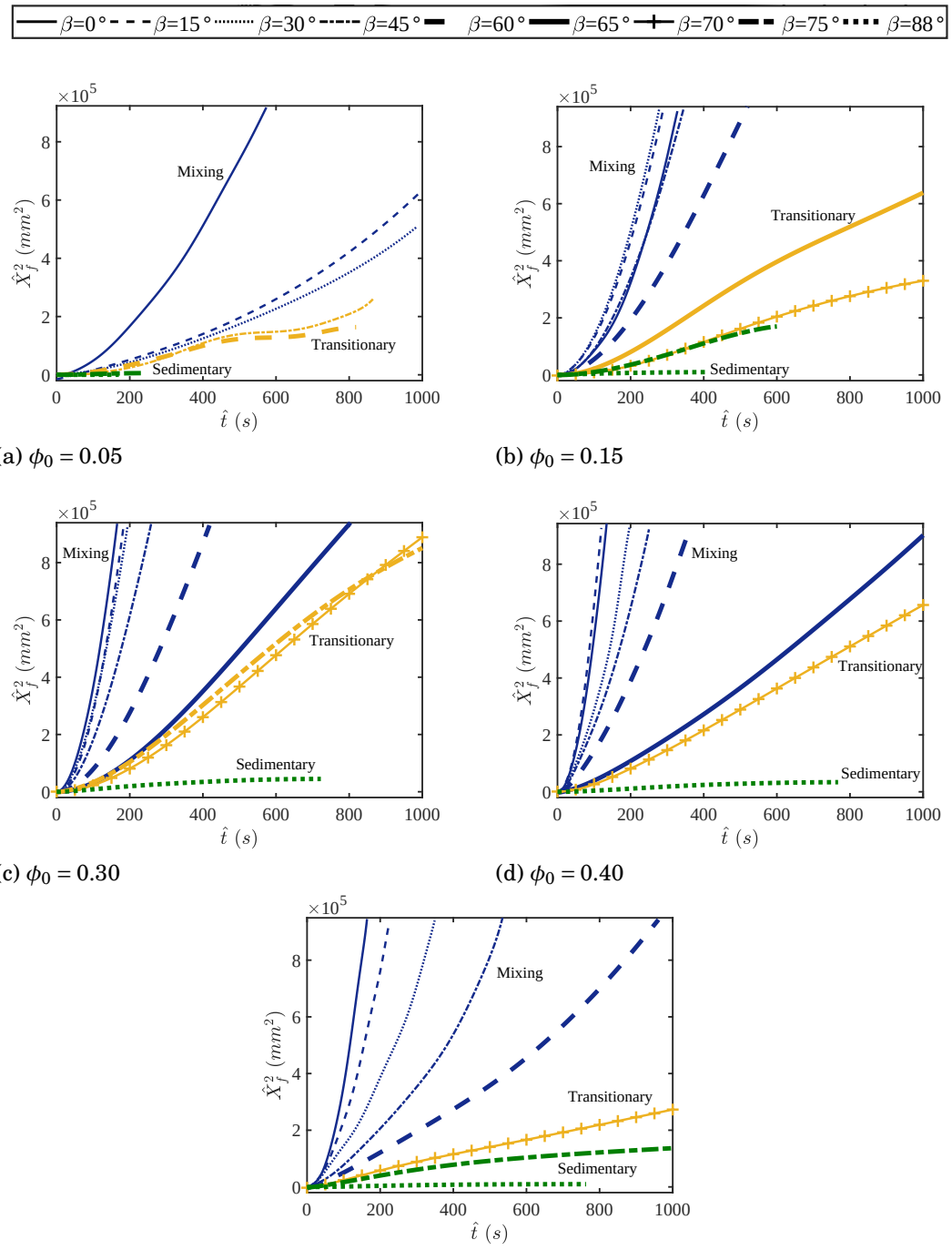

(a) $\phi_0 = 0.05$

(b) $\phi_0 = 0.15$

(c) $\phi_0 = 0.30$

(d) $\phi_0 = 0.40$

(e) $\phi_0 = 0.50$

Figure 2.6: Front position, $\hat{X}_f^2(\hat{t})$, over time, $\hat{t}$, for various angles of inclination and phi_0 corresponding to the experiments in set A. Colors correspond to sedimentary (green), transitionary (yellow), and mixing (blue) regimes.

$\hat{D}/(\delta\hat{V}_v\cos\beta)$. For sedimentation, however, the timescale is defined as $\hat{D}/(\hat{u}_s\sin\beta)$ with length scale $\hat{D}/\sin\beta$ being approximately the depth of suspension at each angle. By increasing β, i.e., moving away from vertical, the timescale of streamwise advancement increases monotonically, while the sedimentation timescale decreases from infinity. Therefore, the sedimentary flow is expected to emerge in near-horizontal angles and mixing at higher inclination as also observed in the experiments.

Zhou *et al.* (2005) presented a similar classification for free-surface particulate film flow over a slope [30]. They reported three distinct settling behaviors: at low concentrations, ϕ_0, and inclinations (large β), particles settle out of the flow and aggregate at the bottom. At intermediate ϕ_0 and β, suspension remains well mixed. And at higher ϕ_0 and inclinations (smaller β), particles are transported faster than fluid, accumulating in a thick ridge in the vicinity of the advancing contact line. Similar behaviors of the first and second regimes in Zhou *et al.* (2005) are also observed in downstream pipe section in our experiments corresponding to "sedimentary" and "mixing" regimes. Nevertheless, our results show no particle enrichment near the tip of the front; see figure 2.7 for images over full range of parameters. Accumulation may occur as a result of relative transportation rate of solid and fluid [30, 31]. Zhou *et al.* (2005) [30] expressed that the relative velocity solid-fluid is proportional to the particle settling rate $\hat{u}_s$, which in our experiments is estimated as typically $O(10^{-4})$ weaker than characteristic velocity $\hat{V}_v$. Therefore, particles remain rather immobile with respect to fluid in streamwise direction. Still in the depthwise direction, volume fraction may increase with depth by settling or decrease by the particle flux due to the gradients in concentration and shear stress [46–48]. Mirzaeian & Alba (2018) [34] showed that in narrow vertical channels shear-induced migration effect may be neglected in front of settling one if the ratio of their

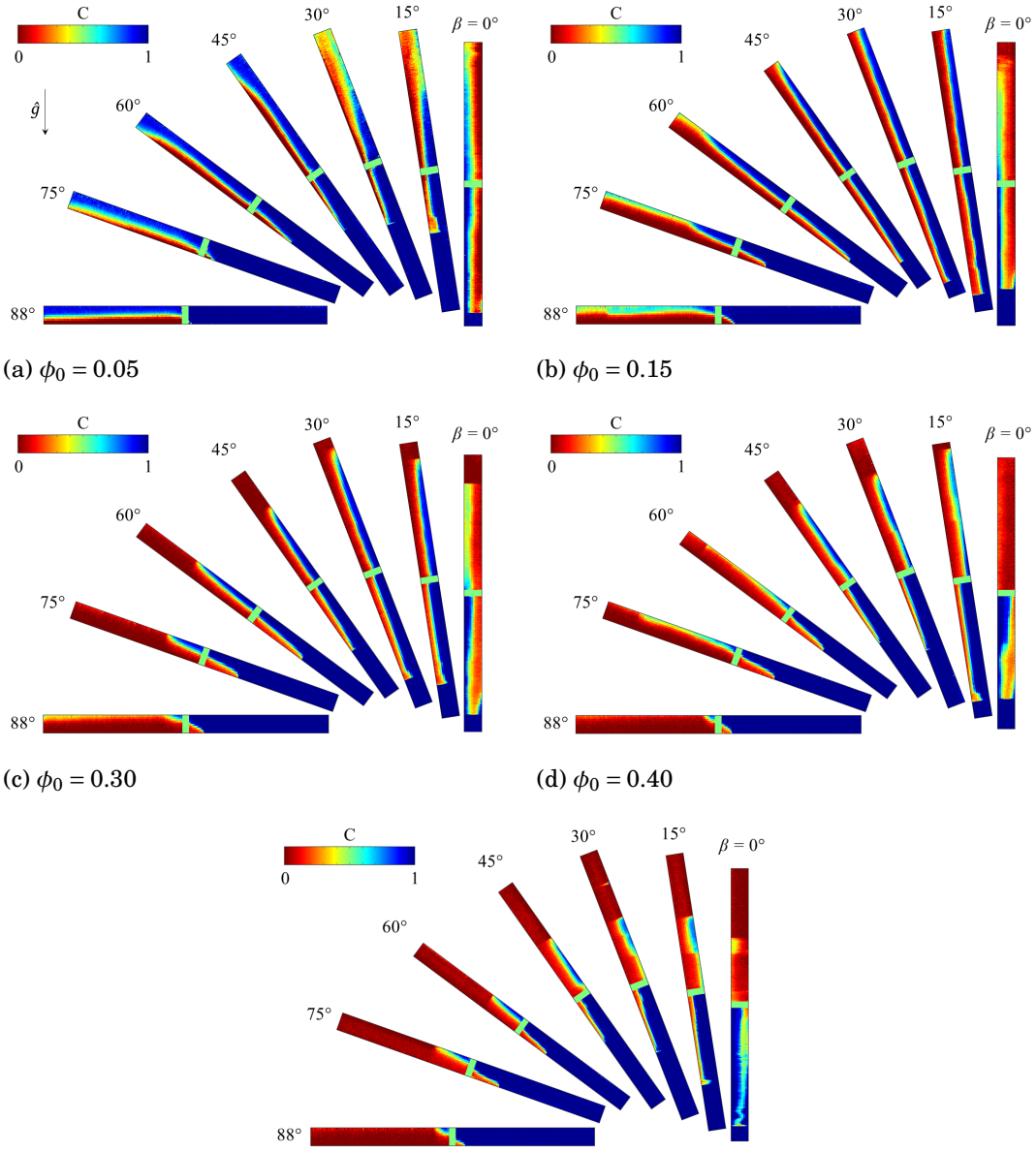

(a) $\phi_0 = 0.05$

(b) $\phi_0 = 0.15$

(c) $\phi_0 = 0.30$

(d) $\phi_0 = 0.40$

(e) $\phi_0 = 0.50$

Figure 2.7: Array of experimental images at various angles for same experiments as in figure 2.6 recorded at: (a) $\hat{t} = 484 \pm 32$ s, (b) $\hat{t} = 248 \pm 12$ s, (c) $\hat{t} = 141 \pm 13$ s, (d) $\hat{t} = 101 \pm 9$ s, and (e) $\hat{t} = 153 \pm 35$ s. View: 2000×9.53 mm^2.

fluxes (in m/s),

$$\frac{\hat{J}_{Migration}}{\hat{J}_{Settling}} = \frac{9K_v(1-\phi_0/\phi_j)^2}{\psi(\xi-1)}\frac{1-\psi}{1+\psi}, \tag{2.4}$$

is infinitesimal. Constant $K_v \approx 0.62$ corresponds to shear-induced particle flux due to gradient in effective viscosity of the suspension [47]. The ratio in Eq. (2.4) is approximately 0.05-0.25 for our range of study, implying that the migration effects may not be too small in presented experiments (up to 25 % of settling flux). As a visual example, consider the experiment at $\beta = 60°$ in figure 2.7b. For this experiment at $\hat{t} \approx 248$ s with $\hat{u}_s = 0.004$ mm s^{-1}, a sediment layer with 1 mm thickness is expected (pipe width is approximately 10 mm). However, the concentration across thickness of the leading front seems to be uniform in this figure. One may relate the reduced particle settling to the migration flux due to high shear rate at this angle.

Let us now focus on the irregular protuberance observed at the forefront of some experiments, for example the one at $\beta = 15°$ with $\phi_0 = 0.30$ in figure 2.7c. For a closer look, consider Fig 2.8 showcasing this experiment. (Parameters are $\phi_0 = 0.30$, $\beta = 15°$, $\hat{\mu}_f = 0.367$ Pa s, $\hat{u}_0 = 0.009$ mm s^{-1}, $\psi = 0.767$, $Re_t = 1.21$, $\xi = 2.01$, and $r_p = 0.007$.) The mean concentration, $\bar{C}$, in the right-hand pipe is presented for a sequence of recordings in this figure. It is clear that the spike in concentration at the advancing front is caused by a bump at the tip of the leading front. In the absence of particle enrichment close to the front, such bump is solely controlled by three-dimensional inertial effects [17, 49]. Similar patterns are often observed in our experiments with intermediate volume fraction ϕ_0, and in pipes tilted away from horizontal ($\beta \to 0°$); see for example $\beta = 15°$ and $30°$ in figures 2.7b-2.7d. The height and stretch length of these bumps may vary with ϕ_0 and β; see figure 2.7. Further detailed analysis of ridge formation at the front is beyond the scope of this paper.

We have summarized flow classification results for set A in the phase diagram of figure 2.9a. (Parameters are $\phi_0 = \{0.05, 0.15, 0.30, 0.40, 0.50\}$, $\hat{d} = 70$ μm, $\hat{\mu}_f = 0.367$ Pa s, $\hat{u}_0 = 0.009$ mm s^{-1}, $\psi = \{0.952, 0.868, 0.767, 0.712, 0.664\}$, $Re_t =$

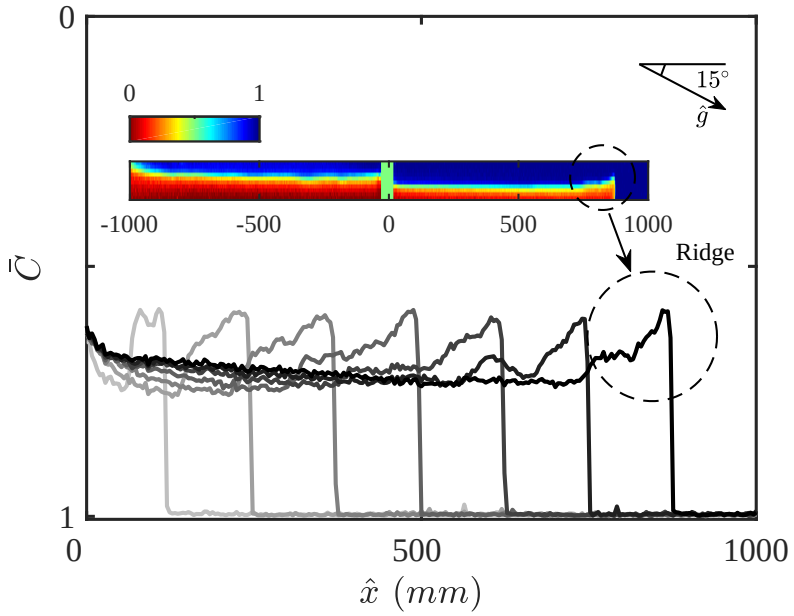

Figure 2.8: Concentration profiles on the right-hand side of the pipe at times $\hat{t} = [0, 23, 46 \ldots 138, 161]$ s, showing the formation of a ridge close to the front region.

$\{1.37, 1.72, 1.21, 0.67, 0.22\}$, $\xi = 2.01$, and $r_p = 0.007$.) Mixing cases shown by (■) belong to a domain as specified by intermediate particle concentration and high inclination (see area below the dashed line). We expect to find fewer mixing flows in dilute limit ($\phi_0 \to 0$) and none at $\phi_0 = 0$, where there is no driving density difference to set off the exchange flow. The same trend is presumed for the packed limit ($\phi_0 \to \phi_j$) where effective viscosity $\hat{\mu}_H(\phi_0) = \hat{\mu}_f(1 - \phi_0/\phi_j)^{-2}$ becomes extremely high so that suspension will be overly packed and almost immobilized. This explains the predicted deflection of mixing domain's bound near higher volume fraction, ϕ_0, in figure 2.9a. Furthermore, due to strong sedimentation in the limit of near-horizontal pipes ($\beta \to 90°$), all experiments in this angle are classified as sedimentary and shown by (●) in the phase diagram. Few sparse transitionary data points adjacent to the mixing domain are also shown in this figure as (▲) which make up for approximately 20% of all cases. The experiments with and without a ridge at the leading front are also marked in figure 2.9a, stretching over medium ϕ_0 and small β. The implication

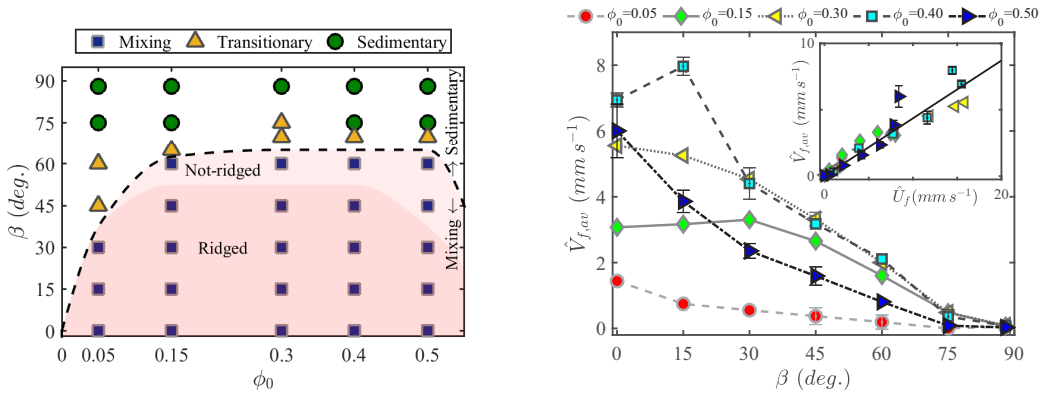

(a) (b)

Figure 2.9: (a) Phase diagram, and (b) variation of the mean frontal velocity $\hat{V}_{f,av}$, versus angle of inclination β, for experiments in set A. The fitted line in inset is given by Eq. (2.6) with $C_F = 0.435$.

is that at least some forms of inertial bump appear in majority of mixing experiments.

An important characteristic which is of interest to geophysical and industrial processes is how fast the heavy suspension layer advances within duct upon its release into a light ambient. We have obtained the mean frontal velocity, $\hat{V}_{f,av}$, by averaging $\hat{V}_f$ at long times when the flow proceeds steadily (variation in velocity is less than 10%). Figure 2.9b presents measured mean frontal velocities for all the experiments in set A. $\hat{V}_{f,av}$ grows expectedly with inclination (or decrease in β) since the driving buoyancy force in streamwise direction increases (depthwise sedimentation also decreasing). Furthermore, higher velocities are interestingly found over an intermediate range of particles volume fraction, away from dilute ($\phi_0 = 0.05$) and dense limits ($\phi_0 = 0.50$). This phenomenon can be explained by considering the intricate effect of ϕ_0 on heavy fluid's density and viscosity. The ratio of density of light to heavy fluid, $\psi = \hat{\rho}_L/\hat{\rho}_H(\phi_0)$, decreases with ϕ_0, ultimately resulting in a larger driving buoyancy force (increasing $\hat{V}_{f,av}$). In the vicinity of packing concentration, however, effective viscosity $\hat{\mu}_H(\phi_0)$, grows exceedingly ($\hat{\mu}_H(\phi_0) \propto (1-\phi_0/\phi_j)^{-2}$); viscous dissipation is strong and flow motion is highly restrained (decreasing $\hat{V}_{f,av}$). That is why a maxi-

mal interpentration rate, $\hat{V}_{f,av}$, is achieved over an intermediate volume fraction.

Let us now investigate whether the dimensional front speeds in figure 2.9b can be predicted (scaled) using an appropriate velocity scale. Herbolzheimer & Acrivos (1981) suggested that for batch sedimentation (Boycott flow), the motion of the descending suspension/clear-fluid interface to be enhanced according to $\Lambda^{1/3}\cos^2\beta$ [27]. Here, $\Lambda = 18\phi_0/[(1-\phi_0)^5 r_p^2]$ is the ratio of the sedimentation Grashof number to Re_t, representing the combined effects of pipe geometry and kinematics of sedimentation. In our case, since we face an exchange flow between the heavy and light phases, governed by viscous-buoyant stress balance (Eq. 2.2), $\Lambda^{1/3}\cos^2\beta$ enhancement term may be multiplied by $\hat{V}_v$. In other words, a velocity scale, $\hat{U}_f$, may be constructed as

$$\hat{U}_f = \hat{V}_v \Lambda^{1/3}\cos^2\beta. \tag{2.5}$$

The inset in figure 2.9b does, in fact, reveal the successfulness of such scaling. Except for the vertical pipe (high $\hat{U}_f$ values in figure 2.9b), velocities collapse agreeably on a line given as

$$\hat{V}_f = C_F \hat{U}_f, \tag{2.6}$$

with $C_F = 0.435$ being the curve-fitted slope. In fact, $\hat{U}_f$ can be $\sim O(10^2)$ greater than characteristic velocity of the pure viscous flow, $\hat{V}_v$. Therefore, we can substantiate that Boycott-type enhanced flow rate in the clarified layer which is exclusively revealed in suspension exchange flows in inclined pipes, indeed facilitates evolution of fronts. Nonetheless, the same statement is simply invalid for the vertical pipe where such an effect is nonexistent.

2.2.3.2 Effect of particle size

For a comprehensive and independent evaluation of each flow parameter in particle-laden exchange current, the density mismatch of heavy and light

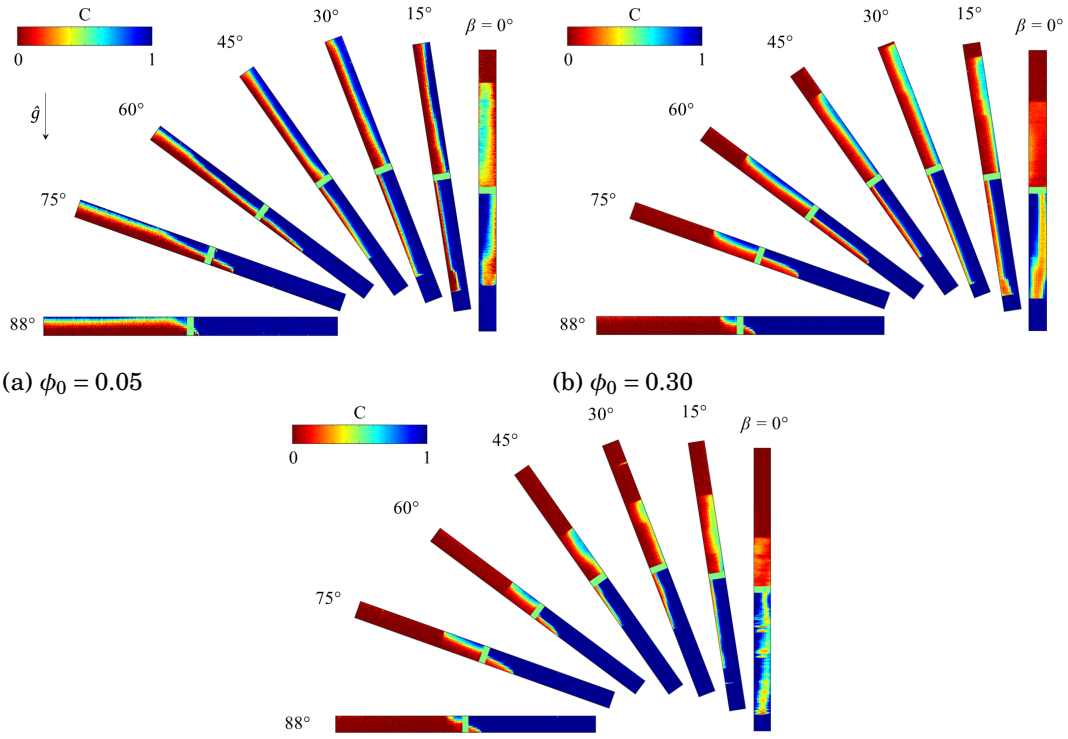

(a) $\phi_0 = 0.05$ (b) $\phi_0 = 0.30$

(c) $\phi_0 = 0.50$

Figure 2.10: Array of experimental images at various angles corresponding to the experiments of set B recorded at (a) $\hat{t} = 778 \pm 51$ s, (b) $\hat{t} = 200 \pm 26$ s, and (c) $\hat{t} = 165 \pm 59$ s. View: 2000×9.53 mm^2.

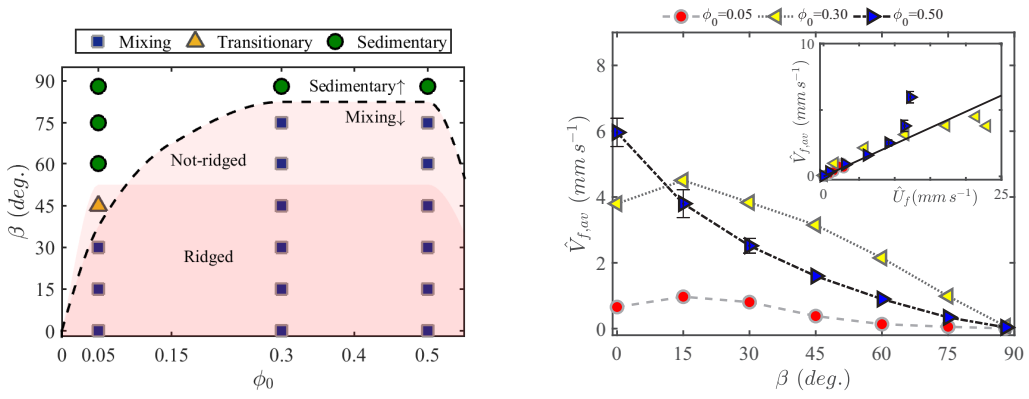

(a) (b)

Figure 2.11: (a) Phase diagram, and (b) variation of the mean frontal velocity $\hat{V}_{f,av}$, versus angle of inclination β, for experiments in set B. The fitted line in inset is given by Eq. (2.6) with $C_F = 0.244$.

phases, $\psi = 1/(1+(\xi-1)\phi_0)$, is preserved throughout all three experimental sets ($\xi = \hat{\rho}_p/\hat{\rho}_f \approx 2$). The settling velocity, $\hat{u}_0$, is then reduced via two ways: 1) Using smaller particles, results of which are presented in this section. 2) Choosing a more viscous fluid (to be presented in section 2.2.3.3). We have carried out a total of 21 experiments using smaller particles of the same density, shape, and distribution within the same fluid; see set B in Table 2.3. Range of initial particle concentration is $\phi_0 = \{0.05, 0.30, 0.50\}$, and experiments cover full range of inclination angles ($\beta \in [0°, 88°]$). Herein, only parameters involving particle size $\hat{d}$, such as particle-to-pipe-diameter ratio r_p, and the settling velocity $\hat{u}_s \propto r_p^2$ are reduced; see Eq. (2.3). All the other parameters in Tables 2.1 and 2.2 remain unchanged; see snapshots of set B experiments given in figure 2.10. (Parameters are $\hat{d} = 40$ μm, $\hat{\mu}_f = 0.367$ Pa s, $\hat{u}_0 = 0.003$ mm s^{-1}, $\phi_0 = \{0.05, 0.30, 0.50\}$, $\psi = \{0.952, 0.767, 0.664\}$, $Re_t = \{1.37, 1.21, 0.22\}$, $\xi = 2.01$, and $r_p = 0.004$.)

We use similar method as explained previously to classify the flow and present the results in figure 2.11a. Interestingly, the boundary of the mixing regime is slightly shifted upward, meaning that the transition from sedimentary to mixing flows occurs even at closer angles to the horizontal direction. This behavior is well expected since the buoyant stress, scaled as $(1-\psi)\hat{g}\hat{D}$, is unaffected by the change of particle size $\hat{d}$, meanwhile reduced sedimentation lets particles stay mixed in the flow for a longer time. It is also very interesting that the periphery of the ridged domain in the phase diagram remains rather untouched regardless of the particle size; compare figure 2.11a with figure 2.9a. This reiterates the fact that in the absence of significant relative velocity between solid and fluid phases along the pipe, bumps originate from the inertial effects at the tip and are certainly independent of settling behavior of particles. Through visual examples of the experiments in figure 2.10, it can be also observed that the particle-enrichment is insubstantial along the leading front; for example, see the image at $\beta = 75°$ with $\phi_0 = 0.30$ in this figure.

Apart from the vertical pipe ($\beta = 0°$), the trends in $\hat{V}_{f,av}$ for experiments with smaller particles (set B) in figure 2.11b, seem to be consistent with those of larger particles (set A shown previously in figure 2.9b). Front velocity consistently decreases with β and is maximal over an intermediate ϕ_0 range. The decrease in particles' settling rate does not have a sizable impact on the advancement of front; compare $\hat{V}_{f,av}$ values between figures 2.9b and 2.11b. The scaled results presented in the inset of figure 2.11b, display a collapse on a line with the equation in form of Eq. (2.6) with the constant $C_F = 0.244$. Note that C_F has decreased equiproportional with r_p in experiments of set B with respect to set A, implying that $C_F = f(r_p)$.

2.2.3.3 Effect of fluid's viscosity

The fluid's viscosity, $\hat{\mu}_f$, affects the flow behavior remarkably by controlling: 1) settling rate $\hat{u}_s \propto 1/\hat{\mu}_f$ (see Eq. (2.3)), and simultaneously 2) The spreading rate through adjusting the effective viscosity of suspension $\hat{\mu}_H(\phi_0) = \hat{\mu}_f(1 - \phi_0/\phi_j)^{-2}$. We have designed 21 additional experiments by suspending the same particles of set A, this time, in a fluid almost twice as viscous with nearly the same density (variation was $< 1\%$; see set C in Table 2.3). As a consequence, $\hat{\mu}_H$ is increased, thus lowering $\hat{u}_s$ and Re_t, while all other parameters remain unchanged. See figure 2.12 for the experimental images belonging to set C. (Parameters are $\hat{d} = 70$ μm, $\hat{\mu}_f = 0.765$ Pa s, $\hat{u}_0 = 0.004$ mm s^{-1}, $\phi_0 = \{0.05, 0.30, 0.50\}$, $\psi = \{0.953, 0.770, 0.668\}$, $Re_t = \{0.66, 0.58, 0.10\}$, $\xi = 1.99$, and $r_p = 0.007$.) Counterintuitively, extents of domains in the phase diagram given in figure 2.13a are in identical fashion of those in set A shown in figure 2.9a. It is valid to conclude that the fluid's viscosity consistently influences the settling and spreading processes to the same extents, thus the regime transition is immaterial of $\hat{\mu}_f$. Nevertheless, by increasing the viscosity of fluid, $\hat{V}_{f,av}$ decreases in all experiments with regard to set A; compare the results in figure 2.13b to figure 2.9b. Note that by increasing $\hat{\mu}_f$ both the viscosities of sus-

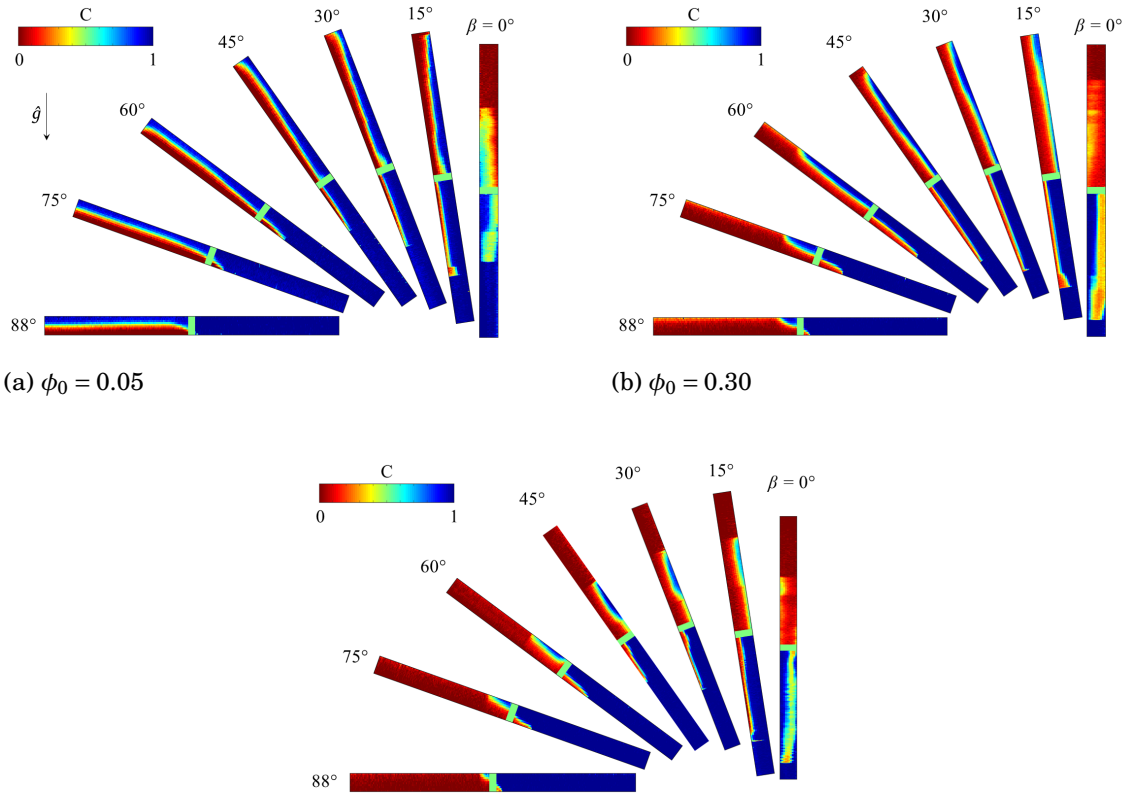

(a) $\phi_0 = 0.05$ (b) $\phi_0 = 0.30$

(c) $\phi_0 = 0.50$

Figure 2.12: Array of experimental images at various angles corresponding to the experiments of set C recorded at (a) $\hat{t} = 882 \pm 52$ s, (b) $\hat{t} = 323 \pm 42$ s, and (c) $\hat{t} = 251 \pm 18$ s. View: 2000×9.53 mm^2.

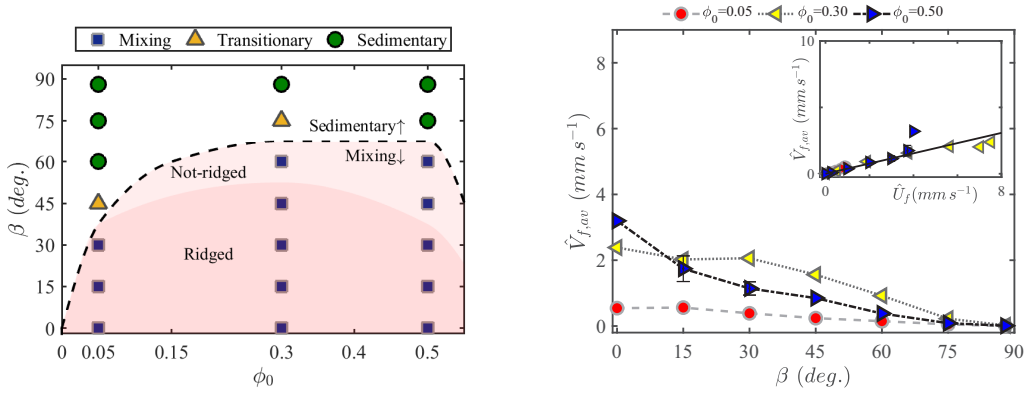

(a) (b)

Figure 2.13: (a) Phase diagram and (b) variation of the mean frontal velocity $\hat{V}_{f,av}$, versus angle of inclination β, for experiments in set C. The fitted line in inset is given by Eq. (2.6) with $C_F = 0.385$.

pension and pure phases are increased leading to overall flow slowdown (decrease in $\hat{V}_{f,av}$).

Again, here the scaled velocities collapse onto a line similar to Eq. (2.6) with the slope $C_F = 0.385$. This constant also varies adversely with the viscosity, suggesting that in general $C_F = f(r_p, \hat{\mu}_f)$. Therefore, it is advised that C_F values given in this manuscript are valid only over certain range of flow parameters and should not be generalized to different circumstances (see Tables 2.1 and 2.2).

Chapter 3: Modeling

In the previous chapter we identified distinct sedimentary, transitionary, and mixing flow regimes depending on different combinations of parameters. It was shown that flow often manifests mixing behavior over the range of intermediate ϕ_0, and in pipes with high inclination (lower β). It was also revealed that the average velocity of the advancing front $\hat{V}_{f,av}$, follows a scaling paradigm as expressed in Eq. (2.6). Vertical pipe case ($\beta = 0^\circ$), however, is exempt from this model in the absence of Boycott-type settling mechanism. Such a flow is crucially important in oil well construction during the vertical drilling/cementing stages. Therefore, an accurate assessment of the scale of frontal velocity in the vertical pipe, requires a precise mathematical modeling of the problem. Furthermore, such a model enables us to examine the particle-enrichment phenomenon which was absent in our experimental results by adopting proper flow parameters.

Lubrication approximation can be applied to model flows in buoyant-viscous domain with negligible inertia. A continuum 1D lubrication model of a particle-laden film flowing down a slope was first developed by [30], predicting the evolution of the interface height, h, and particle volume fraction, ϕ, with time, t, and streamwise distance, x. References [30, 31, 48] reported the formation of a particle-rich ridge in the vicinity of the advancing suspension front (contact line) due to different rates of solid and fluid transport. Two-dimensional effects were later studied in [50], revealing that the addition of solid particles can diminish well-known fingering instabilities of an advancing contact line. While there is a large body of studies on modeling single-layer suspension film flows, the literature on two-layer exchange systems of suspension and pure fluid lacks severely. As a novel approach, we extend the methodology of [30] for free-surface film flows to a practical exchange system within confined (duct)

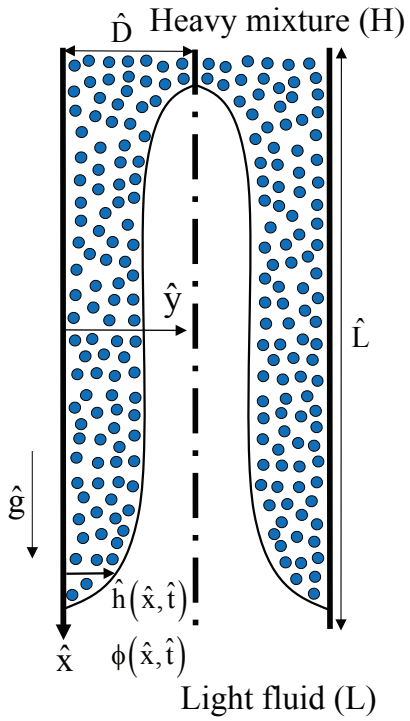

Figure 3.1: Schematic of the symmetric particle-laden exchange flow in a vertical 2D duct used in the lubrication model analysis. Note that dimensional notations are used in the figure. The interface shape is illustrative only.

geometry. As discussed in [51], the exchange flow of two fluids in a vertical duct may reveal slumping side-by-side or symmetric patterns with either heavy or light fluids moving in the core region of the duct. In particular, we are interested in the symmetric mode where the heavy particle-laden film falls along the side walls and the light fluid moves upward in the center of the duct; see figure 3.1. From a different perspective, the examined exchange flow can be considered as an extension to the fundamental *Taylor bubble* problem of [52], now studied for particle-laden fluids.

In this chapter, a more comprehensive scenario is considered where the carrying and light can be different from one another (same-fluid assumption in experiments of chapter 2). Therefore, two new dimensional parameters, i.e., carrying fluid density $\hat{\rho}_{f,H}$, and viscosity $\hat{\mu}_{f,H}$ are introduced to the problem. Accordingly, the new dimensionless parameters involving carrying fluid are obtained, e.g., light-to-carrying-fluid density and viscosity ratios, denoted by η and κ, respectively. Also, note that the par-

ticle size here is presented by its radius $\hat{a}$, whereas duct width is considered $2\hat{D}$. All other non-dimensional parameters are adjusted accordingly and explained throughly in the section 3.1. This study is further extended by investigating the variation of interpenetrating rate as well as particle concentration within the suspension layer along the vertical pipe analytically, for a wide range of controlling parameters. This includes the effects of density, size, and volume fraction of particles, as well as viscosity and density of light and carrying fluids, and Reynolds number. Results are presented in dimensionless interface height and concentration figures which are further discussed throughout this chapter. A last note here is that the developed model is only applicable to highly *viscous* regimes and it is unable to capture interfacial instabilities due to the inherent lubrication model assumption used (negligible inertia) [19]. The stability of thin pure fluid films were extensively studied in the previous works [20, 53, 54] via a Weighted Residual (WR) model. Extending the current particle-laden formulation to a similar WR model, capable of capturing instabilities, is extremely challenging due to the addition of weakly inertial terms in Navier-Stokes equations.

3.1 Dimensional and dimensionless governing parameters

The problem shown schematically in figure 3.1 involves 11 *dimensional* parameters which we denote with $\hat{}$ symbol. The gravitational acceleration is denoted by $\hat{g}$. The vertical duct has width, $2\hat{D}$, and length, $\hat{L}$. The duct geometry considered may simulate particle-laden groundwater flows through aquifers, conduits, caves, cracks, joints, and faults. To capture the fully-developed flow effects as discussed in [13], we assume $\hat{L} \gg \hat{D}$. The solid particles, which are considered to be heavier than the carrying fluid (negatively buoyant), have radius, $\hat{a}$, and density, $\hat{\rho}_p$. Particularly, we are interested in *non-Brownian* suspensions i.e. $\hat{a} > 1$ μm [37]. The Newtonian carrying fluid in the heavy solution has density, $\hat{\rho}_{f,H}$, and viscosity, $\hat{\mu}_{f,H}$. Similarly, the Newtonian light fluid density and viscosity are denoted by $\hat{\rho}_L$ and $\hat{\mu}_L$

Table 3.1: List of *dimensional* independent input parameters of the lubrication model problem.

Definition	**parameter**
Gravitational acceleration	$\hat{g}$
Half the duct width	$\hat{D}$
Duct length	$\hat{L}$
Particle radius	$\hat{a}$
Particle density	$\hat{\rho}_p$
Carrying fluid density	$\hat{\rho}_{f,H}$
Carrying fluid viscosity	$\hat{\mu}_{f,H}$
Light fluid density	$\hat{\rho}_L$
Light fluid viscosity	$\hat{\mu}_L$
Initial total volume of particles	$\hat{V}_p$
Jamming volume of particles	$\hat{V}_j$

respectively. Both the fluids and solid phases are assumed to be incompressible. The initial total volume of particles is $\hat{V}_p$. At time $\hat{t} = 0$ s, the heavy particle-laden mixture occupies the top half of the duct ($\hat{x} < 0$) whereas the light pure fluid takes the bottom half ($\hat{x} \geq 0$). The jamming volume which depends on the shape and packing arrangement of the particles, is further assigned by $\hat{V}_j$ [32]. Through a dimensional analysis based on Buckingham-π theorem, it is not difficult to show that 8 *dimensionless* parameters control the flow in question, namely the duct aspect ratio, $\delta = \hat{D}/\hat{L} \ll 1$, particle-radius-to-half-the-duct-width, $r_p = \hat{a}/\hat{D}$, particle-to-carrying-fluid density ratio, $\xi = \hat{\rho}_p/\hat{\rho}_{f,H}$, light-to-carrying-fluid density ratio, $\eta = \hat{\rho}_L/\hat{\rho}_{f,H}$, light-to-carrying-fluid viscosity ratio, $\kappa = \hat{\mu}_L/\hat{\mu}_{f,H}$, initial volume fraction of particles, $\phi_0 = \hat{V}_p/\hat{V}_H$, jamming volume fraction, $\phi_j = \hat{V}_j/\hat{V}_H$, and the Reynolds number, $Re = \hat{\rho}_H\left(\phi_0\right)\hat{V}_t(2\hat{D})/\hat{\mu}_H\left(\phi_0\right)$. Similar to the approach of [31], we assume that the volume fraction of particles across the depth of the suspension layer, y, is uniform i.e. $\phi = \phi(x,t)$ only. See Ref. [55] for particle heterogeneity effects in sedimentary flows and Appendix B for negligibility of shear-induced migration effects. Assuming that the duct has unit depth, the total volume of the heavy solution is found as $\hat{V}_H = \hat{D}\hat{L}$. Further assuming monodisperse spherical particles, jamming volume frac-

Table 3.2: List of *dimensionless* independent input parameters of the lubrication model problem.

Definition	parameter
Aspect ratio	$\delta = \frac{\hat{D}}{\hat{L}} \ll 1$
particle-radius-to-half-the-duct-width ratio	$r_p = \frac{\hat{a}}{\hat{D}} \ll 1$
Particle-to-carrying-fluid density ratio	$\xi = \frac{\hat{\rho}_p}{\hat{\rho}_{f,H}} > 1$
Light-to-carrying-fluid density ratio	$\eta = \frac{\hat{\rho}_L}{\hat{\rho}_{f,H}} > 1$
Light-to-carrying-fluid viscosity ratio	$\kappa = \frac{\hat{\mu}_L}{\hat{\mu}_{f,H}} \in [0.1, 10]$
Initial volume fraction of particles	$\phi_0 = \frac{\hat{V}_p}{\hat{V}_H} < \phi_j$
Jamming volume fraction of particles	$\phi_j = \frac{\hat{V}_j}{\hat{V}_H} \approx 0.67$
Reynolds number	$Re = \frac{\hat{\rho}_H(\phi_0)\hat{V}_t(2\hat{D})}{\hat{\mu}_H(\phi_0)} \sim O(1)$

tion is obtained as $\phi_j \approx 0.67$ [31]. The expressions $\hat{\rho}_H\left(\phi_0\right) = \left(\hat{\rho}_p\phi_0 + \hat{\rho}_{f,H}\left(1-\phi_0\right)\right)$ and $\hat{\mu}_H\left(\phi_0\right) = \hat{\mu}_{f,H}\left(1-\phi_0/\phi_j\right)^{-2}$ determine the density and viscosity of heavy fluid respectively [32]. The characteristic velocity in the Reynolds number expression is defined as $\hat{V}_t = \sqrt{\left(1-\psi\right)\hat{g}\hat{D}/\left(1+\psi\right)}$ where $\psi = \hat{\rho}_L/\hat{\rho}_H(\phi_0) = \eta/\left(1+(\xi-1)\phi_0\right)$ is the density ratio of the light fluid to heavy suspension. In our simulations, η can be larger than 1 i.e. light fluid heavier than the carrying fluid. However, ψ is always less than one meaning that the overall suspension mixture is heavier than the light fluid. The dimensional parameters governing the flow along with the dimensionless numbers and their ranges are listed in Tables 3.1 and 3.2.

3.2 Lubrication model derivation

We aim to construct a lubrication model in simplified vertical 2D channel geometry shown schematically in figure 3.1. Due to symmetry, only half of the duct domain between the left wall ($y = 0$) and center ($y = 1$) is considered in the model. Extending the model to a pipe geometry, potentially more convenient for experimentation, is performed in Appendix C. As discussed in depth in Appendix B, for the Boussinesq limit considered ($At \ll 1$ where $At = (\hat{\rho}_H(\phi_0) - \hat{\rho}_L)/(\hat{\rho}_H(\phi_0) + \hat{\rho}_L) = (1-\psi)/(1+\psi)$ is the Atwood number), we may neglect the diffusive effects associated with shear-

induced migration of particles [31, 56, 57]. A lubrication model describing viscous exchange flow of pure fluids has been developed in our recent work [58] for which the configuration was considered to be *slumping* i.e. no-slip condition at both $y = 0$ and 1. Here, we adopt a *symmetric* configuration i.e. no-slip condition at $y = 0$ and stress-free condition at $y = 1$. Following the approach of [58] the governing streamwise and depthwise momentum equations in the heavy particle-laden layer reduce to

$$0 = -p_x + \frac{\rho_H(\phi)Re}{1-\psi} + \mu_H(\phi)u_{yy}, \tag{3.1}$$

$$0 = -p_y, \tag{3.2}$$

where we have scaled the streamwise and depthwise distances by $\hat{D}/\delta$ and $\hat{D}$ respectively. Moreover, the pressure has been scaled by $\hat{\mu}_H(\phi_0)\hat{V}_t/(\delta\hat{D})$. The dimensionless density and viscosity of the heavy layer in the continuum form and as a function of the particles volume fraction, ϕ, are expressed below [31]

$$\rho_H\left(\phi\right) = \frac{1+(\xi-1)\phi}{1+(\xi-1)\phi_0}, \tag{3.3}$$

$$\mu_H\left(\phi\right) = \frac{\left(1-\phi/\phi_j\right)^{-2}}{\left(1-\phi_0/\phi_j\right)^{-2}}. \tag{3.4}$$

Similarly, for the light fluid layer we obtain

$$0 = -p_x + \frac{\psi Re}{1-\psi} + mu_{yy}, \tag{3.5}$$

$$0 = -p_y, \tag{3.6}$$

where $m = \hat{\mu}_L/\hat{\mu}_H(\phi_0) = \kappa\left(1-\phi_0/\phi_j\right)^2$ is the viscosity ratio of the light fluid to that of the heavy suspension layer. Integrating (3.2) and (3.6) across the width gives

$$p = p_0(x,t) + \frac{\rho_H(\phi)xRe}{1-\psi}, \qquad 0 \le y \le 1, \tag{3.7}$$

where we define $p_0(x,t)$ as

$$p_0(x,t) = p(x,0,t) - \frac{\rho_H(\phi)xRe}{1-\psi}. \tag{3.8}$$

In obtaining (3.7), we neglected the effects of an interfacial tension between the two mixtures for simplicity. In other words, we consider an immiscible interface but with zero interfacial tension. Such limit is indeed equivalent to a miscible interface with zero molecular diffusion; see [20, 54, 59] for studies taking similar approach for pure fluids.

The pressure expression (3.7) is now used in the streamwise momentum equations (3.1) and (3.5) to give

$$0 = -P_{0,x} + \mu_H(\phi)u_{yy}, \qquad 0 \le y \le h, \tag{3.9}$$

$$0 = -P_{0,x} - \frac{\rho_H(\phi)-\psi}{1-\psi}Re + mu_{yy}, \qquad h \le y \le 1. \tag{3.10}$$

Note that for simplification, we have defined $P_{0,x} = p_{0,x} + (x\rho_{H,\phi}\phi_x Re)/(1-\psi)$. Applying appropriate boundary and interfacial conditions in (3.11)-(3.13), the equations (3.9) and (3.10) can be integrated with respect to y in order to determine the streamwise velocity closures in each layer. In the case of miscible fluids, standard no-slip condition at the lower wall ($y = 0$) may be used. However, in the case of immiscible fluids, we face the well-known *contact-line* problem due to the singularity of the stress at the walls. Many authors have worked intensely for decades to address this issue suggesting a wide range of remedies e.g. replacing no-slip conditions at the

wall by *Navier-slip* ones [60] assuming a narrow *precursor* film of thickness b in the vicinity of the wall as laid out by [61]. Similar to study of [31], we are interested in a scenario where the suspension mixture flows close to the surface of the duct wall. The precursor film approach then suits our application the best. In fact, the validity of such assumption for particle-laden flows has been confirmed in the experiments of [30]. Due to the symmetry, we can further apply the stress-free condition in the duct center ($y = 1$). In summary

$$u = 0, \quad at\ y = 0, \tag{3.11}$$

$$u_y = 0, \quad at\ y = 1. \tag{3.12}$$

The homogeneity of the velocity and stress at the interface, h, requires

$$[u] = 0, \ \left[\tau_{xy}\right] = 0, \quad at\ y = h, \tag{3.13}$$

where [ ] denotes the jump of the given quantity. Note that in (3.13), $\tau_{xy} = u_y$ for the heavy and $\tau_{xy} = mu_y$ for the light fluids respectively. The last condition needed to solve the system of equations (3.9) and (3.10) for the velocity closures is the total flow constraint

$$\int_0^1 u dy = 0. \tag{3.14}$$

The streamwise velocity, u, in the heavy and light layers can then be obtained by integrating (3.9) and (3.10) twice as

$$u = \frac{P_{0,x} y^2}{2\mu_H} + c_1 y + c_2, \quad 0 \le y \le h, \tag{3.15}$$

$$u = \left(P_{0,x} + \frac{\rho_H - \psi}{1 - \psi} Re\right) \frac{y^2}{2m} + d_1 y + d_2, \quad h \le y \le 1, \tag{3.16}$$

where $P_{0,x}$, c_1, c_2, d_1, and d_2 are coefficients given in Appendix D. The flux function,

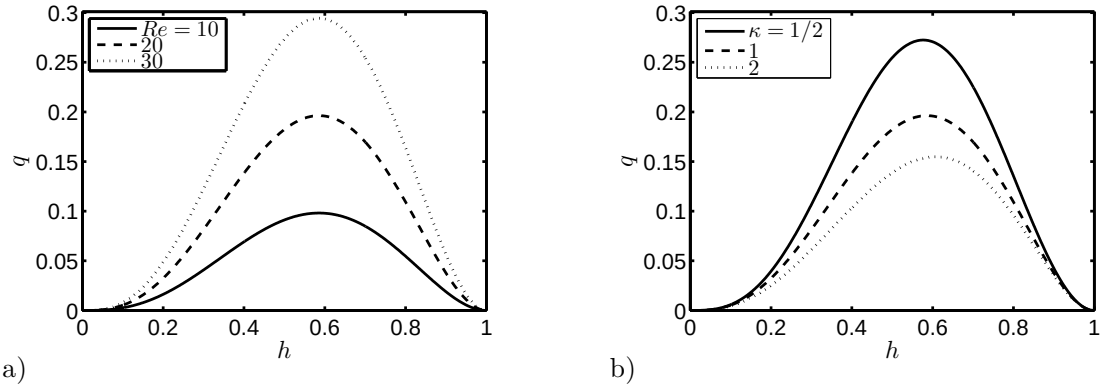

a) b)

Figure 3.2: Variation of the flux function, q, in (3.17) with interface height, h, for pure fluids ($\phi_0 = r_p = \xi = 0$) and a) $\kappa = 1$ at various values of Re, b) $Re = 20$ at various values of κ.

$q = \hat{q}/\hat{D}$, as the flow rate within the heavy layer can eventually be calculated as

$$q = \int_0^h u dy, \tag{3.17}$$

which is given in Appendix E as function of h, Re, m, μ_H, and ρ_H. In the case of pure fluids ($\phi_0 = 0$), we obtain $\rho_H = \mu_H = 1$ from (3.3) and (3.4). Relevant dimensionless numbers governing the flow would then be reduced to Re and κ. Note that since $\rho_H = 1$ in (3.16) the model becomes immaterial of ψ (thus η). Figures 3.2a and b show the variation of q versus h for different values of Re and κ respectively. As $h \to 0$ and 1, $q \to 0$. The flux function, q exhibits a maximum in the interval $h \in [0,1]$. The location of this maximum remains unchanged in the iso-viscous case, $h \approx 0.586$; see figure 3.2a. However, the maximal q location slightly shifts to the left (smaller h) with decreasing the viscosity ratio, κ, i.e. less-viscous light fluid, as shown in figure 3.2b.

The evolution equations for the interface height and particle volume fraction respectively read; see appendix F for derivation and also Ref. [31] for similar formula-

tion derived for particle-laden film flow over an inclined surface,

$$h_t + q_x = 0, \tag{3.18}$$

$$(\phi h)_t + (u_p \phi h)_x = 0, \tag{3.19}$$

where u_p is the particle velocity expressed as $u_p = q/h + u_s(1-\phi)$. Here, $u_s = f(\phi)w(h)u_0$ is the dimensionless hindered Stokes velocity with $u_0 = 2\hat{a}^2\left(\hat{\rho}_p - \hat{\rho}_{f,H}\right)\hat{g}/(9\hat{V}_t\hat{\mu}_{f,H})$ - or $u_0 = (\xi-1)\psi\kappa\mathrm{Re}\left(1+\psi\right)r_p^2/(9m\eta\left(1-\psi\right))$ - being the dimensionless Stokes velocity of a single particle [32]. Moreover, $f(\phi) = (1-\phi)^5$ is Richardson-Zaki settling function [43] and $w(h)$ is the wall function chosen as $w(h) = h^2$ to give 0 and 1 at the wall ($y = 0$) and center ($y = 1$) respectively; see also Ref. [31] for other forms of the wall function. In (3.18) and (3.19), time is naturally scaled by $\hat{D}/(\delta\hat{V}_t)$. In order to advantageously solve the system of equations (3.18) and (3.19) in a conservative framework, we define an additional parameter θ as

$$\theta = \phi h. \tag{3.20}$$

Using (3.20), (3.18) and (3.19) will result in the following set of equations, simply in the form of classical Riemann problem

$$h_t + F_x(h,\theta) = 0, \tag{3.21}$$

$$\theta_t + G_x(h,\theta) = 0, \tag{3.22}$$

where

$$F(h,\theta) = q(h,\theta), \tag{3.23}$$

$$G(h,\theta) = \frac{\theta F(h,\theta)}{h} + u_0\theta\left(1-\frac{\theta}{h}\right)f\left(\frac{\theta}{h}\right)w(h). \tag{3.24}$$

The kinematic conditions (3.21) and (3.22) along with flux condition (3.14) ensure conservation of pure fluids as well as total mass of particles (and thus volume and area due to the presumed incompressibility) at all times.

3.3 Numerical scheme

3.3.1 Procedure

Our methodology to numerically solve the system of Partial Differential Equations (PDE) of (3.21) and (3.22) in space, x, and time, t, is based on the robust explicit high-resolution Total Variation Diminishing (TVD) finite difference scheme of [62]. We first define

$$\vec{u} = \begin{bmatrix} h \\ \theta \end{bmatrix}, \vec{f} = \begin{bmatrix} F \\ G \end{bmatrix} \tag{3.25}$$

Discretizing (3.21) and (3.22) using finite difference method gives

$$\frac{\vec{u}_j^{n+1} - \vec{u}_j^n}{\Delta t} + \frac{1}{\Delta x}\left[\vec{f}^n_{j+\frac{1}{2}} - \vec{f}^n_{j-\frac{1}{2}}\right] = 0. \tag{3.26}$$

The flux vector, $\vec{f}$, in (3.26) is expressed as

$$\vec{f}^n_{j\pm\frac{1}{2}} = \frac{1}{2}\left\{\left[\vec{f}\left(\vec{u}^{R,n}_{j\pm\frac{1}{2}}\right) + \vec{f}\left(\vec{u}^{L,n}_{j\pm\frac{1}{2}}\right)\right] - a^n_{j\pm\frac{1}{2}}\left[\vec{u}^{R,n}_{j\pm\frac{1}{2}} - \vec{u}^{L,n}_{j\pm\frac{1}{2}}\right]\right\}. \tag{3.27}$$

Here,

$$\begin{aligned} \vec{u}^{R,n}_{j+\frac{1}{2}} &= \vec{u}^n_{j+1} - \frac{\Delta x}{2}\left(\vec{u}^n_x\right)_{j+1}, & \vec{u}^{L,n}_{j+\frac{1}{2}} &= \vec{u}^n_j + \frac{\Delta x}{2}\left(\vec{u}^n_x\right)_j, \\ \vec{u}^{R,n}_{j-\frac{1}{2}} &= \vec{u}^n_j - \frac{\Delta x}{2}\left(\vec{u}^n_x\right)_j, & \vec{u}^{L,n}_{j-\frac{1}{2}} &= \vec{u}^n_{j-1} + \frac{\Delta x}{2}\left(\vec{u}^n_x\right)_{j-1}, \end{aligned} \tag{3.28}$$

with $(\vec{u}_x^n)_k$ being a flux limiter chosen to be in the $minmod$ class of the following form

$$\left(\vec{u}_x^n\right)_k = minmod\left(\frac{\vec{u}_k^n - \vec{u}_{k-1}^n}{\Delta x}, \frac{\vec{u}_{k+1}^n - \vec{u}_k^n}{\Delta x}\right). \tag{3.29}$$

The function $minmod$ is defined as

$$minmod(a,b) = \frac{1}{2}[\mathrm{sgn}(a) + \mathrm{sgn}(b)].\min(|a|,|b|). \tag{3.30}$$

Also note that

$$a_{j\pm\frac{1}{2}}^n = \max\left[\rho\left(\frac{\partial \vec{f}}{\partial \vec{u}}\right)_{\vec{u}_{j\pm\frac{1}{2}}^{R,n}}, \rho\left(\frac{\partial \vec{f}}{\partial \vec{u}}\right)_{\vec{u}_{j\pm\frac{1}{2}}^{L,n}}\right], \tag{3.31}$$

gives the local propagation speed of the interfacial wave. Here,

$$\rho(A) = max(|\lambda_1|, |\lambda_2|), \tag{3.32}$$

is the spectral radius of matrix A with λ_1 and λ_2 being its eigenvalues. The stable time step, dt, is calculated using a Courant-Friedrichs-Lewy (CFL) condition as

$$dt = \frac{CFL.dx}{\max(|a(t)|)}. \tag{3.33}$$

For our simulations, we have found that $CFL \approx 0.1$ leads to stable results. Once h and θ are computed, particle volume fraction can be simply obtained from $\phi = \theta/h$. The numerical examples shown in this thesis are attained using the computational resources in Center for Advanced Computing & Data Systems of University of Houston (Maxwell cluster). While the run time on a parallelized code on such a cluster (4 nodes) for pure fluids can be very quick (order of minutes), due to the extremely small mesh size required in the particle-laden case, it can take up to 4 days for the simulations to complete. We will discuss this in more details in section 3.4.2.

3.3.2 Benchmarking notes

In order to ensure the validity of our model and numerical scheme, the following steps were taken (results are not presented here for brevity): **1)** Figures 6.23-27 and 6.32 in [62], obtained from solving similar nonlinear conservation equations to (3.21) and (3.22), were successfully recovered using our code. **2)** Adopting the flux function expression given in Appendix B of [58], we benchmarked their results of exchange flow of pure immiscible fluids in a duct. **3)** In the case of particle-laden film flow over a flat free surface studied by [31], the flux function, q, is shown to simply reduce to $q = \rho_H h^3/\mu_H$; compare with q expression given in our Appendix E. Using this flux function and our numerical scheme, we fully restored figures 4.3 and 4.4 in [31], where they depict particle enrichment and depletion effects in the vicinity of the advancing suspension front. We will discuss this issue in detail in section 3.4.2.

3.4 Results

3.4.1 Pure fluids ($\phi_0 = 0$)

While the slumping exchange flow of two fluids in a duct has been investigated extensively in the literature [19, 58, 63, 64] the symmetric configuration, to the best of our knowledge, has not been studied even for pure fluids. Therefore, we find it important to address such limit first before moving on to a more complicated particle-laden flow. In the absence of an interfacial tension between the two fluids, the thickness of the precursor film can be chosen as zero ($b = 0$) without any contact-line singularity issue [19, 58]. Figure 3.3a shows the evolution of the interface height with time assuming two iso-viscous fluids ($\kappa = 1$) at $Re = 20$. (Other parameters used are $\phi_0 = r_p = \xi = 0$.) The initial condition is such that the interface height is $h = 1$ and 0 over $x < 0$ and $x \geq dx$ respectively, i.e. the heavy (light) mixture occupying left (right) side of the duct. It has been confirmed that the computed solution is not sensitive to the choice of initial condition (results not presented here for brevity). The mesh

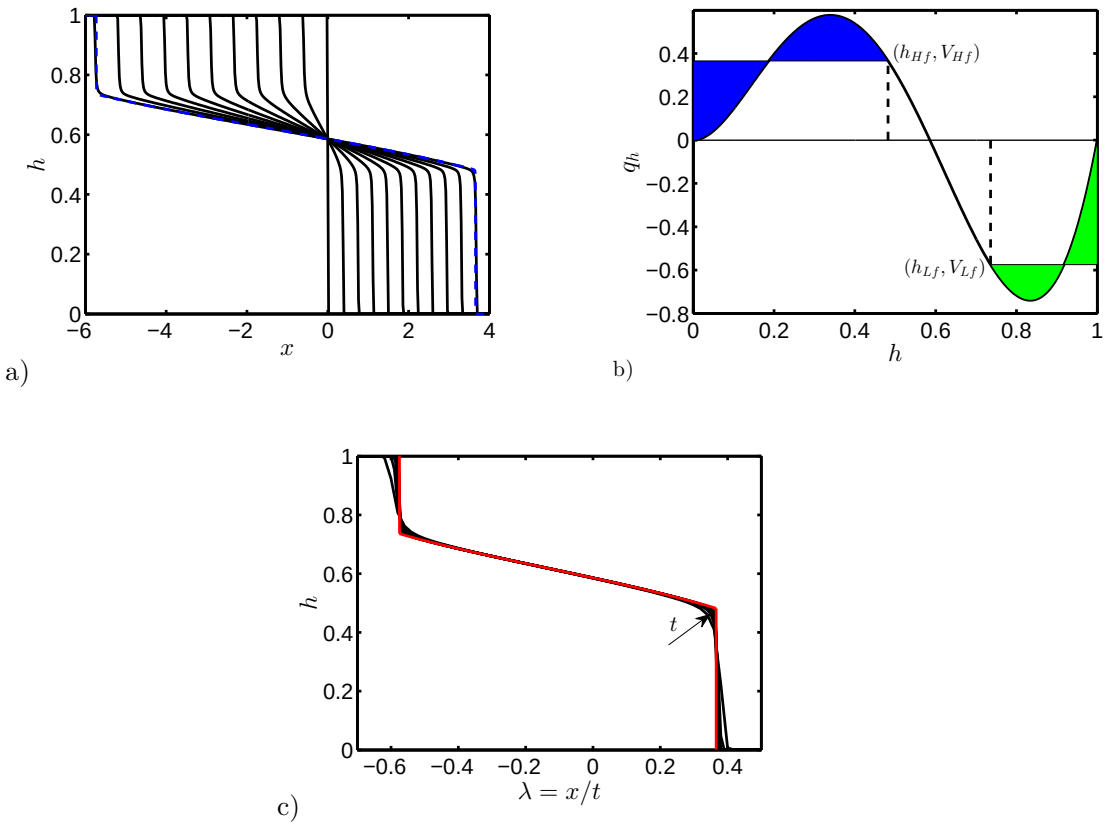

Figure 3.3: a) Evolution of the interface height, h, with time, $t = [0,1,2,...,10]$, of two iso-viscous fluids. b) Dependency of the derivative of the flux function, q_h, on h. c) Collapse of the h profiles using similarity parameter, $\lambda = x/t$.

size chosen to produce figure 3.3a and all other pure fluid examples is $dx = 0.02$. The results for $dx = 0.002$ (blue dashed line) are almost indistinguishable from those of $dx = 0.02$ as illustrated in figure 3.3a. Due to the symmetric duct flow configuration, the light layer in the center of the duct has to advance faster than the heavy one to conserve mass.

The interface profiles shown in figure 3.3a suggest a rather *self-similar* pattern in the form of steady traveling waves. Using a similarity parameter, $\lambda = x/t$, equation (3.18) can be re-written as

$$-\frac{\lambda h_\lambda}{t} + \frac{q_\lambda}{t} = 0. \tag{3.34}$$

Alternatively, the following condition can be derived

$$\lambda = q_h, \tag{3.35}$$

which, via q expression given in Appendix E, relates λ to h, Re and κ. For the example shown in figure 3.3a ($\phi_0 = 0$, $Re = 20$, $\kappa = 1$), we may obtain the following

$$\lambda = -10(h^3 - 5h^2 + 6h - 2)h^2, \tag{3.36}$$

Equation (3.36) clearly has an analytical expression for h as function of λ. However, it can be checked this solution does not satisfy the total flow rate constraint (3.14) over the whole range of λ [58]. Reference [65] showed that a compound wave solution may instead be put forth comprising heavy and light layers front heights, h_{Hf} and h_{Lf}, located at λ_{Hf} and λ_{Lf} respectively; and a stretching region in between ($\lambda_{Lf} < \lambda < \lambda_{Hf}$). Following the approach of [19], the front heights, h_{Hf} and h_{Lf}, and speeds, $\lambda_{Hf}(= V_{Hf})$ and $\lambda_{Lf}(= V_{Lf})$, are determined from the *equal-area* rule

$$q(h_{Hf}) = h_{Hf} q_h(h_{Hf}), \tag{3.37}$$

$$-q(h_{Lf}) = (1 - h_{Lf}) q_h(h_{Lf}). \tag{3.38}$$

Figure 3.3b depicts the implementation of the equal-area rule for the example shown in figure 3.3a. It is found that $h_{Hf} \approx 0.482$, $h_{Lf} \approx 0.736$, $V_{Hf} \approx 0.366$ and $V_{Lf} \approx -0.575$. The compound similarity solution for the flow shown in figure 3.3a is finally obtained as

$$h = \begin{cases} 1, & \lambda < -0.575, \\ -10\left(h^3 - 5h^2 + 6h - 2\right)h^2, & -0.575 \le \lambda \le 0.366, \\ 0, & \lambda > 0.366, \end{cases} \tag{3.39}$$

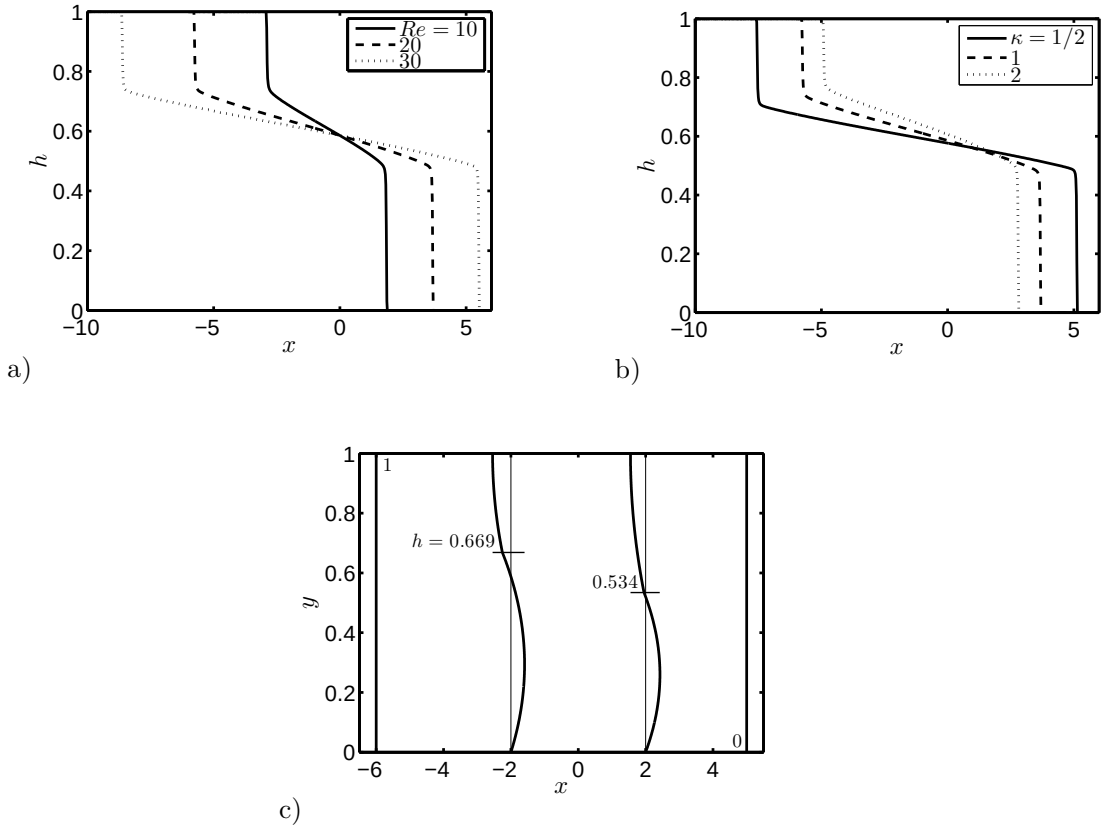

Figure 3.4: Comparison of the interface height, h, at $t = 10$ for a) $\kappa = 1$ at different values of Re, and b) $Re = 20$, at different values of κ. c) Streamwise velocity profile, u.

The analytical solution (3.39) and computed interface profiles at long time are shown in figure 3.3c. The *long-time* behavior is defined where there are no noticeable changes of the interface height behavior with time, t. For instance, in figure3.3a, it can be seen that as time progresses, the interface height front approaches the value of 0.482 i.e. the layers steadily interpenetrate into one another within a traceable path. Very close agreement found between the analytical solution (3.39) and computation in figure 3.3c verifies the effectiveness of the similarity-solution approach.

Figure 3.4a compares the interface profiles at long time ($t = 10$) for $\kappa = 1$ and different values of Re. (Other parameters used are $\phi_0 = r_p = \xi = 0$.) As observed, the interpenetration of the heavy and light layers is enhanced with Re. Larger Re can be interpreted as higher density difference between the two fluids which acts to in-

tensify the exchange flow. Although the frontal speeds change with Re, the front heights remain unaffected. The effect of a viscosity contrast between the two fluids, κ, is shown in figure 3.4b. It is evident that at lower κ values (less-viscous light fluid), the degree of interpenetration of the layers is higher which is in agreement with the findings of [19, 64] for slumping flows. Keeping $Re = \hat{\rho}_H(\phi_0)\hat{V}_t(2\hat{D})/\hat{\mu}_H(\phi_0)$ constant with more-viscous heavy fluid (low κ) requires larger $\hat{V}_t$ or driving buoyancy force which acts to expand the extent of the exchange zone (figure 3.4b). Unlike figure 3.4a shown for different values of Re, the front height does change with κ. It is insightful at this stage to look into the streamwise velocity profiles of a typical simulation. Figure 3.4c shows computed velocity profiles using (3.15) and (3.16) at different locations, $x = -6, -2, 2, 5$, for $\kappa = 2$ case in figure 3.4b. The calculated interface heights at the given x locations are respectively, $h = 1, 0.669, 0.534, 0$. The velocity profile is perfectly zero at duct cross sections that are full of heavy ($h = 1$) and light ($h = 0$) layers. The validity of the no-slip and no-stress conditions (3.11) and (3.12) at the wall ($y = 0$) and the duct center ($y = 1$) respectively is apparent. Since $\kappa = 2$ corresponds to a less-viscous heavy fluid, we note a slightly larger gradient of velocity within this layer ($h = 0.669$ and 0.534 cases in figure 3.4c) which ensures homogeneity of shear stress across the interface; see condition (3.13).

The variation of the height and speed of heavy and light fronts at long time with κ and Re is shown in figure 3.5 using the equal-area rule. Figures 3.5a and b demonstrate the variation of h_{Hf} and h_{Lf} respectively over a wide range of κ. As predicted in figure 3.4a, the heights of heavy and light fronts will not change with the Reynolds number. Therefore, the curves for all values of Re overlay in figures 3.5a and b. h_{Hf} reaches a minimum at $\kappa \approx 0.8$, while the minimum h_{LF} appears at a smaller viscosity contrast ($\kappa \approx 0.2$). Although h_{Hf} and h_{Lf} change non-monotonically with viscosity ratio, the variation of V_{Hf} and V_{Lf} with κ is monotonic as shown in figures 3.5c and d. Also note that unlike the frontal height, the frontal speeds clearly depend on Re

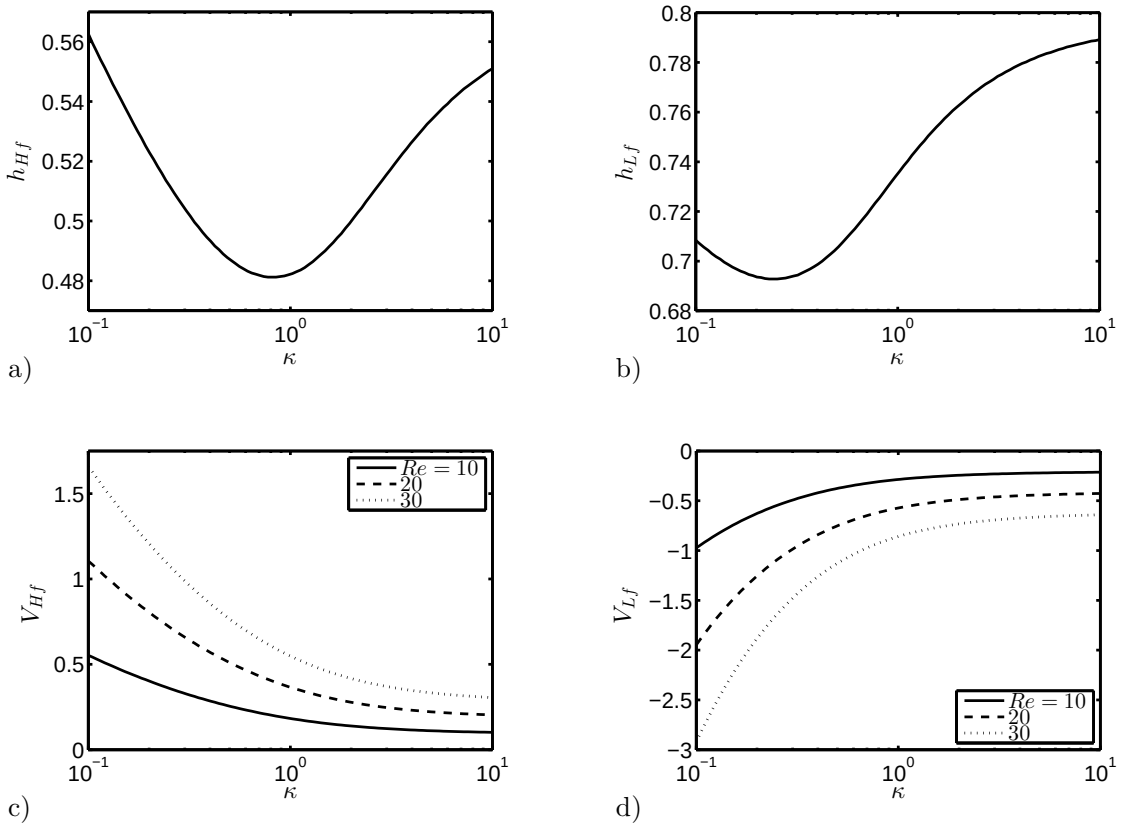

Figure 3.5: Variation of a) heavy front height, h_{Hf}, and b) light front height, h_{Lf}, , and their frontal velocities (c) V_{Hf}, and (d) V_{Lf}, versus κ and Re for $\phi_0 = r_p = \xi = 0$.

(speeds increasing with Re). Absolute values of V_{Hf} and V_{Lf} decrease with an increase in κ as also revealed in figure 3.4b.

3.4.2 Particle-laden flows ($\phi_0 > 0$)

We now examine particle-laden flows. Solving the governing system of PDEs (3.18) and (3.19) numerically when $\phi_0 \neq 0$, is more challenging since an extremely small mesh size ($dx \approx 2 \times 10^{-7}$) is required to fully capture the underlying effects of the flow [31]. Figure 3.6a shows the evolution of the interface height profile, h, at times $t = [0, 0.01, 0.02, ..., 0.1]$ for $\phi_0 = 0.3$, $Re = 0.1$, and $\kappa = 1$. The other parameters are chosen closely to those in the experiments of [30] ($r_p = 0.06$, $\xi = 1.9$, and $\eta = 1.25$). The particle volume fraction value mostly chosen in our study ($\phi_0 = 0.3$) is selected such that a comparison with results of [30] and [31] can be made feasible. Understanding the suspension behavior in dense granular limit ($\phi_0 \rightarrow \phi_j$) [66] requires further studying which is outside the scope of current thesis. Note that the viscosity function (3.4) becomes singular as $\phi_0 \rightarrow \phi_j$. In the case of particle-laden flows, a zero precursor film thickness introduces a singularity into the solution as laid out by [31]. To overcome such a singularity, we have used a small value of $b = 0.01$ in the thesis unless otherwise stated; see also experiments of [30] and computations of [31]. The small choice of $t = 0.1$ for the case of figure 3.6 is due to the limited access to computational resources for carrying out these simulations. Nevertheless, even this small interval is enough to extrapolate the long time behavior of the flow, thanks to the self-similarity characteristic of the solutions. The top insets in figures 3.6a and b show the collapse of profiles using $\lambda = x/t$ with a small residual dependence on time which is comparable to that found by [19] and [58] for displacement flows. Due to the complex interface shape, Rankine-Hugoniot similarity conditions of [30] may not be directly applied to the particle-laden exchange flows in confined geometry. Computed solution mesh independence is successfully confirmed in figure 3.6a for two different values of dx. The blue dashed line in (a) shows the solution at $t = 0.1$ for $dx = 2 \times 10^{-6}$

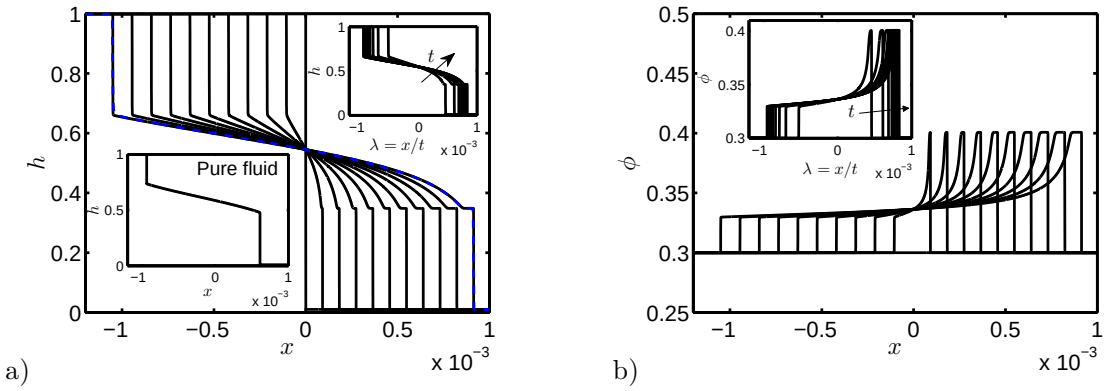

Figure 3.6: Evolution of the a) interface height, h, and b) particle volume fraction, ϕ, profiles with time, $t = [0, 0.01, 0.02, ..., 0.1]$.

which is almost indistinguishable from that of $dx = 2 \times 10^{-7}$.

In order to fully understand the effect of particle addition to exchange flows, we have added interface height profiles corresponding to the pure fluids as inset to the particle-laden figure results; see figures 3.6-3.13. The Reynolds number, Re, and mixtures viscosity ratio, $m = m(\phi_0, \kappa)$ are kept the same in associated pure-fluid and particle-laden cases. Upon comparing figure 3.6a to pure fluid results shown in the lower left inset, two important conclusions may be drawn: 1) The interface height profile in the presence of solid particles exhibits a plateau in the vicinity of the heavy layer front ($h \approx 0.348$ and $\phi \approx 0.400$ as steady long-time behavior). Such plateau is reminiscent to the capillary ridge in simulations of [58] but is formed under a completely different mechanism namely the presence of solid particles. 2) The stretched interface between the heavy and light fronts also is more curved in the particle-laden case compared to the pure fluid. In order to understand these differences we need to look at the volume fraction profiles, ϕ, as shown in figure 3.6b. As it is interestingly evident, there are jumps in ϕ along the duct length, x. Particularly, there is an increase in ϕ close to the light layer's front followed by a stronger jump in the vicinity of the heavy layer's front. This pattern is different than that reported experimentally and theoretically by [30] for free-surface film flows. Due to the lock exchange config-

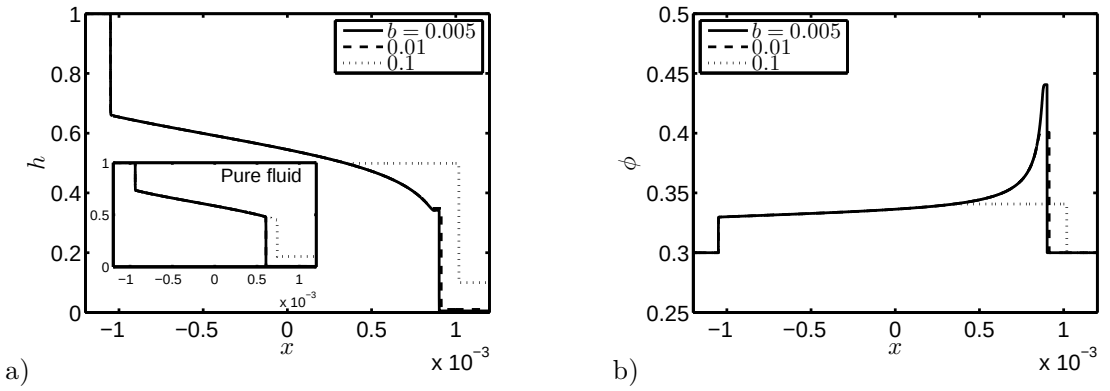

Figure 3.7: Change in a) interface height, h, and b) particle volume fraction, ϕ, with x at $t = 0.1$ and various values of the precursor film thickness, b.

uration and geometry confinement we witness a two-step increase in ϕ close to the heavy and light layers instead of the one observed in the vicinity of the heavy front in the case of [30]. The curvature of the interface height in particle-laden case is then justified by the fact that the viscosity of the heavy solution is continuously changing alongside streamwise direction through ϕ in (3.4), in turn modifying the dynamics of the exchange flow (see also figure 3.4b).

It has been hypothesized by [30] that the accumulation of particles close to the frontal region of the flow (e.g. in figure 3.6b) is due to the different transport rates of fluid and solid shown mathematically in (3.23) and (3.24). See also Ref. [67] for similar shock formation effects in sedimentation problems. One question that might arise here is whether particle accumulation at the front can grow to an extent that causes *pinch-off*. In fact, by closely looking into the experiments of [30, 56, 68–73] for particle-laden film flow down an incline, there is no evidence that such accumulation may lead to pinch-off. Also note that our computational code fails when particle enrichment approaches the jamming limit ($\mu \to \infty$ as $\phi \to \phi_j$). The lubrication model assumption will also not be valid close to this limit. As can be seen, in all presented simulations, the computed ϕ values are well below this jamming limit. Due to settling Stokes velocity of particles (negative buoyancy), the particles accumulate close

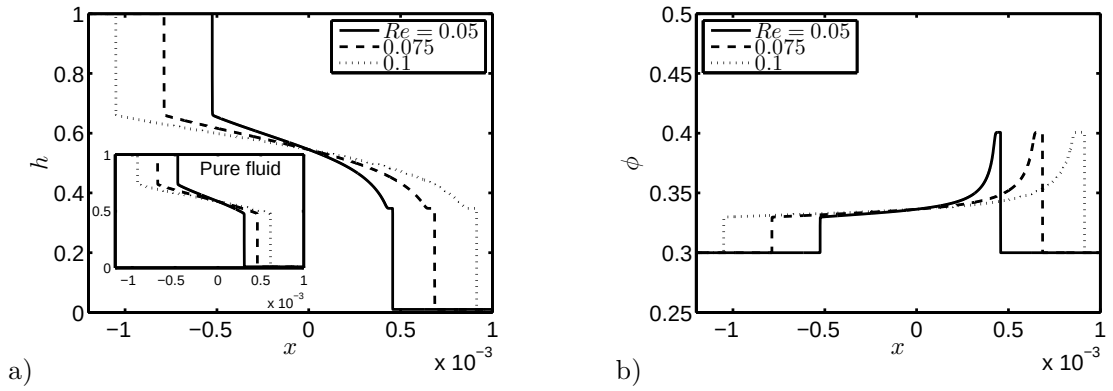

Figure 3.8: Change in a) interface height, h, and b) particle volume fraction, ϕ, with x at $t = 0.1$ and various values of the Reynolds number, Re.

to the front. However, this accumulation does not grow unboundedly because at the same time the properties of the mixture such as density (3.3) and viscosity (3.4) are also changing as a result of enrichment, eventually taking the frontal flow dynamics to a balanced state.

The effect of the precursor film thickness, b, is investigated in figure 3.7, keeping the rest of the controlling parameters the same as in figure 3.6 ($\phi_0 = 0.3$, $Re = 0.1$, $\kappa = 1$, $r_p = 0.06$, $\xi = 1.9$, and $\eta = 1.25$). Figure 3.7a shows that even though the shape of light layer's front remains unchanged, the one for the heavy layer is significantly affected by b; also compare against the inset representing pure-fluid case. The height of the heavy layer's front and its extent increase with b. An increase in the frontal height is accompanied by a decrease in the level of particle enrichment as evident in figure 3.7b. For small values of b, particle-rich zone grows to an extent that might cause singularity in the solution ($\mu_H \to \infty$ as $\phi \to \phi_j$). This observation is in complete agreement with the findings of [30, 31] for free-surface film flows. In fact, they mention that this complex frontal shock behavior may not be entirely captured by first order lubrication model. Figures 3.8a and b compare the profiles of the interface height, h, and particle volume fraction, ϕ, respectively, at various values of the Reynolds number, Re. In compliance with our observation in figure 3.8a in-

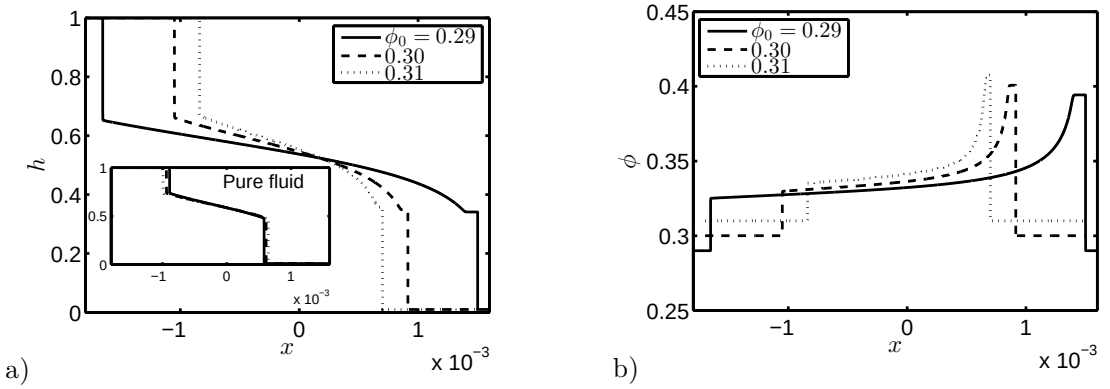

Figure 3.9: Change in a) interface height, h, and b) particle volume fraction, ϕ, with x at $t = 0.1$ and various values of the initial particle volume fraction, ϕ_0.

set for pure fluids, the interpenetration rate of the heavy and light layers similarly increases with Re. Moreover, the heights of the heavy and light fronts remain the same while changing Re. The constancy in advancing front heights is accompanied by uniform increase in volume fraction of particle; see figure 3.8b.

The initial volume fraction of particles, ϕ_0, plays an important role in the dynamics of the flow as it controls both the density (3.3) and viscosity (3.4) of the heavy mixture. Keeping all the other parameters constant, the dependency of the interface height, h, and volume fraction of particles, ϕ, on ϕ_0 is investigated in figures 3.9a and b respectively. The extent of the exchange flow is decreased with ϕ_0 as shown in figure 3.9a. While the density of the heavy mixture, $\hat{\rho}_H$ increases with ϕ_0 (larger driving force), its viscosity, $\hat{\mu}_H$, also increases which results to an overall slowdown of the flow. The frontal heights at the heavy and light layers are shown to minutely increase with ϕ_0. The corresponding profiles to the pure fluid case is shown in inset of figure 3.9a. An increase in ϕ_0 results in a decrease in effective mixtures viscosity ratio, m, which can mildly extend the exchange zone between the two fluids observed from the inset of figure 3.9a; see also figure 3.4b. Particle enrichment close to the heavy and light fronts is consistently observed over a range of ϕ_0 (figure 3.9b). However, the relative rise in particle concentration seems to be slightly less for higher

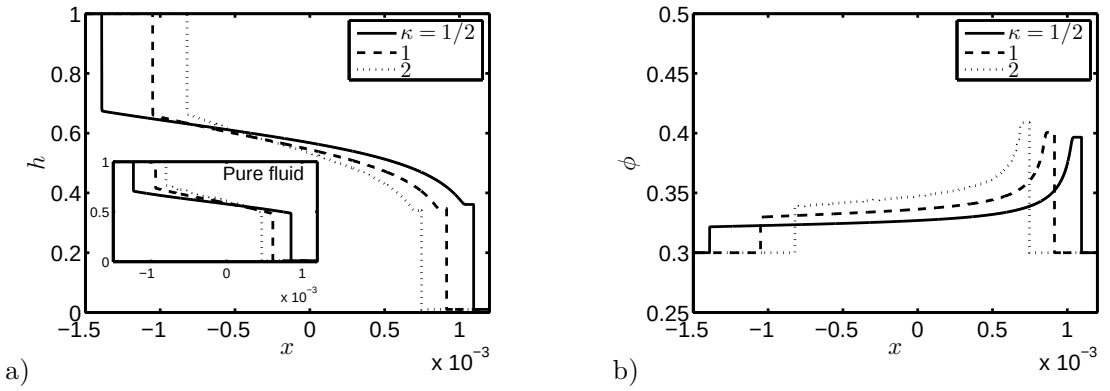

Figure 3.10: Change in a) interface height, h, and b) particle volume fraction, ϕ, with x at $t = 0.1$ and various values of the light-to-carrying-fluid viscosity ratio, κ.

ϕ_0; compare e.g. $\phi_0 = 0.29$ and 0.31 curves in figure 3.9b. The general features of the flow such as interface height curvature as well as particle enrichment close to the heavy front, for other values of ϕ_0, e.g. in the dilute range $\phi_0 = 0.01$ [6], are similar to those obtained for $\phi_0 \approx 0.3$. Results are not presented here for brevity.

The increase in light-to-carrying-fluid viscosity ratio, κ, tends to contract the exchange zone between the two fluids as shown in figure 3.10a. Comparing this to the results for pure exchange flows shown as the inset, we infer that the height of the heavy front in the particle-laden case slightly decreases with κ which is complemented by a growth in the volume fraction of particles, ϕ (figure 3.10b). Note that in the case of free-surface film flow of [30] and [31], an increase/decrease in the frontal height is only achieved by an increase/decrease in local particle volume fraction. However, in a confined geometry, various intricate scenarios might happen at the front, for example, the frontal height might decrease while particle volume fraction increasing (figure 3.10) and vice versa (figure 3.7). Let us physically explain the increase of ϕ with κ observed in figure 3.10b: Large κ corresponds to small $\hat{\mu}_{f,H}$. Considering the definition, the dimensionless Stokes velocity, $u_0 = 2\hat{a}^2\left(\hat{\rho}_p - \hat{\rho}_{f,H}\right)\hat{g}/(9\hat{V}_t\hat{\mu}_{f,H})$, is increased as $\hat{\mu}_{f,H}$ is decreased. Larger u_0 increases particle slip velocity in G flux function (3.24) which will consequently result

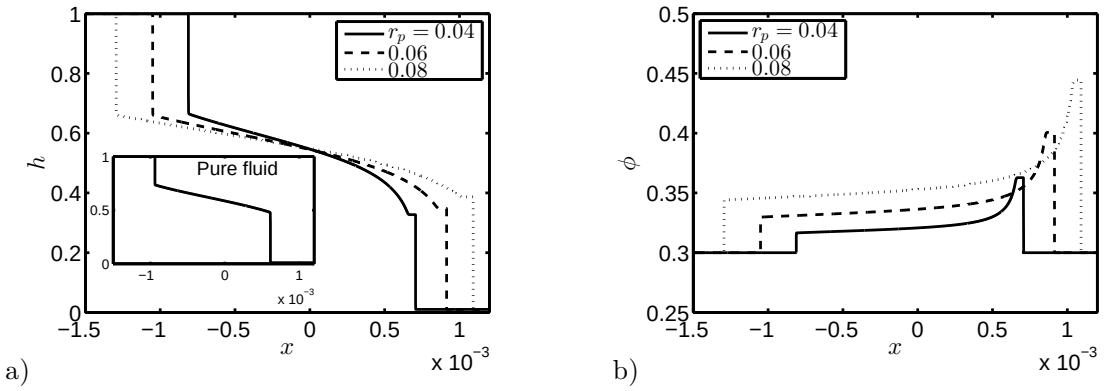

Figure 3.11: Change in a) interface height, h, and b) particle volume fraction, ϕ, with x at $t = 0.1$ and various values of the particle-radius-to-half-the-duct-width ratio, r_p.

in stronger accumulation of particles as shown in figure 3.10b. In the cases of [30] and [31], the dynamics of flow is basically governed by particle settling within a single carrying fluid plus no-stress condition imposed at the free surface. However, in the current channel flow case, not only we have the effect of particles' slip velocity but also the interaction of the carrying and light fluids at the interface captured via the stress homogeneity condition (3.13). Such combination gives rise to complex patterns observed in the channel geometry as opposed to the free-surface one.

Investigating the effect of the relative size of particles, r_p, can provide more insight into the dynamics of the exchange flow in question. Figure 3.11 shows the interface height and particle volume fraction profiles for the same parameters as in figure 3.6 except r_p. An increase in the size of particles consistently increases the height of the heavy front (figure 3.11a) and local volume fraction (figure 3.11b). Note a similar increase in ϕ close to the light fluid front as well as the heavy one. As it is evident in figure 3.11a, the interface between the two fluids has been extended with r_p. Let us have a fundamental look into this effect: The increase in $r_p = \hat{a}/\hat{D}$ can be interpreted as either an increase in particle radius, $\hat{a}$, or a decrease in half of the duct width, $\hat{D}$. If we supposedly consider the latter, then from the Reynolds number expression given in Table 3.2, Re should therefore decrease. Increasing r_p while

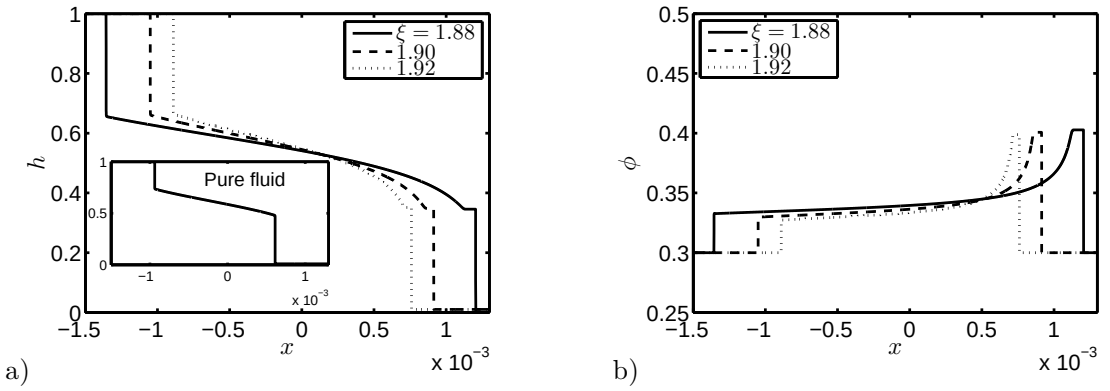

Figure 3.12: Change in a) interface height, h, and b) particle volume fraction, ϕ, with x at $t = 0.1$ and various values of the particle-to-carrying-fluid density ratio, ξ.

keeping Re the same in figure 3.11 requires, for instance, a decrease in the heavy mixture viscosity, $\hat{\mu}_H(\phi_0)$, which is achievable by decreasing the carrying fluid viscosity, $\hat{\mu}_{f,H}$, see section 3.1. In order to keep $\kappa = \hat{\mu}_L/\hat{\mu}_{f,H}$ the same in figure 3.11, $\hat{\mu}_L$ shall also be decreased. A decrease in the carrying and light fluids viscosity, on the other hand, acts to ease the advancement of the exchange flow as confirmed in figure 3.11a. The effect of r_p is also directly reflected in particle's dimensionless Stokes velocity, $u_0 = (\xi - 1)\psi\kappa Re\left(1+\psi\right)r_p^2/(9m\eta\left(1-\psi\right))$, which feeds into the flux function, G in (3.24). An increase in r_p enhances the settling speed of the particles, which in turn, causes accumulation of particles close to the advancing frontal regions.

Another factor that can potentially enhance the Stokes settling velocity of the particles is the particle-to-carrying-fluid density ratio, ξ; see figure 3.12. As opposed to r_p, an increase in ξ reduces the interpenetration rate of the heavy and light layers; see figure 3.12a. At first glance, this effect seems rather counter-intuitive since an increase in ξ indicates heavier particles which should, in turn, increase the buoyant driving force of the flow. However, similar to the rationale presented for figure 3.11, we need to consider the fact that the depicted profiles are obtained for constant Reynolds number, $Re = \hat{\rho}_H\left(\phi_0\right)\hat{V}_t(2\hat{D})/\hat{\mu}_H\left(\phi_0\right)$. From section 3.1, we learnt that Re depends on $\hat{V}_t$ which, by itself, decreases with ψ since $\hat{V}_t = \sqrt{(1-\psi)\hat{g}\hat{D}/(1+\psi)}$.

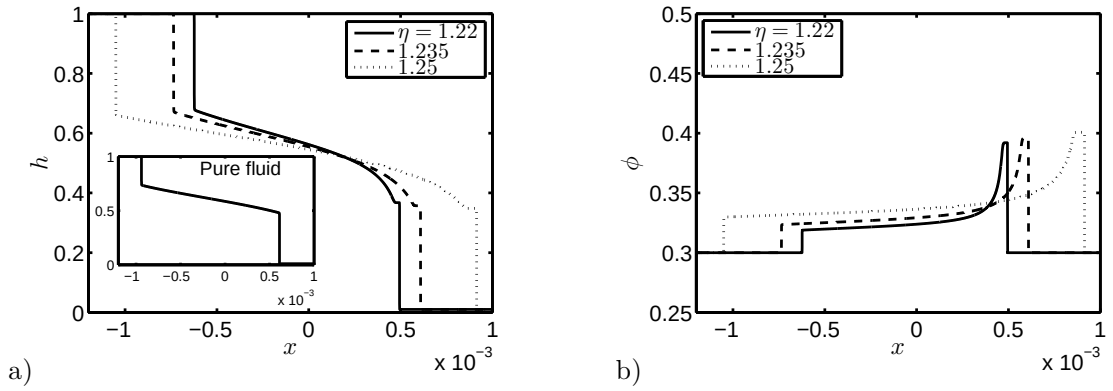

Figure 3.13: Change in a) interface height, h, and b) particle volume fraction, ϕ, with x at $t = 0.1$ and various values of the light-to-carrying-fluid density ratio, η.

The parameter $\psi = \eta/(1 + (\xi - 1)\phi_0)$ is inversely related to ξ. Therefore, increasing ξ (thus $\hat{V}_t$) meanwhile keeping Re constant may be deduced as an increase in $\hat{\mu}_H(\phi_0) = \hat{\mu}_{f,H}(1 - \phi_0/\phi_j)^{-2}$ or $\hat{\mu}_{f,H}$. Since $\kappa = \hat{\mu}_L/\hat{\mu}_{f,H} = 1$, we shall also have $\hat{\mu}_L$ increasing. As a result, flow deceleration will occur for high ξ which is correspondingly confirmed in figure 3.12a. Furthermore, the increase in volume fraction of particles for high ξ (settling in high viscosity medium) is slightly less than, but still comparable to, that of low ξ owing to the higher density of solids in the former (figure 3.12b).

Finally, the variations of the interface height, h, and particle volume fraction, ϕ, versus the light-to-carrying-fluid density ratio, η, are examined in figures 3.13a and b, respectively. Even though the presented η values are all larger than unity, i.e. light fluid denser than the carrying one, the overall density of the suspension mixture is always larger than the light pure fluid ($\psi < 1$). Note that the interpenetration extent of the mixtures has increased with η (figure 3.13a). Similar to figure 3.12, this effect also appears counter-intuitive at first. Because, an increase in η means a denser light fluid in the lower section of the duct compared to the carrying fluid at the top i.e. a decrease in the effective density difference between the heavy and light mixtures. Increasing η meanwhile keeping Re the same in figure 3.13a, requires, for instance, a reduction in the viscosity of the involved fluids ($Re \propto \hat{\rho}_H(\phi_0)/\hat{\mu}_H(\phi_0)$)

which consequently enhances flow acceleration. The front height on the heavy side slightly decreases with an increase in η. As η increases (while keeping Re constant), mixtures' viscosity decreases, facilitating particles settling and thus enrichment in volume fraction, ϕ, close to the fronts (figure 3.13b). Since r_p, ξ, and η do not affect the mixtures' viscosity ratio, $m = \kappa\left(1-\phi_0/\phi_j\right)^2$, the shape of the interface height obtained in the pure-fluid limit remains unchanged with these parameters; see insets shown in figures 3.11a-3.13a.

3.5 Comparison between theory and experiment

A one-to-one comparison between the results of experiments with those of the modeling may not be possible due to the different flow configurations. In experiments, the exchange domain takes a *slumping* form in which suspension always occupies the lower wall of the pipe, while the pure fluid moves closer to the upper wall. In the modeling, we have considered a *symmetric* configuration to alleviate the singularity at the location of suspension front. In such geometry, particle-laden flow falls alongside both walls, while pure fluid goes through the core of channel. Nevertheless, the result of modeling can correctly capture the exchanging behavior of heavy and light fluids as also observed experimentally. For example in figure 3.14 for pure exchange flow, both in simulation ($\beta = 0°$, $Re = 20$, $m = 1$) and experiment ($\beta = 80°$, $Re = 172$, $m = 1$) the heights h, remains almost unchanged with time. Note that the frontal height is indirectly presented by the average concentration, $\bar{C}$, in the experiment. This assumption is acceptably valid to estimate h for the slumping flow in the absence of interfacial mixing.

In the particle-laden limit, the results of experiment and modeling are also rather comparable. By looking into the figure 3.15, we observe that shape of the suspension front is deformed in both simulation ($\beta = 0°$, $\phi_0 = 0.3$, $Re = 0.1$, $\kappa = 1$, $r_p = 0.06$, $\xi = 1.9$, and $\eta = 1.25$) and experiment ($\beta = 60°$, $\phi_0 = 0.3$, $Re = 1.2$, $\kappa = 1$, $r_p = 0.007$, $\xi = 2.0$, and $\eta = 1$). The trailing fronts, however, evolve in different ways. It is seen

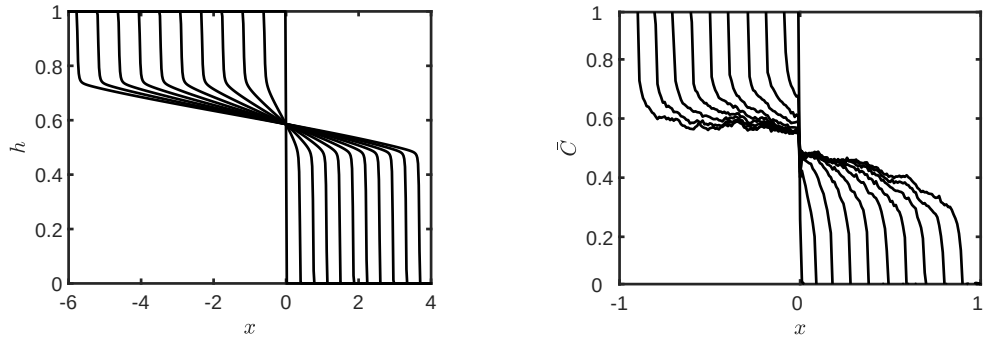

(a) (b)

Figure 3.14: Evolution of (a) interface height, h, with time, $t = [0, 1, \ldots, 10]$, in pure exchange simulation, and (b) mean concentration $\bar{C}$, with time, $t = [1, 12, \ldots, 100]$, in the experiment.

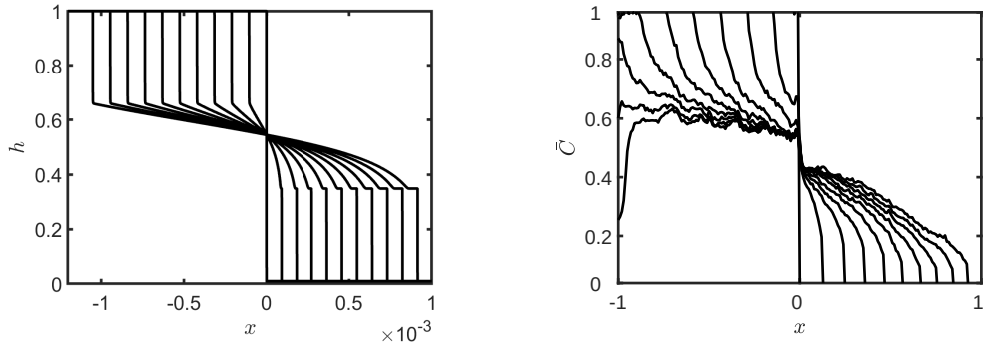

(a) (b)

Figure 3.15: Evolution of (a) interface height, h, with time, $t = [0, 0.01, \ldots, 0.1]$, in particle-laden flow simulation, and (b) mean concentration $\bar{C}$, with time, $t = [1, 85, \ldots, 757]$, in the experiment.

in the experiment (right figure), that the height of trailing front grows erratically over time due to the effective settling across the pipe. Additional experiments need to be carefully designed in order to evaluate the effectiveness of the mathematical model. As well as matching fluids and particle densities, a special gate valve needs to be considered to mimic the flow configuration assumed in the lubrication model, namely, suspension wetting the wall and pure fluid moving through the core.

Chapter 4: Conclusions

4.1 Contributions

Buoyancy-driven particle-laden flows in a narrow lock-exchange pipe (small aspect ratio, $\delta = \hat{D}/\hat{L} \ll 1$) has been initially studied experimentally. Suspension was a mixture of a Newtonian carrying fluid containing negatively-buoyant solid particles with sizes in the range of $\hat{d} \in [20 - 100]\ \mu$m. In the experiments, light fluid was primarily selected as the carrying fluid, thus, the effective density difference between heavy and light phases was solely dependent on the existence of solid particles. Assuming a jamming volume fraction of $\phi_j \approx 0.61$, five dimensionless parameters control the flow, namely, pipe inclination angle, β, particle-to-pipe-diameter ratio, r_p, particle-to-fluid density ratio, ξ, initial volume fraction of particles, ϕ_0 (away from packed limit $\phi_j \rightarrow \phi_j$), and the Reynolds number Re.

- Due to the small density difference (Boussinesq limit) and high viscosity (corresponding to low Reynolds numbers $Re \in [0.10 - 1.72]$), heavy-light interface remains mostly unperturbed showing insignificant mixing across the pipe. As a result, the interpenetration domain is stretched in the form of segregated counter parallel layers of suspension moving downstream, and light pure fluid advancing upstream.

- For pipes even slightly inclined, a novel Boycott-type interface is formed behind the suspension which descends downward along the inclination of pipe. Evolution in the direction of pipe's axis depends on the relative buoyancy of the light and heavy phases which itself is a function of their density difference and the angle of inclination (β from vertical). Sedimentation tends to slow down

the current as it reduces the concentration and consequently diminishes the effective driving density difference. The interpenetration rate was shown to be extremely limited by the trade-off between depthwise settling and streamwise spreading.

- By inclining the pipe from near horizontal to vertical (decreasing β), three distinct regimes have been observed: (1) sedimentary: in the near-horizontal pipes ($\beta \to 90°$) buoyancy force is first balanced by inertia, later by viscosity, and at long times is controlled by sedimentation. The spreading velocity, $\hat{V}_f$, decreases constantly to zero until flow halts at a finite distance. The location and time of the halt is closely related to the density of viscosity of suspension, while both increase with its initial particle concentration ϕ_0. It was observed in our experiments that flows corresponding to intermediate ϕ_0, survive longer and stop further benefiting from rather low viscosity and effective density difference. Besides, halt occurs less frequently by decreasing β. (2) Mixing: away from horizontal ($\beta \to 0°$), depthwise settling hardly affects the spreading of fronts. Particles stay mixed in the suspension and flow develops through a viscous-buoyancy equilibrium. The front velocity, $\hat{V}_f$, then reaches a constant non-zero value. (3) Transition between sedimentary and mixing regime occurs abruptly at angles closer to horizontal. Flow in this regime partly demonstrates the sedimentary and mixing behaviors.

- A classifying method accounting for the profile of the leading front's location, $\hat{X}_f$, have been developed by considering i) straight profile corresponding to the mixing regime, ii) plateaued curve as sedimentary, and iii) regular curve for the transitionary domains. In response to the objectives laid out in chapter 1, the results of this classification have been further plotted on a dimensionless map of β and ϕ_0 applicable for industrial design and planning. It has been revealed

that the mixing flows abound predominately in the range of intermediate ϕ_0 and at high pipe inclinations meaning lower β. Transitionary flows also tend to occur commonly at angles closer to the horizontal for all ϕ_0. A halt was always observed in flows in the near-horizontal pipe over the full range of ϕ_0.

- Average front velocity $\hat{V}_{f,av}$, is generally higher for the flows corresponding to the mixing domain. Using a scaling factor which simultaneously constitutes the viscous effect (depending on the ξ and Re) and Boycott feature (varying with ϕ_0 and r_p) in the flow, allows us to accurately predict the frontal velocity variation at each angle as given in Eq. (2.6). Near-vertical angles exceptionally yield to higher variations than predicted values in absence of Boycott-type convection, suggesting that their front velocities no longer follow similar scaling.

- Protuberances in the form of inertial bumps frequently appeared in our mixing experiments. Particle enrichment along the pipe was insubstantial due to the negligible streamwise motion of particles relative to the fluid (related to Stokes settling velocity, $\hat{u}_0$). However, their migration in depthwise direction has been proved to help keeping them suspended within the carrying fluid.

- By preserving the density contrast between heavy and light fluids (through keeping $\xi \approx 2$), effects of reducing particle size (i.e. reducing r_p) and increasing fluid's viscosity have further been investigated. Essentially, both reduce the settling rate of particles $\hat{u}_0$, with only difference being that by increasing the fluid's viscosity, spreading is further restricted (i.e. reduced Re). Therefore, the sedimentary behavior is diminished if smaller particles are used, while it remains approximately the same regardless of the fluid's viscosity. Consequently, flow undergoes phase changeover at lower angles in the former case, whereas transitions occur invariably over same range of angles during the latter.

In addition to the experimental study, buoyancy-driven exchange flow of two mix-

tures in a vertical duct (2D channel as well as pipe) was investigated theoretically to obtain a better insight of the problem in this configuration. The methodology of [30] for free-surface particle-laden film flows was employed and extended to a lock-exchange system in a confined geometry under the Boussinesq limit. The derived model takes the simple form of the classical Riemann problem. A robust Total Variation Diminishing (TVD) finite difference scheme was implemented to solve the model PDEs numerically. The solutions suggest self-similar interface shapes over time. During this analysis the carrying fluid was assumed to be different than the light fluid, introducing two new dimensionless parameters to the problem, e.g., light-to-carrying-fluid density ratio, η, light-to-carrying-fluid viscosity ratio, κ. In the limit of small aspect ratio ($\delta \ll 1$) and assuming a jamming volume fraction of (here) $\phi_j \approx 0.67$, other dimensionless parameters governing the flow, were namely, particle-radius-to-half-the-duct-width ratio, r_p, particle-to-carrying-fluid density ratio, ξ, initial volume fraction of particles, ϕ_0, and the Reynolds number, Re.

- The physical effect of these parameters on the dynamics of the flow was quantified through a systematic approach. Novel particle-rich zones inside the suspension were further discovered in the vicinity of the advancing heavy and light fronts. The particle enrichment at the fronts is associated with different transport rates of fluid and solid due to the Stokes settling velocity of the particles.

- It was also revealed that geometry confinement plays a significant role in exchange flow dynamics such as formation of interfacial patterns and particle-enrichment behavior. While in the unconfined geometry, particle enrichment was shown to be accompanied by an increase in the interface height profile, in a confined duct, either an increase or decrease in height is possible depending on the controlling parameters of the flow. The level of the particle enrichment remains the same with Re, is enhanced by κ, r_p, and η and is slightly reduced

with ϕ_0 and ξ. The stretched interface between the heavy and light fronts grows with r_p, η, and Re but shrinks with ϕ_0, κ, and ξ.

- By comparing the simulation result with experiment, similar behaviors were observed in both analyses. However, due to the limitation of experimental parameter range as well as different flow configuration in the analytical study a one-to-one comparison was not feasible. Therefore, additional experiments are needed in order to effectively evaluate the mathematical model.

4.2 Future works

In the extension to this work, the effects of bidensity particles in suspension would be of interest. Similar work is the experimental paper by Lee *et al.* (2014) [74] for debris flow. Moreover, the displacement flow of suspension by a Newtonian pure fluid or visa versa, similar to the work of Alba *et al.* (2013) [13], appears to be a valid continuation to our lock-exchange experiments with potential industrial significances, for example, during the fracking process. Meanwhile, the model can be easily extended to include interfacial tension effects; see [58] for similar implementation in the case of pure fluids.

Published papers

Here, I briefly review the contents used in this thesis from papers that are already accepted for publication or are currently under review. I also mention the extent of contribution of collaborators and co-authors in the papers.

- **N. Mirzaeian**, and K. Alba. *Particle-laden exchange flows in inclined pipes.* ***Prepared for submission to Phys. Rev. Fluids.***

  This work is primarily experimental study of exchange flow of a particle-laden mixture releasing into a pure fluid within a lock-exchange pipe geometry. The suspension consists of solid microspheres with size $20-100\,\mu$m being suspended in pure Newtonian fluid. It is shown that the flow evolution is primarily determined by a trade-off between the depthwise settling and streamwise buoyant spreading mechanisms. Various sedimentary, transitionary, and mixing regimes are classified and the results are mapped onto dimensionless diagrams suitable for industrial design. A scaling model for the advancing front velocity is developed accounting for multiple flow parameters as well as the geometry. Effects of particle size and the viscosity of interstitial fluid are further investigated. The novelty of this work is in extending the fundamental study of particulate exchange flows in strictly horizontal channels by Saha *et al.* (2013) [32] to an inclined practical pipe. The key finding of this paper is identifying a dimensionless mixing domain marked by intermediate initial volume fraction of particles, ϕ_0, and lower inclination angle, β, measured from the vertical direction. I conducted the experiments and wrote the paper while benefiting useful comments from K. Alba. I also supervised co-op student, Hector Garza, in realizing the experimental apparatus who is also acknowledged in the paper. This research was supervised by K. Alba.

- **N. Mirzaeian**, and K. Alba. *Monodisperse particle-laden exchange flow in a vertical duct.* ***Accepted for publication in J. Fluid Mech.***

  This paper theoretically studies the particle-laden exchange problem in a strictly vertical configuration. A 1D lubrication model similar to the methodology of Cook *et al.* (2008) [31] for free-surface thin-film flow, is developed for channel and pipe geometries. The resulting model, which is in the form of classical Riemann problem, is further solved numerically using a robust Total Variation Diminishing (TVD) finite difference scheme. It is observed that the interface between two fluids takes a self-similar shape at long times. The effects of various independent controlling parameters of the flow are quantified through a systematic approach. The novel result of this work is identifying a particle-enriched zone close to the advancing contact line of suspension. Interestingly, it is shown that particle enrichment in a confined geometry, can be accompanied by either an increase or decrease in frontal height depending on the different flow parameters. The paper was written by K. Alba. He developed the mathematical model in close collaboration with myself (particularly on shear-induced migration section and relevance to Zhou *et al.* (2005) [30] and Saha *et al.* (2013) [32] models) and carried out the numerical simulations. Moreover, I read the paper and provided comments prior to the submission as well as during two detailed rounds of revisions through communication with external referees. This research was supervised by K. Alba.

Bibliography

[1] T. B. Benjamin, "Gravity currents and related phenomena," *Journal of Fluid Mechanics*, vol. 31, no. 2, pp. 209–248, 1968.

[2] J. Shin, S. Dalziel, and P. Linden, "Gravity currents produced by lock exchange," *Journal of Fluid Mechanics*, vol. 521, pp. 1–34, 2004.

[3] V. Birman, B. Battandier, E. Meiburg, and P. Linden, "Lock-exchange flows in sloping channels," *Journal of Fluid Mechanics*, vol. 577, pp. 53–77, 2007.

[4] M. Baird, K. Aravamudan, N. Rao, J. Chadam, and A. Peirce, "Unsteady axial mixing by natural convection in a vertical column," *AIChE journal*, vol. 38, no. 11, pp. 1825–1834, 1992.

[5] H. Pratt and M. Baird, "Axial dispersion," *Handbook of Solvent Extraction*, p. 199, 1983.

[6] G. Segre, "Radial particle displacements in poseuille flow of suspensions," *Nature*, vol. 189, pp. 209–210, 1961.

[7] J. A. Wiklund, M. Stading, A. J. Pettersson, and A. Rasmuson, "A comparative study of uvp and lda techniques for pulp suspensions in pipe flow," *AIChE Journal*, vol. 52, no. 2, pp. 484–495, 2006.

[8] E. Nelson and D. Guillot, "Well cementing, 773," *Sugar Land, Texas: Schlumberger*, 2006.

[9] A. A. Boateng, *Rotary kilns: transport phenomena and transport processes*. Butterworth-Heinemann, 2015.

[10] A. Asomah and T. Napier-Munn, "An empirical model of hydrocyclones incorporating angle of cyclone inclination," *Minerals Engineering*, vol. 10, no. 3, pp. 339–347, 1997.

[11] A. M. Hamed, "Experimental investigation on the adsorption/desorption processes using solid desiccant in an inclined-fluidized bed," *Renewable Energy*, vol. 30, no. 12, pp. 1913–1921, 2005.

[12] K. Alba, S. Taghavi, and I. Frigaard, "Miscible density-stable displacement flows in inclined tube," *Physics of Fluids*, vol. 24, no. 12, p. 123 102, 2012.

[13] ——, "Miscible density-unstable displacement flows in inclined tube," *Physics of Fluids*, vol. 25, no. 6, p. 067 101, 2013.

[14] K. Alba, "Displacement flow of complex fluids in an inclined duct," PhD thesis, University of British Columbia, 2013.

[15] M. Debacq, V. Fanguet, J.-P. Hulin, D. Salin, and B. Perrin, "Self-similar concentration profiles in buoyant mixing of miscible fluids in a vertical tube," *Physics of fluids*, vol. 13, no. 11, pp. 3097–3100, 2001.

[16] T. Séon, J.-P. Hulin, D. Salin, B. Perrin, and E. Hinch, "Buoyancy driven miscible front dynamics in tilted tubes," *Physics of Fluids*, vol. 17, no. 3, p. 031 702, 2005.

[17] T. Séon, J. Znaien, D. Salin, J. Hulin, E. Hinch, and B. Perrin, "Transient buoyancy-driven front dynamics in nearly horizontal tubes," *Physics of Fluids*, vol. 19, no. 12, p. 123 603, 2007.

[18] T. Séon, J. Znaien, B. Perrin, E. Hinch, D. Salin, and J. Hulin, "Front dynamics and macroscopic diffusion in buoyant mixing in a tilted tube," *Physics of Fluids*, vol. 19, no. 12, p. 125 105, 2007.

[19] S. Taghavi, T. Seon, D. Martinez, and I. Frigaard, "Buoyancy-dominated displacement flows in near-horizontal channels: The viscous limit," *Journal of Fluid Mechanics*, vol. 639, pp. 1–35, 2009.

[20] K. Alba, S. Taghavi, and I. Frigaard, "A weighted residual method for two-layer non-newtonian channel flows: Steady-state results and their stability," *Journal of Fluid Mechanics*, vol. 731, pp. 509–544, 2013.

[21] Z. Borden and E. Meiburg, "Circulation-based models for boussinesq internal bores," *Journal of Fluid Mechanics*, vol. 726, 2013.

[22] K. Sahu and S. Vanka, "A multiphase lattice boltzmann study of buoyancy-induced mixing in a tilted channel," *Computers & Fluids*, vol. 50, no. 1, pp. 199–215, 2011.

[23] S. Taghavi, K. Alba, and I. Frigaard, "Buoyant miscible displacement flows at moderate viscosity ratios and low atwood numbers in near-horizontal ducts," *Chemical engineering science*, vol. 69, no. 1, pp. 404–418, 2012.

[24] K. Alba, S. Taghavi, and I. Frigaard, "Miscible heavy-light displacement flows in an inclined two-dimensional channel: A numerical approach," *Physics of Fluids*, vol. 26, no. 12, p. 122 104, 2014.

[25] W. D. Hill, R. Rothfus, and K. Li, "Boundary-enhanced sedimentation due to settling convection," *International Journal of Multiphase Flow*, vol. 3, no. 6, pp. 561–583, 1977.

[26] A. Acrivos and E. Herbolzheimer, "Enhanced sedimentation in settling tanks with inclined walls," *Journal of fluid mechanics*, vol. 92, no. 3, pp. 435–457, 1979.

[27] E. Herbolzheimer and A. Acrivos, "Enhanced sedimentation in narrow tilted channels," *Journal of Fluid Mechanics*, vol. 108, pp. 485–499, 1981.

[28] R. T. Bonnecaze, H. E. Huppert, and J. R. Lister, "Particle-driven gravity currents," *Journal of Fluid Mechanics*, vol. 250, pp. 339–369, 1993.

[29] E. Meiburg and B. Kneller, "Turbidity currents and their deposits," *Annual Review of Fluid Mechanics*, vol. 42, pp. 135–156, 2010.

[30] J. Zhou, B. Dupuy, A. Bertozzi, and A. Hosoi, "Theory for shock dynamics in particle-laden thin films," *Physical review letters*, vol. 94, no. 11, p. 117 803, 2005.

[31] B. P. Cook, A. L. Bertozzi, and A. Hosoi, "Shock solutions for particle-laden thin films," *SIAM Journal on Applied Mathematics*, vol. 68, no. 3, pp. 760–783, 2008.

[32] S. Saha, D. Salin, and L. Talon, "Low reynolds number suspension gravity currents," *The European Physical Journal E*, vol. 36, no. 8, p. 85, 2013.

[33] C. Mouquet, V. Greffeuille, and S. Treche, "Characterization of the consistency of gruels consumed by infants in developing countries: Assessment of the bostwick consistometer and comparison with viscosity measurements and sensory perception," *International journal of food sciences and nutrition*, vol. 57, no. 7-8, pp. 459–469, 2006.

[34] N. Mirzaeian and K. Alba, "Monodisperse particle-laden exchange flows in a vertical duct," *Journal of fluid mechanics*, 2018, Accepted.

[35] A. Hasnain, E. Segura, and K. Alba, "Buoyant displacement flow of immiscible fluids in inclined pipes," *Journal of Fluid Mechanics*, vol. 824, pp. 661–687, 2017.

[36] B. Eslami, S. Shariatnia, H. Ghasemi, and K. Alba, "Non-isothermal buoyancy-driven exchange flows in inclined pipes," *Physics of Fluids*, vol. 29, no. 6, p. 062 108, 2017.

[37] L. Espn and S. Kumar, "Forced spreading of films and droplets of colloidal suspensions," *Journal of Fluid Mechanics*, vol. 742, pp. 495–519, 2014.

[38] M. Haw, "Jamming, two-fluid behavior, and self-filtration in concentrated particulate suspensions," *Physical review letters*, vol. 92, no. 18, p. 185 506, 2004.

[39] C. Ancey, N. Andreini, and G. Epely-Chauvin, "Granular suspension avalanches. i. macro-viscous behavior," *Physics of Fluids*, vol. 25, no. 3, p. 033 301, 2013.

[40] I. M. Krieger, "Rheology of monodisperse latices," *Advances in Colloid and Interface science*, vol. 3, no. 2, pp. 111–136, 1972.

[41] S. H. Maron and P. E. Pierce, "Application of ree-eyring generalized flow theory to suspensions of spherical particles," *Journal of colloid science*, vol. 11, no. 1, pp. 80–95, 1956.

[42] J. B. Segur and H. E. Oberstar, "Viscosity of glycerol and its aqueous solutions," *Industrial & Engineering Chemistry*, vol. 43, no. 9, pp. 2117–2120, 1951.

[43] J. Richardson and W. Zaki, "The sedimentation of a suspension of uniform spheres under conditions of viscous flow," *Chemical Engineering Science*, vol. 3, no. 2, pp. 65–73, 1954.

[44] J.-C. Bacri, C. Frenois, M. Hoyos, R. Perzynski, N. Rakotomalala, and D. Salin, "Acoustic study of suspension sedimentation," *EPL (Europhysics Letters)*, vol. 2, no. 2, p. 123, 1986.

[45] J. Martin, N. Rakotomalala, and D. Salin, "Accurate determination of the sedimentation flux of concentrated suspensions," *Physics of Fluids*, vol. 7, no. 10, pp. 2510–2512, 1995.

[46] D. Leighton and A. Acrivos, "The shear-induced migration of particles in concentrated suspensions," *Journal of Fluid Mechanics*, vol. 181, pp. 415–439, 1987.

[47] R. J. Phillips, R. C. Armstrong, R. A. Brown, A. L. Graham, and J. R. Abbott, "A constitutive equation for concentrated suspensions that accounts for shear-induced particle migration," *Physics of Fluids A: Fluid Dynamics*, vol. 4, no. 1, pp. 30–40, 1992.

[48] B. P. Cook, "Theory for particle settling and shear-induced migration in thin-film liquid flow," *Physical Review E*, vol. 78, no. 4, p. 045 303, 2008.

[49] S. Taghavi, T. Seon, D. Martinez, and I. Frigaard, "Influence of an imposed flow on the stability of a gravity current in a near horizontal duct," *Physics of Fluids*, vol. 22, no. 3, p. 031 702, 2010.

[50] B. Cook, O. Alexandrov, and A. Bertozzi, "Linear stability of particle-laden thin films," *The European Physical Journal Special Topics*, vol. 166, no. 1, pp. 77–81, 2009.

[51] R. Kerswell, "Exchange flow of two immiscible fluids and the principle of maximum flux," *Journal of Fluid Mechanics*, vol. 682, pp. 132–159, 2011.

[52] R. Davies and S. G. Taylor, "The mechanics of large bubbles rising through extended liquids and through liquids in tubes," in *Dynamics of Curved Fronts*, Elsevier, 1988, pp. 377–392.

[53] K. Alba, P. Laure, and R. E. Khayat, "Transient two-layer thin-film flow inside a channel," *Physical Review E*, vol. 84, no. 2, p. 026 320, 2011.

[54] S. M. Taghavi, K. Alba, T. Séon, K. Wielage-Burchard, D. Martinez, and I. Frigaard, "Miscible displacement flows in near-horizontal ducts at low atwood number," *Journal of Fluid Mechanics*, vol. 696, pp. 175–214, 2012.

[55] B. Metzger, E. Guazzelli, and J. E. Butler, "Large-scale streamers in the sedimentation of a dilute fiber suspension," *Physical review letters*, vol. 95, no. 16, p. 164 506, 2005.

[56] A. Mavromoustaki and A. Bertozzi, "Hyperbolic systems of conservation laws in gravity-driven, particle-laden thin-film flows," *Journal of Engineering Mathematics*, vol. 88, no. 1, pp. 29–48, 2014.

[57] L. Wang and A. L. Bertozzi, "Shock solutions for high concentration particle-laden thin films," *SIAM Journal on Applied Mathematics*, vol. 74, no. 2, pp. 322–344, 2014.

[58] A. Hasnain and K. Alba, "Buoyant displacement flow of immiscible fluids in inclined ducts: A theoretical approach," *Physics of Fluids*, vol. 29, no. 5, p. 052 102, 2017.

[59] P. Petitjeans and T. Maxworthy, "Miscible displacements in capillary tubes. part 1. experiments," *Journal of Fluid Mechanics*, vol. 326, pp. 37–56, 1996.

[60] H. P. Greenspan, "On the motion of a small viscous droplet that wets a surface," *Journal of Fluid Mechanics*, vol. 84, no. 1, pp. 125–143, 1978.

[61] M. Spaid and G. Homsy, "Stability of newtonian and viscoelastic dynamic contact lines," *Physics of Fluids*, vol. 8, no. 2, pp. 460–478, 1996.

[62] A. Kurganov and E. Tadmor, "New high-resolution central schemes for nonlinear conservation laws and convection–diffusion equations," *Journal of Computational Physics*, vol. 160, no. 1, pp. 241–282, 2000.

[63] J. Martin, N. Rakotomalala, L. Talon, and D. Salin, "Viscous lock-exchange in rectangular channels," *Journal of Fluid Mechanics*, vol. 673, pp. 132–146, 2011.

[64] G. P. Matson and A. J. Hogg, "Viscous exchange flows," *Physics of Fluids*, vol. 24, no. 2, p. 023 102, 2012.

[65] Z. Zheng, L. Rongy, and H. A. Stone, "Viscous fluid injection into a confined channel," *Physics of fluids*, vol. 27, no. 6, p. 062 105, 2015.

[66] M. Lyon and L. Leal, "An experimental study of the motion of concentrated suspensions in two-dimensional channel flow. part 1. monodisperse systems," *Journal of Fluid Mechanics*, vol. 363, pp. 25–56, 1998.

[67] F. Auzerais, R. Jackson, and W. Russel, "The resolution of shocks and the effects of compressible sediments in transient settling," *Journal of Fluid Mechanics*, vol. 195, pp. 437–462, 1988.

[68] N. Grunewald, R. Levy, M. Mata, T. Ward, and A. L. Bertozzi, "Self-similarity in particle-laden flows at constant volume," *Journal of Engineering Mathematics*, vol. 66, no. 1-3, pp. 53–63, 2010.

[69] M. R. Mata and A. L. Bertozzi, "A numerical scheme for particle-laden thin film flow in two dimensions," *Journal of Computational Physics*, vol. 230, no. 16, pp. 6334–6353, 2011.

[70] N. Murisic, J. Ho, V. Hu, P. Latterman, T. Koch, K. Lin, M. Mata, and A. Bertozzi, "Particle-laden viscous thin-film flows on an incline: Experiments compared with a theory based on shear-induced migration and particle settling," *Physica D: Nonlinear Phenomena*, vol. 240, no. 20, pp. 1661–1673, 2011.

[71] N. Murisic, B. Pausader, D. Peschka, and A. L. Bertozzi, "Dynamics of particle settling and resuspension in viscous liquid films," *Journal of Fluid Mechanics*, vol. 717, pp. 203–231, 2013.

[72] L. Wang, A. Mavromoustaki, A. Bertozzi, G. Urdaneta, and K. Huang, "Rarefaction-singular shock dynamics for conserved volume gravity driven particle-laden thin film," *Physics of Fluids*, vol. 27, no. 3, p. 033 301, 2015.

[73] J. T. Wong and A. L. Bertozzi, "A conservation law model for bidensity suspensions on an incline," *Physica D: Nonlinear Phenomena*, vol. 330, pp. 47–57, 2016.

[74] S. Lee, A. Mavromoustaki, G. Urdaneta, K. Huang, and A. L. Bertozzi, "Experimental investigation of bidensity slurries on an incline," *Granular Matter*, vol. 16, no. 2, pp. 269–274, 2014.

[75] U. Schaflinger, A. Acrivos, and K. Zhang, "Viscous resuspension of a sediment within a laminar and stratified flow," *International Journal of Multiphase Flow*, vol. 16, no. 4, pp. 567–578, 1990.

[76] A. Acrivos, X. Fan, and R. Mauri, "On the measurement of the relative viscosity of suspensions," *Journal of Rheology*, vol. 38, no. 5, pp. 1285–1296, 1994.

[77] S. Taghavi, T. Seon, K. Wielage-Burchard, D. Martinez, and I. Frigaard, "Stationary residual layers in buoyant newtonian displacement flows," *Physics of Fluids*, vol. 23, no. 4, p. 044 105, 2011.

[78] J. Wong, "Modeling and analysis of thin-film incline flow: Bidensity suspensions and surface tension effects," PhD thesis, University of California (Los Angles), 2017.

Appendix A: Benchmarking against pure (particle-free) exchange flow study of Seon *et al.* (2005) [16]

We used solution of water and NaCl salt for the heavy fluid, and fresh water dyed with non-waterproof black ink (1600 mg/l) for the light one. Density difference between heavy and light fluids was characterized by Atwood number as $At = (\hat{\rho}_H - \hat{\rho}_L)/(\hat{\rho}_H + \hat{\rho}_L) = (1-\psi)/(1+\psi)$ and interpenetrating rate by Reynolds number, $Re_t = \hat{V}_t \hat{D}/\hat{\nu}_f$. We performed 33 experiments covering $\beta = 0° - 88°$ and At=0.0035, 0.01 and 0.04 ($Re_t \in [170, 600]$). Validity of these experiments are ensured via four ways: (1) Seon *et al.* [16] classified various viscous, transitionary, and mixing regimes using the dimensionless controlling parameter $Re_t \cos\beta$. This quantity represents the relative strength of streamwise buoyant $\Delta\hat{\rho}\hat{g}\hat{D}\cos\beta$ to viscous stresses $\hat{\mu}\hat{V}_t/\hat{D}$ [13]. Seon *et al.* [16] found the changeover from viscous to transitionary flows happens at $Re_t \cos\beta \approx 50$. Our experimental results presented in figure A.1a also confirm such transition. Different regimes are denoted as viscous (●), transitionary (■), and diffusive (▲); different colors correspond to At = 0.0035 (red), At = 0.01 (yellow), and At = 0.04 (blue).

(2) The frontal velocity variation with inclination in the viscous domain is reported as $\hat{V}_f/\hat{V}_t = \left(1/16 - 1/\left(2\pi^2\right)\right) Re_t \cos\beta$ [16] which is in close agreement to our prediction shown as inclined dashed line in figure A.1a. (3) Furthermore, in the same figure, frontal velocities in the transitionary domain collapse onto a plateau with maximum value $\hat{V}_f/\hat{V}_t \approx 0.7$ as shown by horizontal dashed line remaining almost independent of inclination. (4) The heavy and light interpenetrating velocities in the diffusive flow domain are relatively low due to the effective transverse mixing [16]. For such flows, it is valid to assume a rather stationary mixing core and

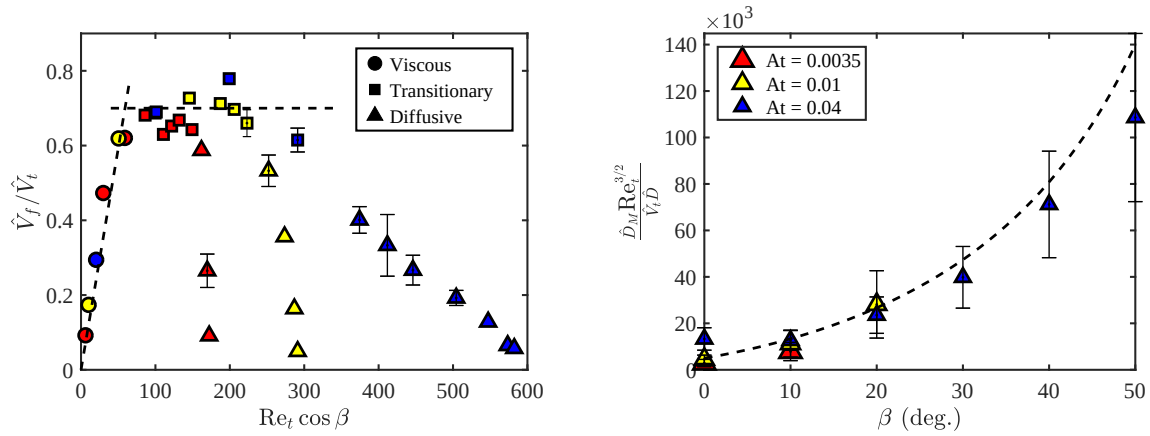

(a) (b)

Figure A.1: Benchmarking result of experiments for pure fluid against Ref. [16]: (a) dependency of $\hat{V}_f/\hat{V}_t$ on $Re_t \cos\beta$, (b) variation of the dimensionless macroscopic diffusion coefficient versus inclination angle β, and Atwood number At.

use $\hat{x}/\sqrt{\hat{t}}$ as a similarity parameter [18]. Thus, flow is controlled by a linear diffusion equation,

$$\frac{\partial \bar{C}}{\partial \hat{t}} = \hat{D}_M \frac{\partial^2 \bar{C}}{\partial \hat{x}^2}. \tag{A.1}$$

Here, $\hat{D}_M$ is a *macroscopic* diffusion coefficient which may be $O(10^5)$ greater than the molecular diffusivity $\hat{D}_m$, and is determined by fitting the averaged concentration profile $\bar{C}(\hat{x},\hat{t})$, to solutions of the diffusion equation (A.1). Our measured $\hat{D}_M$ for diffusive experiments in figure A.1b obey the expression proposed by Seon *et al.* [18],

$$\frac{\hat{D}_M Re_t^{3/2}}{\hat{V}_t \hat{D}} = 5 \times 10^3 (1 + 3.6 \tan\beta)^2, \tag{A.2}$$

for $Re_t \lesssim 1000$, which covers the range of our pure exchange experiments. Note that our macroscopic measurements in figure A.1b agree with Eq. (A.2), and deviations are comparably similar to those in Ref. [18, 36].

Appendix B: Shear-induced migration effects

Migration of particles induced by shear is in fact an important effect widely observed in particle-laden flows. Our methodology follows the approach of [30] for gravity driven suspension film down an incline which neglects shear-induced migration effect ([75, 76]). In this Appendix we would like to verify under what condition such assumption is valid. The particle transport equation for particle-laden film flows is given by [71] and [73] as

$$\phi_{\hat{t}} + \hat{u}\phi_{\hat{x}} + \hat{v}\phi_{\hat{y}} = -\hat{\mathbf{J}}_{\hat{x},\hat{x}} - \hat{\mathbf{J}}_{\hat{y},\hat{y}}. \tag{B.1}$$

Here, $\hat{\mathbf{J}}$ is the particle flux due to settling and migration

$$\hat{\mathbf{J}} = \hat{\mathbf{J}}_{Settling} + \hat{\mathbf{J}}_{Migration}. \tag{B.2}$$

The settling and migration flux components can be expressed as the following ([71, 73])

$$\hat{\mathbf{J}}_{settling} = \frac{2\hat{a}^2\hat{g}\left(\hat{\rho}_p - \hat{\rho}_{f,H}\right)}{9\hat{\mu}_{f,H}}\left(1-\phi\right)\phi, \tag{B.3}$$

$$\hat{\mathbf{J}}_{Migration} = -\frac{\hat{a}^2\hat{V}_t}{\hat{D}^2}\left[K_c\phi\nabla\left(\phi u_y\right) + \frac{K_v\phi^2 u_y}{\mu_H}\nabla\mu_H\right]. \tag{B.4}$$

The constants $K_c \approx 0.41$ and $K_v \approx 0.62$ correspond to shear-induced particle flux due to gradients in the particle volume fraction and effective viscosity of the suspension which are determined empirically ([47, 73]). From the velocity expression (3.15), it can be found that $u_y \sim Re$; see also Appendix D for the coefficients. Therefore, the largest flux component due to shear-induced migration in (B.4) is of order

$K_v\hat{a}^2\hat{V}_tRe/\hat{D}^2$, whereas that of settling is the coefficient of $\left(1-\phi\right)\phi$ term in (F.14) i.e. $2\hat{a}^2\hat{g}(\hat{\rho}_p-\hat{\rho}_{f,H})/(9\hat{\mu}_{f,H})$. Note that the rest of the terms in (F.14) and (B.4) being multiplied by these coefficients are $O(1)$ since they are made dimensionless. By requiring the settling effects overcoming those of migration ($\hat{\mathbf{J}}_{settling} \gg \hat{\mathbf{J}}_{Migration}$), the following condition is finally obtained

$$\frac{9K_v\eta\left(1-\phi_0/\phi_j\right)^2}{\psi(\xi-1)}\frac{\left(1-\psi\right)}{\left(1+\psi\right)} \ll 1. \tag{B.5}$$

Note that the $(1-\psi)/(1+\psi)$ term in (B.5) is nothing but the effective Atwood number, $At=(\hat{\rho}_H(\phi_0)-\hat{\rho}_L)/(\hat{\rho}_H(\phi_0)+\hat{\rho}_L)$. In other words, the Boussinesq limit ($At \ll 1$), discussed by [54], ensures that the shear-induced migration effects are negligible in front of settling. Note the rest of the terms in (B.5) are approximately $O(1)$. From a fundamental standpoint, the small Atwood number or density difference between the mixtures does not cause strong counter-current and shear in the flow which would lead to migration. However, in the meantime, the particles would have the opportunity to settle due to their weight. The condition (B.5) is indeed valid in the simulations presented in this paper. For instance, for a typical set of parameter chosen in our study e.g. in figure 3.6, the left-hand-side term in condition above is approximately 0.019 i.e. settling flux more than 50 times stronger than that of shear-induced migration.

Appendix C: Axisymmetric flow in pipe

Performing exchange flow experiments in a pipe geometry can be more feasible compared to the 2D channel one. Therefore, in this appendix the exchange flow model is extended to a practical pipe geometry; see figure C.1. It is not difficult to show that in cylindrical coordinate the momentum equations (3.9) and (3.10) take the following form

$$0 = -P_{0,x} + \mu_H(\phi)(ru_r)_r/r, \qquad 1-h \le r \le 1, \tag{C.1}$$

$$0 = -P_{0,x} - (\rho_H(\phi) - \psi)Re/(1-\psi) + m(ru_r)_r/r, \qquad 0 \le r \le 1-h. \tag{C.2}$$

Applying appropriate boundary and interfacial conditions, the equations (C.1) and (C.2) can be integrated with respect to r in order to determine the streamwise velocity closures in each layer. The flux function, $q = \hat{q}/(\pi\hat{D}^2\hat{V}_t)$, as the flow rate within the heavy layer can eventually be calculated as

$$q = 2\int_{1-h}^{1} rudr, \tag{C.3}$$

which is given below as function of h, Re, m, μ_H, ρ_H, and ψ

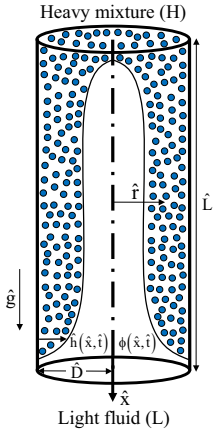

Figure C.1: Schematic of axisymmetric particle-laden exchange flow in a vertical pipe.

$$
\begin{aligned}
q \;=\; & -(1/8)Re(-4\ln(1-h)\mu_H\psi - 104h^6 m\psi - 144h^5\mu_H\psi + 176h^5 m\psi - 80h^3 m\rho_H + \\
& 16h^2 m\rho_H + 164h^4 m\rho_H + 144h^5\mu_H\rho_H + 104h^6 m\rho_H + 80h^6\mu_H\psi + 92h^3\mu_H\rho_H - \\
& 30h^2\mu_H\rho_H + 4h\mu_H\rho_H - 4h^8 m\psi + 32h^7 m\psi + 4h^8 m\rho_H - 32h^7 m\rho_H - 24h^7\mu_H\psi + \\
& 24h^7\mu_H\rho_H + 3h^8\mu_H\psi - 3h^8\mu_H\rho_H + 280\ln(1-h)h^4\mu_H\rho_H - 208\ln(1-h)h^3 m\psi + \\
& 208\ln(1-h)h^3 m\rho_H + 224\ln(1-h)h^3\mu_H\psi - 224\ln(1-h)h^3\mu_H\rho_H - 112\ln(1-h)h^2\mu_H\psi + \\
& 112\ln(1-h)h^2\mu_H\rho_H + 32\ln(1-h)h\mu_H\psi - 32\ln(1-h)h\mu_H\rho_H + 88\ln(1-h)h^2 m\psi - \\
& 88\ln(1-h)h^2 m\rho_H - 16\ln(1-h)hm\psi + 16\ln(1-h)hm\rho_H + 4\ln(1-h)h^8 m\psi - 32\ln(1-h)h^7 m\psi - \\
& 4\ln(1-h)h^8 m\rho_H + 32\ln(1-h)h^7 m\rho_H - 4\ln(1-h)h^8\mu_H\psi + 32\ln(1-h)h^7\mu_H\psi + \\
& 4\ln(1-h)h^8\mu_H\rho_H - 32\ln(1-h)h^7\mu_H\rho_H + 112\ln(1-h)h^6 m\psi - 112\ln(1-h)h^6 m\rho_H - \\
& 112\ln(1-h)h^6\mu_H\psi + 112\ln(1-h)h^6\mu_H\rho_H - 224\ln(1-h)h^5 m\psi + 224\ln(1-h)h^5 m\rho_H + \\
& 224\ln(1-h)h^5\mu_H\psi - 224\ln(1-h)h^5\mu_H\rho_H + 276\ln(1-h)h^4 m\psi - 276\ln(1-h)h^4 m\rho_H - \\
& 280\ln(1-h)h^4\mu_H\psi - 92h^3\mu_H\psi - 164h^4 m\psi - 4h\mu_H\psi + 30h^2\mu_H\psi + 80h^3 m\psi - \\
& 16h^2 m\psi + 151h^4\mu_H\psi - 151h^4\mu_H\rho_H - 80h^6\mu_H\rho_H - 176h^5 m\rho_H + 4\ln(1-h)\mu_H\rho_H)/ \\
& (\mu_H(h^4 m\psi - h^4\mu_H\psi - h^4 m + h^4\mu_H - 4h^3 m\psi + 4h^3\mu_H\psi + 4h^3 m - 4h^3\mu_H + 6h^2 m\psi - \\
& 6h^2\mu_H\psi - 6h^2 m + 6h^2\mu_H - 4hm\psi + 4h\mu_H\psi + 4hm - 4h\mu_H - \mu_H\psi + \mu_H)). \qquad \text{(C.4)}
\end{aligned}
$$

Similar to (3.21) and (3.22), the evolution equations for the interface height and particle volume fraction in cylindrical coordinate respectively read

$$H_t + F_x(H,\Theta) = 0, \qquad \text{(C.5)}$$

$$\Theta_t + G_x(H,\Theta) = 0, \qquad \text{(C.6)}$$

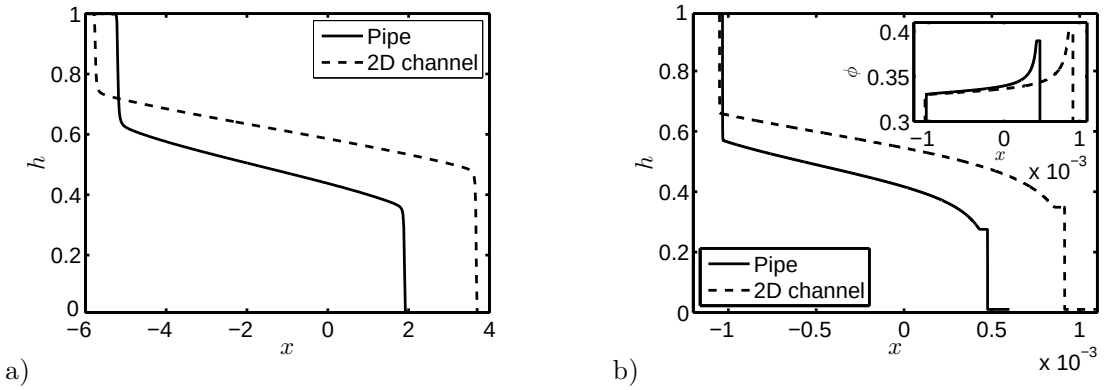

Figure C.2: Comparison of the interface height profile, h, for a) pure fluid ($\phi_0 = 0$) and b) particle-laden cases ($\phi_0 = 0.3$) between pipe and 2D channel. The inset in part b depicts the corresponding profile of volume fraction, ϕ.

where, $H = (1-h)^2$, $\Theta = \theta\left(1-(1-h)^2\right)/h$, and

$$F(H,\Theta) = -q(H,\Theta), \tag{C.7}$$

$$G(H,\Theta) = -\frac{\Theta F(H,\Theta)}{1-H} + u_0\Theta\left(1-\frac{\Theta}{1-H}\right) f(H,\Theta)\, w(H). \tag{C.8}$$

See derivation in the appendix G. Using exact same numerical scheme as the one explained in section 3.3, system of PDEs (C.5) and (C.6) can be solved to give evolution of H and Θ (thus h and ϕ) in space, x, and time, t. Figures C.2a and b show sample computed results in pipe geometry for pure fluid ($\phi_0 = 0$) and suspension cases ($\phi_0 = 0.3$) respectively. Figure C.2a compares the pipe interface profile with that of 2D channel shown earlier in figure 3.3a. The effect of geometry on spreading of heavy and light layers is evident. The computed heavy/light frontal shock heights ($h_{HF} \approx 0.36$ and $h_{LF} \approx 0.63$) were successfully compared to those obtained from equal-area rule in pipe; see also (3.37)-(3.38) and [77]

$$q(h_{Hf}) = \left(1-(1-h_{HF})^2\right) q_h(h_{Hf})/[2(1-h_{HF})], \tag{C.9}$$

$$-q(h_{Lf}) = (1-h_{LF})^2 q_h(h_{Lf})/[2(1-h_{LF})]. \tag{C.10}$$

Figure C.2b compares the pipe interface profile against that of 2D channel shown earlier in figure 3.6 for particle-laden case. The inset depicts corresponding profile of volume fraction, ϕ. Similar particle enrichment effect as to the 2D channel case is observed with only slight modification due to the geometric difference. Figure C.2 suggests that the heavy and light frontal height, h, is larger in the case of channel compared to the pipe. Moreover, the exchange flow overall advances more rapidly in the former.

Appendix D: Coefficients in velocity expressions (3.15) and (3.16) for 2D channel case

$$
\begin{aligned}
P_{0,x} &= -[(3h^3m - 2h^3\mu_H - 9h^2m + 6h^2\mu_H + 6hm - 6h\mu_H + 2\mu_H)\psi - \\
&\quad 3h^3m\rho_H + 2h^3\mu_H\rho_H + 9h^2m\rho_H - 6h^2\mu_H\rho_H - 6hm\rho_H + 6h\mu_H\rho_H - 2\mu_H\rho_H]Re/ \\
&\quad [2(\psi - 1)(h^3m - h^3\mu_H - 3h^2m + 3h^2\mu_H + 3hm - 3h\mu_H + \mu_H)], \qquad \text{(D.1)} \\
c_1 &= [(2h^3m - 2h^3\mu_H - 5h^2m + 6h^2\mu_H + 3hm - 6h\mu_H + 2\mu_H)\psi - \\
&\quad 2h^3m\rho_H + 2h^3\mu_H\rho_H + 5h^2m\rho_H - 6h^2\mu_H\rho_H - 3hm\rho_H + 6h\mu_H\rho_H - \\
&\quad 2\mu_H\rho_H]hRe/[2\mu_H((h^3m - h^3\mu_H - 3h^2m + 3h^2\mu_H + 3hm - 3h\mu_H + \mu_H)\psi - \\
&\quad h^3m + h^3\mu_H + 3h^2m - 3h^2\mu_H - 3hm + 3h\mu_H - \mu_H)], \qquad \text{(D.2)} \\
c_2 &= 0, \qquad \text{(D.3)} \\
d_1 &= [(h - 3)\psi - h\rho_H + 3\rho_H]h^2Re/ \\
&\quad [2(\psi - 1)(h^3m - h^3\mu_H - 3h^2m + 3h^2\mu_H + 3hm - 3h\mu_H + \mu_H)], \qquad \text{(D.4)} \\
d_2 &= [(h^3m - h^3\mu_H - h^2m + h^2\mu_H + 2\mu_H)\psi - h^3m\rho_H + h^3\mu_H\rho_H + h^2m\rho_H - \\
&\quad h^2\mu_H\rho_H - 2\mu_H\rho_H]h^2Re/ \\
&\quad [4\mu_H(\psi - 1)(h^3m - h^3\mu_H - 3h^2m + 3h^2\mu_H + 3hm - 3h\mu_H + \mu_H)]. \qquad \text{(D.5)}
\end{aligned}
$$

Appendix E: Flux function, q, in (3.17) for 2D channel case

$$
\begin{aligned}
q \;=\; & [(3h^3m - 4h^3\mu_H - 6h^2m + 12h^2\mu_H + 3hm - 12h\mu_H + 4\mu_H)\psi - 3h^3m\rho_H + \\
& 4h^3\mu_H\rho_H + 6h^2m\rho_H - 12h^2\mu_H\rho_H - 3hm\rho_H + 12h\mu_H\rho_H - 4\mu_H\rho_H]h^3Re/ \\
& [12\mu_H((h^3m - h^3\mu_H - 3h^2m + 3h^2\mu_H + 3hm - 3h\mu_H + \mu_H)\psi - h^3m + h^3\mu_H + \\
& 3h^2m - 3h^2\mu_H - 3hm + 3h\mu_H - \mu_H)]. \qquad \text{(E.1)}
\end{aligned}
$$

For pure fluids, $\phi_0 = 0$ and $\rho_H = \mu_H = 1$. Therefore, q is reduced to

$$
q \;=\; \frac{(3h^3m - 4h^3 - 6h^2m + 12h^2 + 3hm - 12h + 4)h^3Re}{12(h^3m - h^3 - 3h^2m + 3h^2 + 3hm - 3h + 1)}. \qquad \text{(E.2)}
$$

Appendix

F: Derivation of lubrication model Eqs. (3.18) and (3.19) for 2D channel

The flux function in the heavy fluid layer is expressed as

$$\hat{q} = \int_0^{\hat{h}} \hat{u} d\hat{y}, \tag{F.1}$$

Leibniz integral rule can be applied to obtain the derivative of $\hat{q}$

$$\hat{q}_{\hat{x}} = \frac{d}{d\hat{x}} \int_0^{\hat{h}} \hat{u} d\hat{y} = \int_0^{\hat{h}} \hat{u}_{\hat{x}} d\hat{y} + \hat{h}_{\hat{x}} \hat{u}|_{\hat{y}=\hat{h}}, \tag{F.2}$$

continuity requires $\hat{u}_{\hat{x}} = -\hat{v}_{\hat{y}}$, therefore

$$\hat{q}_{\hat{x}} = -\int_0^{\hat{h}} \hat{v}_{\hat{y}} d\hat{y} + \hat{h}_{\hat{x}} \hat{u}|_{\hat{y}=\hat{h}} = -\hat{v}(h) + \hat{h}_{\hat{x}} \hat{u}|_{\hat{y}=\hat{h}}. \tag{F.3}$$

Meanwhile, depthwise velocity of the height of heavy layer is given by

$$\hat{v}(h) = \frac{D\hat{h}}{D\hat{t}} = \hat{h}_{\hat{t}} + \hat{h}_{\hat{x}} u|_{\hat{y}=\hat{h}}, \tag{F.4}$$

thus, the evolution equation for the interface height is obtained as

$$\hat{h}_{\hat{t}} + \hat{q}_{\hat{x}} = 0. \tag{F.5}$$

Non-dimesnionlized form of (F.5) using $\hat{x} = \hat{L}x,\ \hat{h} = \hat{D}h,\ \hat{t} = \hat{L}t/\hat{V}_t,$ and $\hat{q} = \hat{D}\hat{V}_t q$, is

$$h_t + q_x = 0. \tag{F.6}$$

Similar approach can be applied to the particle flux

$$\frac{d}{d\hat{x}} \int_0^{\hat{h}} \hat{u}\phi d\hat{y} = \hat{u}|_{\hat{y}=\hat{h}} \phi|_{\hat{y}=\hat{h}} \hat{h}_{\hat{x}} + \int_0^{\hat{h}} \hat{u}_{\hat{x}} \phi d\hat{y} + \int_0^{\hat{h}} \hat{u}\phi_{\hat{x}} d\hat{y}, \tag{F.7}$$

from continuity $\hat{u}_{\hat{x}} = -\hat{v}_{\hat{y}}$, yields

$$\begin{aligned} \frac{d}{d\hat{x}} \int_0^{\hat{h}} \hat{u}\phi d\hat{y} &= \hat{u}|_{\hat{y}=\hat{h}} \phi|_{\hat{y}=\hat{h}} \hat{h}_{\hat{x}} - \int_0^{\hat{h}} \hat{v}_{\hat{y}} \phi d\hat{y} + \int_0^{\hat{h}} \hat{u}\phi_{\hat{x}} d\hat{y} \\ &= \hat{u}|_{\hat{y}=\hat{h}} \phi|_{\hat{y}=\hat{h}} \hat{h}_{\hat{x}} - \hat{v}|_{\hat{y}=\hat{h}} \phi|_{\hat{y}=\hat{h}} + \int_0^{\hat{h}} \hat{v}\phi_{\hat{y}} d\hat{y} + \int_0^{\hat{h}} \hat{u}\phi_{\hat{x}} d\hat{y}. \end{aligned} \tag{F.8}$$

As before,

$$\hat{v}|_{\hat{y}=\hat{h}} = \frac{D\hat{h}}{D\hat{t}} = \hat{h}_{\hat{t}} + \hat{h}_{\hat{x}} u|_{\hat{y}=\hat{h}}, \tag{F.9}$$

similarly,

$$\frac{d}{d\hat{x}} \int_0^{\hat{h}} \hat{u}\phi d\hat{y} = -\phi|_{\hat{y}=\hat{h}} \hat{h}_{\hat{t}} + \int_0^{\hat{h}} \hat{v}\phi_{\hat{y}} d\hat{y} + \int_0^{\hat{h}} \hat{u}\phi_{\hat{x}} d\hat{y}. \tag{F.10}$$

On the other hand from the Leibniz integral rule

$$\phi|_{\hat{y}=\hat{h}} \hat{h}_{\hat{t}} = \frac{d}{d\hat{t}} \int_0^{\hat{h}} \phi d\hat{y} - \int_0^{\hat{h}} \phi_{\hat{t}} d\hat{y}, \tag{F.11}$$

then,

$$\frac{d}{d\hat{x}}\int_0^{\hat{h}}\hat{u}\phi d\hat{y}=-\frac{d}{d\hat{t}}\int_0^{\hat{h}}\phi d\hat{y}+\int_0^{\hat{h}}\left(\phi_{\hat{t}}+\hat{u}\phi_{\hat{x}}+\hat{v}\phi_{\hat{y}}\right)d\hat{y}. \tag{F.12}$$

The particle transport equation for particle-laden film flows is given by [71] and [73] as

$$\phi_{\hat{t}}+\hat{u}\phi_{\hat{x}}+\hat{v}\phi_{\hat{y}}=-\hat{\mathbf{J}}_{\hat{x},\hat{x}}-\hat{\mathbf{J}}_{\hat{y},\hat{y}}. \tag{F.13}$$

Here, $\hat{\mathbf{J}}$ is the particle flux due to settling and migration. In absence of significant shear-induced migration effect and for the vertical channel geometry, only settling flux component remains in (F.13) which is defined

$$\widehat{\mathbf{J}}_{settling}=\frac{2\hat{a}^2\hat{g}\left(\hat{\rho}_p-\hat{\rho}_{f,H}\right)}{9\hat{\mu}_{f,H}}\left(1-\phi\right)\phi=\hat{u}_s\left(1-\phi\right)\phi. \tag{F.14}$$

Hence, (F.12) is modified

$$\frac{d}{d\hat{x}}\int_0^{\hat{h}}\hat{u}\phi d\hat{y}=-\frac{d}{d\hat{t}}\int_0^{\hat{h}}\phi d\hat{y}-\int_0^{\hat{h}}\hat{\mathbf{J}}_{\hat{x},\hat{x}}d\hat{y}, \tag{F.15}$$

and in the partial derivative form as

$$\int_0^{\hat{h}}\hat{\mathbf{J}}_{\hat{x},\hat{x}}d\hat{y}=\frac{\partial}{\partial\hat{x}}\int_0^{\hat{h}}\hat{\mathbf{J}}_{\hat{x}}d\hat{y}-\hat{\mathbf{J}}_{\hat{x}}|_{\hat{y}=\hat{h}}\hat{h}_{\hat{x}}. \tag{F.16}$$

The term $\hat{\mathbf{J}}_{\hat{x}}|_{\hat{y}=\hat{h}}\hat{h}_{\hat{x}}=0$, indicates the total flux leaving the interface of suspension layer as also appeared in [78]. Therefore,

$$\int_0^{\hat{h}}\hat{\mathbf{J}}_{\hat{x},\hat{x}}d\hat{y}=\frac{\partial}{\partial\hat{x}}\int_0^{\hat{h}}\hat{\mathbf{J}}_{\hat{x}}d\hat{y}, \tag{F.17}$$

integrating across width of the layer results in

$$\frac{\partial\left(\phi\hat{h}\right)}{\partial\hat{t}}+\frac{\partial\left(\hat{u}_{ave}\phi\hat{h}\right)}{\partial\hat{x}}+\frac{\partial\left(\hat{u}_{s}\left(1-\phi\right)\phi\hat{h}\right)}{\partial\hat{x}}=0, \tag{F.18}$$

since $u_p=\hat{u}_{ave}+\hat{u}_s\left(1-\phi\right)$, it is simplified as

$$\frac{\partial\left(\phi\hat{h}\right)}{\partial\hat{t}}+\frac{\partial\left(\hat{u}_{p}\phi\hat{h}\right)}{\partial\hat{x}}=0, \tag{F.19}$$

which in dimensionless form becomes

$$\frac{\partial\left(\phi h\right)}{\partial t}+\frac{\partial\left(u_{p}\phi h\right)}{\partial x}=0. \tag{F.20}$$

Appendix G: Derivation of lubrication model for axisymmetric flow in pipe (Appendix C)

The flux function in the heavy fluid layer is expressed as

$$\hat{q} = \int_{\hat{D}-\hat{h}}^{\hat{D}} 2\pi \hat{r}\hat{u}\, d\hat{r}, \tag{G.1}$$

Leibniz integral rule can be applied to obtain the derivative of $\hat{q}$

$$\hat{q}_{\hat{x}} = \frac{d}{d\hat{x}} \int_{\hat{D}-\hat{h}}^{\hat{D}} 2\pi \hat{r}\hat{u}\, d\hat{r} = \int_{\hat{D}-\hat{h}}^{\hat{D}} 2\pi \hat{r}\hat{u}_{\hat{x}}\, d\hat{r} + 2\pi \left(\hat{D}-\hat{h}\right)\hat{h}_{\hat{x}}\hat{u}|_{\hat{r}=\hat{D}-\hat{h}}, \tag{G.2}$$

continuity requires $\hat{u}_{\hat{x}} = -\partial(\hat{r}\hat{v})/\hat{r}\partial\hat{r}$, therefore

$$\begin{aligned}\hat{q}_{\hat{x}} &= -\int_{\hat{D}-\hat{h}}^{\hat{D}} 2\pi \hat{r}\frac{1}{\hat{r}}\frac{\partial(\hat{r}\hat{v})}{\partial\hat{r}}\, d\hat{r} + 2\pi \left(\hat{D}-\hat{h}\right)\hat{h}_{\hat{x}}\hat{u}|_{\hat{r}=\hat{D}-\hat{h}} \\ &= 2\pi \left(\hat{D}-\hat{h}\right)\hat{v}|_{\hat{r}=\hat{D}-\hat{h}} + 2\pi \left(\hat{D}-\hat{h}\right)\hat{h}_{\hat{x}}\hat{u}|_{\hat{r}=\hat{D}-\hat{h}}.\end{aligned} \tag{G.3}$$

Meanwhile, depthwise velocity of the height of heavy layer is given by

$$\hat{v}|_{\hat{r}=\hat{D}-\hat{h}} = \frac{D\left(\hat{D}-\hat{h}\right)}{D\hat{t}} = -\frac{D\hat{h}}{D\hat{t}} = -\hat{h}_{\hat{t}} - \hat{h}_x\hat{u}|_{\hat{r}=\hat{D}-\hat{h}}, \tag{G.4}$$

thus, the evolution equation for the interface height is obtained as

$$\hat{q}_{\hat{x}} = -2\pi \left(\hat{D}-\hat{h}\right)\hat{h}_{\hat{t}}. \tag{G.5}$$

Non-dimesnionlized form of (G.5) using $\hat{x} = \hat{L}x, \hat{h} = \hat{D}h,\ \hat{t} = \hat{L}t/\hat{V}_t,$ and $\hat{q} = \pi\hat{D}^2\hat{V}_t q$, is

$$\frac{\partial(1-h)^2}{\partial t} - \frac{\partial q}{\partial x} = 0. \tag{G.6}$$

Similar approach can be applied to the particle flux

$$\frac{d}{d\hat{x}} \int_{\hat{D}-\hat{h}}^{\hat{D}} 2\pi\hat{r}\hat{u}\phi d\hat{r} = 2\pi\left(\hat{D}-\hat{h}\right)\hat{u}|_{\hat{r}=\hat{D}-\hat{h}}\phi|_{\hat{r}=\hat{D}-\hat{h}}\hat{h}_{\hat{x}} + 2\pi\int_{\hat{D}-\hat{h}}^{\hat{D}} \hat{r}\hat{u}_{\hat{x}}\phi d\hat{r} + 2\pi\int_{\hat{D}-\hat{h}}^{\hat{D}} \hat{r}\hat{u}\phi_{\hat{x}} d\hat{r}, \tag{G.7}$$

from continuity $\hat{u}_{\hat{x}} = -\partial(\hat{r}\hat{v})/\hat{r}\partial\hat{r}$, yields

$$\begin{aligned}\frac{d}{d\hat{x}} \int_{\hat{D}-\hat{h}}^{\hat{D}} \hat{r}\hat{u}\phi d\hat{r} &= \left(\hat{D}-\hat{h}\right)\hat{u}|_{\hat{r}=\hat{D}-\hat{h}}\phi|_{\hat{r}=\hat{D}-\hat{h}}\hat{h}_{\hat{x}} - \int_{\hat{D}-\hat{h}}^{\hat{D}} \frac{\partial(\hat{r}\hat{v})}{\partial\hat{r}}\phi d\hat{r} + \int_{\hat{D}-\hat{h}}^{\hat{D}} \hat{r}\hat{u}\phi_{\hat{x}} d\hat{r} \\ &= \left(\hat{D}-\hat{h}\right)\hat{u}|_{\hat{r}=\hat{D}-\hat{h}}\phi|_{\hat{r}=\hat{D}-\hat{h}}\hat{h}_{\hat{x}} + \left(\hat{D}-\hat{h}\right)\hat{v}|_{\hat{r}=\hat{D}-\hat{h}}\phi|_{\hat{r}=\hat{D}-\hat{h}} \\ &+ \int_{\hat{D}-\hat{h}}^{\hat{D}} \hat{r}\hat{v}\phi_{\hat{r}} d\hat{r} + \int_{\hat{D}-\hat{h}}^{\hat{D}} \hat{r}\hat{u}\phi_{\hat{x}} d\hat{r}.\end{aligned} \tag{G.8}$$

As before,

$$\hat{v}|_{\hat{r}=\hat{D}-\hat{h}} = \frac{D\left(\hat{D}-\hat{h}\right)}{D\hat{t}} = -\frac{D\hat{h}}{D\hat{t}} = -\hat{h}_{\hat{t}} - \hat{h}_{\hat{x}}\hat{u}|_{\hat{r}=\hat{D}-\hat{h}}, \tag{G.9}$$

similarly,

$$\frac{d}{d\hat{x}} \int_{\hat{D}-\hat{h}}^{\hat{D}} \hat{r}\hat{u}\phi d\hat{r} = -\left(\hat{D}-\hat{h}\right)\phi|_{\hat{r}=\hat{D}-\hat{h}}\hat{h}_{\hat{t}} + \int_{\hat{D}-\hat{h}}^{\hat{D}} \hat{r}\hat{v}\phi_{\hat{r}} d\hat{r} + \int_{\hat{D}-\hat{h}}^{\hat{D}} \hat{r}\hat{u}\phi_{\hat{x}} d\hat{r}. \tag{G.10}$$

On the other hand from the Leibniz integral rule

$$\left(\hat{D}-\hat{h}\right)\phi|_{\hat{r}=\hat{D}-\hat{h}}\hat{h}_{\hat{t}}=\frac{d}{d\hat{t}}\int\limits_{\hat{D}-\hat{h}}^{\hat{D}}\hat{r}\phi d\hat{r}-\int\limits_{\hat{D}-\hat{h}}^{\hat{D}}\left(\hat{r}\phi\right)_{\hat{t}}d\hat{r}, \tag{G.11}$$

then,

$$\frac{d}{d\hat{x}}\int\limits_{\hat{D}-\hat{h}}^{\hat{D}}\hat{r}\hat{u}\phi d\hat{r}=-\frac{d}{d\hat{t}}\int\limits_{\hat{D}-\hat{h}}^{\hat{D}}\hat{r}\phi d\hat{r}+\int\limits_{\hat{D}-\hat{h}}^{\hat{D}}\hat{r}\left(\phi_{\hat{t}}+\hat{u}\phi_{\hat{x}}+\hat{v}\phi_{\hat{r}}\right)d\hat{r}. \tag{G.12}$$

The particle transport equation for particle-laden film flows is given by [71, 73]

$$\phi_{\hat{t}}+\hat{u}\phi_{\hat{x}}+\hat{v}\phi_{\hat{r}}=-\hat{\mathbf{J}}_{\hat{x},\hat{x}}-\hat{\mathbf{J}}_{\hat{r},\hat{r}}, \tag{G.13}$$

where,

$$\widehat{\mathbf{J}}_{settling}=\frac{2\hat{a}^2\hat{g}\left(\hat{\rho}_p-\hat{\rho}_{f,H}\right)}{9\hat{\mu}_{f,H}}\left(1-\phi\right)\phi=\hat{u}_s\left(1-\phi\right)\phi. \tag{G.14}$$

For the vertical channel geometry, hence, (G.12) is modified

$$\frac{d}{d\hat{x}}\int\limits_{\hat{D}-\hat{h}}^{\hat{D}}\hat{r}\hat{u}\phi d\hat{r}=-\frac{d}{d\hat{t}}\int\limits_{\hat{D}-\hat{h}}^{\hat{D}}\hat{r}\phi d\hat{r}-\int\limits_{\hat{D}-\hat{h}}^{\hat{D}}\hat{r}\hat{\mathbf{J}}_{\hat{x},\hat{x}}d\hat{r}, \tag{G.15}$$

and in the partial derivative form as

$$\int\limits_{\hat{D}-\hat{h}}^{\hat{D}}\hat{r}\hat{\mathbf{J}}_{\hat{x},\hat{x}}d\hat{r}=\frac{\partial}{\partial\hat{x}}\int\limits_{\hat{D}-\hat{h}}^{\hat{D}}\hat{r}\hat{\mathbf{J}}_{\hat{x}}d\hat{r}-\left(\hat{D}-\hat{h}\right)\hat{\mathbf{J}}_{\hat{x}}|_{\hat{r}=\hat{D}-\hat{h}}\hat{h}_x. \tag{G.16}$$

The term $\hat{\mathbf{J}}_{\hat{x}}|_{\hat{r}=\hat{D}-\hat{h}}\hat{h}_{\hat{x}}=0$, indicates the total flux leaving the interface of suspension layer as also appeared in [78]. Therefore,

$$\int_{\hat{D}-\hat{h}}^{\hat{D}} \hat{r}\hat{\mathbf{J}}_{\hat{x},\hat{x}}d\hat{r} = \frac{\partial}{\partial\hat{x}}\int_{\hat{D}-\hat{h}}^{\hat{D}} \hat{r}\hat{\mathbf{J}}_{\hat{x}}d\hat{r}, \tag{G.17}$$

integrating across width of the layer results in

$$\frac{\partial\left(\phi\left(\hat{D}^2-\left(\hat{D}-\hat{h}\right)^2\right)\right)}{\partial\hat{t}} + \frac{\partial\left[\phi\hat{q}+\hat{u}_s\left(1-\phi\right)\phi\left(\hat{D}^2-\left(\hat{D}-\hat{h}\right)^2\right)\right]}{\partial\hat{x}} = 0, \tag{G.18}$$

which in dimensionless form becomes

$$\frac{\partial\left(\phi\left(1-(1-h)^2\right)\right)}{\partial t} + \frac{\partial\left[\left(\phi q+u_s\left(1-\phi\right)\phi\left(1-(1-h)^2\right)\right)\right]}{\partial x} = 0. \tag{G.19}$$